Modeling and Control of Switching Converters: I. Unified Modeling and Measurement of Current-Programmed Converters II. A Generic Averaged Model for Switches in Dc-to-Dc Converters

Thesis by
Fang Dong Tan

In Partial Fulfillment of the Requirements
for the Degree of
Doctor of Philosophy

California Institute of Technology
Pasadena, California

1994
(Submitted November 10, 1993)

to my grandma, parents, and parents-in-law

Acknowledgements

I wish to thank my advisor, Professor R. D. Middlebrook, for accepting me directly into the Ph.D. program in power electronics at Caltech, for introducing me into the field of current programming, for his guidance, for his encouragement, and most of all, for the excellent example he has set as a lecturer, as a researcher, and as a writer.

I must also express my deep gratitude to Professor S. M. Ćuk, my co-advisor, for supervising me through the first half of my stay at Caltech, for his support, and for his guidance.

I gratefully acknowledge the financial support of the following corporations who supported my graduate research assistantships: Hughes Aircraft Co., Rockwell International Inc., General Electric Co., Apple Computer Inc., GEC Ferranti Defense Systems Ltd.,Southern California Edison Inc., Italtel Inc., Day-Ray Products Inc., and MagneTek Incorporated.

I thank each and every one of the members of the Power Electronics Group for the open exchange of ideas, the free flow of suggestions, and of course, the pleasure of friendships. Special thanks must go to Dr. A. Pietkiewicz, now with the ASCOM Power Systems, Switzerland, for sharing with me the original idea of using balance equations to characterize switches in PWM converters, and to J. L. Vollin for a fruitful three-year collaboration on the Hughes contract.

Thanks also go to all of our predecessors, who have left behind high standards for us to meet, and a large body of knowledge for us to build on.

Finally, my endeavor at Caltech could never have been possible without the support of my former professors at the Jiangxi Polytechnic University, Nanchang, China, and most especially without the love and support of my wife Fang and son Taige.

Abstract

Part I

A unified model is established for a current-programmed converter, which unifies and extends previous models.

A low-frequency modification leads to a unified duty-ratio control law for the buck, the boost, and the buck/boost converters, which results in improved predictions for several essential quantities of the current-loop gain.

Inclusion of the sampling effect allows the presence of an additional pole ω_p in the current-loop gain to be derived. The resulting final double-slope asymptote is fixed in position, and the crossover frequency cannot exceed half the switching frequency.

Two parameters are found to be central quantities of interest. A parameter D'_{min} represents the minimum value of D', the complementary duty ratio, to maintain stability of the current loop, and shows explicitly the stabilizing effect of a compensating ramp. A "stability parameter" Q_s determines the additional pole ω_p and describes the degree of peaking in the closed-loop transfer functions.

Experimental verification employs an analog signal injection technique, which is easier to use, and contains more information about high-frequency dynamics than a conventional digital signal injection technique.

Part II

A generic averaged model for switches in dc-to-dc converters is established for the first time by using, in addition to averaging, volt-second and amp-second balance equations.

The generic model inherits advantages of previous models and extend them to a new height: switches in dc-to-dc converters can now be handled as linear-time-invariant two-terminal circuit elements for their low-frequency characterizations.

It is shown that the generic model is equivalent to the canonical circuit model from state-space averaging when it is substituted into a particular converter. It is also shown that the model for PWM switches is a special case of the generic model.

A theoretical discussion about the equivalent duty ratio δ reveals that averaging can retain low-frequency information contained in the original quantity regardless of its ripple content. The conditions are that the dc value of the original quantity is not vanishingly small, and the perturbation frequency is limited to half the switching frequency for amplitude perturbation or to a quarter of the switching frequency for frequency perturbation.

Extensions of the generic model to converters with isolations, in discontinuous conduction mode, in current programming, and in other modes of operation are obtained. The concept of equivalent duty ratio is found useful.

One salient feature of the extended generic model, which distinguishes it from similar previous models, is that different versions of the model have exactly the same form. The invariance of the form of the model is extremely useful for computer simulations of the averaged large- and small-signal dynamics in dc-to-dc converters under various modes of operation.

One important feature of the approach, which separates it from all previous modeling approaches, is that its application is not limited by the number of switches in a converter. A three-switch converter is analyzed to show key steps in the derivation of a generic model for converters with multiple switches. Experimental results support the predictions from the generic model for the three-switch converter.

Contents

List of Figures

List of Tables

Part I

Unified Modeling and Measurement of Current-Programmed Converters

Chapter 1

Introduction

Current programming has become the regulating scheme of choice in dc-to-dc converters owing to its advantages over duty-ratio programming such as better line-noise rejection, automatic overload protection, easy paralleling of multiple converters, and especially design flexibility in improving small-signal dynamics.

Since its initial conception [1, 2], a large number of small-signal models have been proposed, for example, [3]-[13]. A brief non-exhaustive review of some of the previous efforts is presented in the following to show the evolution of models.

A low-frequency circuit-oriented approach was proposed in [5]. A modulator model (also referred to as "duty-ratio control law" by other authors) is derived by perturbation of an expression for the average inductor current in steady state. Then, the modulator model is interfaced with the state-space averaged model for the power stage to obtain a complete model for the entire converter. The interface is consistent since both the power stage and the modulator models are derived by perturbation of steady-state quantities. Current-loop gains are identified and then absorbed. This approach has gained wide acceptance owing to its simplicity and the insight gained into the properties of current programming.

One of the major insights gained in [5] is that the crossover frequency of the current loop can in general be considered wideband, implying possible degradation of performance of a low-frequency model. To cope with potential deficiencies, a separate earlier work [4] needed to be used. A sampled-data approach was presented in [4], where efforts were focused on high-frequency dynamics. This model is capable of predicting the well-known subharmonic oscillation which occurs, for example, when the duty ratio is greater than 0.5 and no compensating ramp is used. A general expression for the sampled-data version of the current-loop gain is derived, from which it is seen that the crossover

frequency of the current loop is limited to approximately one third of the switching frequency. It will be shown later analytically as well as experimentally that this estimate is too conservative. Another significant contribution of [4] is its detailed discussion on measurement of current-loop gain, some of which is further developed in the present work.

Another earlier work [13] suggested that the modulator gain factor F_m can approach infinity at the limit of stability. Since it is proportional to the modulator gain factor, the crossover frequency can approach infinity, too. A few authors have contested this result on the ground that Shannon's sampling theorem limits the crossover frequency to half the switching frequency. A resolution of this apparent contradiction is provided by the unified model developed in the present work. The unified model inherits the value of the gain factor and reveals that the the crossover frequency of the current-loop gain is limited to half the switching frequency, not by limiting the value of the modulator gain factor, but by the presence of an additional pole due to sampling.

The modulator model in [5] was derived by perturbation of an expression for inductor average current in steady state. This procedure was disputed in [7], where it is argued that the small-signal modulator model needs to be derived by perturbing an expression for inductor average current in perturbed state. A modulator model so-derived is then interfaced with the state-space averaged model for the power stage to yield the complete model. Experimental measurements, however, did not support its prediction for the case where no compensating ramp is used.

A continuous-time model was proposed in [8], where a modified Padé approximation of the complex exponential, accurate up to half the switching frequency, is used to approximate the sampled-data version of the current-loop gain derived in [4], allowing interpretation of sampled-data results in the continuous-time domain. Consequently, the mechanism behind the peaking, occurring at half the switching frequency in various closed-loop transfer functions when the duty-ratio is close to 0.5 and no compensating ramp is used, is seen to be due to the presence of a double right-half-plane zero at half the switching frequency. However, the expression for the current-loop gain crossover frequency is found to be the same as in [4], which lacks experimental support and is incon-

sistent with the corresponding closed-loop control-to-inductor-current transfer function.

A low-frequency model for switches in a current-programmed converter was proposed in [9], which enjoys easy implementation in computer simulation applications. A capacitance is used to emulate the sample-and-hold function. The current-loop gain is entirely suppressed. A Q-factor is found to determine the degree of peaking in closed-loop transfer functions.

In the following chapters, a unified model for current-programmed converters is developed. Discussions focus on the buck, the boost, and the buck/boost converters in continuous inductor current mode at constant frequency. However, general results, with suitable modifications, are equally applicable to other converters.

The unified model represents a low-frequency modification and a high-frequency extension over previous models. A low-frequency modification leads to a unified modulator model, which results in improved predictions for several essential quantities of current-loop gain. An extension to include sampling effect allows the presence of an additional pole in the current loop to be derived. Two parameters are found to be central quantities of interest. Parameter D'_{min}, the minimum value of D' to maintain stability of the current loop, shows explicitly the stabilizing effect of the compensating ramp. A "stability parameter" Q_s, related to the converter duty ratio and the compensating ramp, emerges as a central quantity of interest. Experimental verification employs an analog signal injection technique.

Chapter 2 derives a unified low-frequency modulator model, which improves low-frequency predictions. Subtle points in the derivation are identified. Chapter 3 analyzes the low-frequency current-loop gain and identifies its salient features. The crossover frequency of the current-loop gain can approach infinity at the stability limit. Different mechanisms exist for three basic converters to go unstable. Chapter 4 reveals two equivalent approaches to include the sampling effect in the current loop and exposes new features of current-loop gain. The high-frequency asymptote has a fixed slope -40dB/dec and crosses 0 dB at a fixed frequency (half the switching frequency). Chapter 5 discusses the measurement of current-loop gain and the related issues. It is concluded that analog signal injection outperforms digital signal injection in all aspects for cases where both of

them are applicable. Chapter 6 presents various closed-loop transfer functions. Abundant physical insights are obtained. Chapter 7 collects measured data on two prototype converters to support analytical results. Consistently good agreements between the measured and the predicted data are seen, validating the proposed unified model and the preferred measurement technique. Chapter 8 concludes the discussion of this part with a summary of major results.

Notation conventions adopted here are as follows. Capital letters are used to indicate quantities associated with steady-state, hatted letters are quantities associated with small-signal perturbations, and small letters represent quantities associated with perturbed state, i.e., quantities which are the sum of capital and hatted letters.

Chapter 2

A Unified Modulator Model

A brief introduction to the basics of current programming is first presented, where differences between current programming and duty-ratio programming are emphasized. Key steps of modeling a current-programmed converter are outlined. Then, a unified modulator model is derived. Subtle points in the derivation are pointed out. Some mathematical formalism used during its derivation is provided in the last section.

2.1 Basic Concept of Current Programming

Figure 2.1 (a) shows an illustrative diagram for a conventional duty-ratio-programmed buck converter. Because of the nature of the comparator (duty-ratio modulator), the duty ratio is determined when a ramp reaches a certain peak value set by a control voltage v_c. In common implementations, the ramp starts and ends with zero values and with a constant rising slope. Since the ramp is independent of any power stage variables, the duty ratio can be considered to be uniquely determined by the value of the control voltage v_c.

Figure 2.1 (b) is an illustrative diagram for a current-programmed buck converter, where inductor current is sensed and compared to a control current i_c. A clock signal initiates each switching cycle at a constant frequency. Duty ratio d is determined when inductor current i_l reaches a certain peak value set by i_c. Thus, the duty ratio depends not only on the value of control current (which sets the peak value), but also on how long it takes the inductor current to reach the peak value. Also, this time duration is determined by the starting value and the up-slope of inductor current.

Use of inductor current to determine duty ratio introduces feedback into the converter. Thus, small-signal dynamics is expected to change. A current-programmed

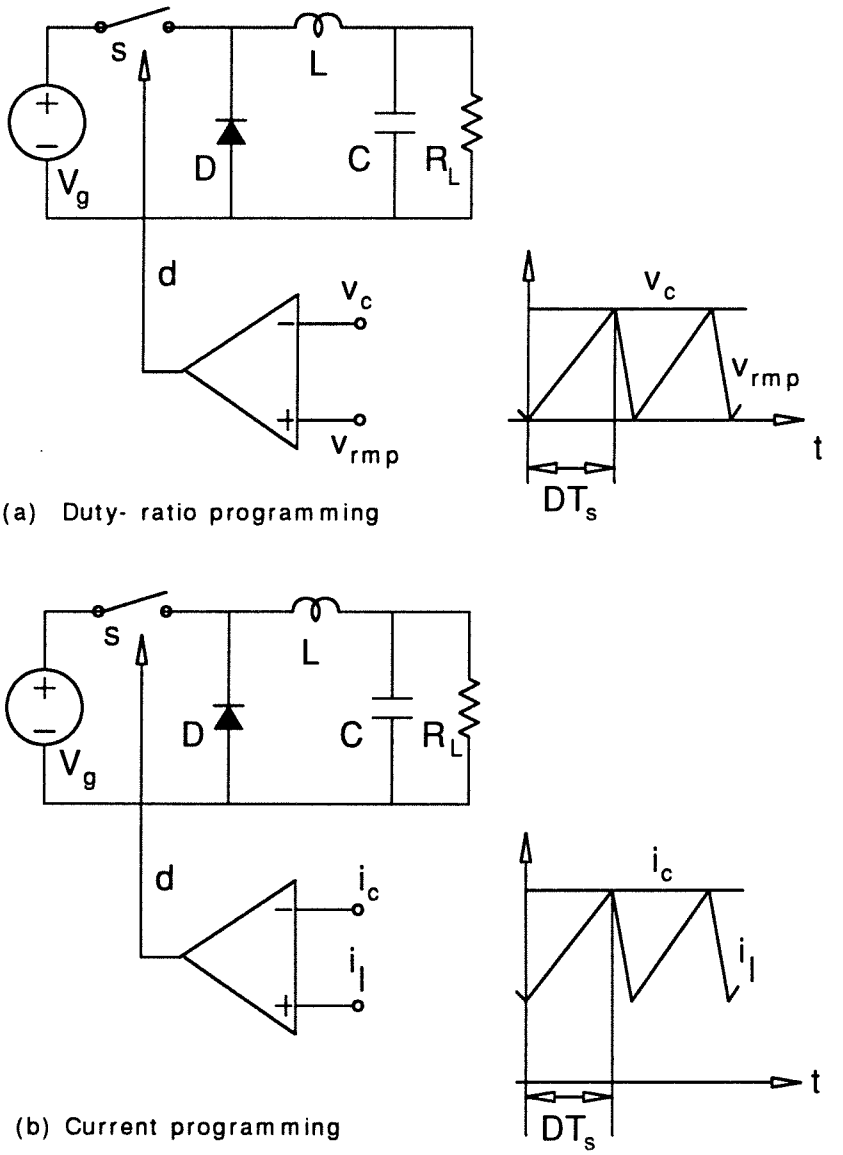

Figure 2.1: A duty-ratio-programmed buck converter (a), and a current-programmed buck converter (b) where the ramp function is obtained by sensing the inductor current. The ramp starts and ends with nonzero values, which is different from a duty-ratio programmed converter where the ramp starts and ends at zero values.

converter has much better dynamic performances than a duty-ratio programmed converter. Major advantages are: better line-noise rejection, automatic overload protection, easy paralleling of multiple converters, and most importantly, flexibility in improving small-signal dynamics.

The fact that duty ratio is directly related to the up-slope of inductor current is a major difference between current-programming and duty-ratio programming. This difference implies that duty ratio is not only related to control current and inductor current, but also to the effective voltage which determines the slopes of inductor current.

Another difference is the fact that inductor current ramp starts and ends with nonzero values if a converter is in continuous inductor current mode. These nonzero values are equal if a converter is in steady state, and they are not necessarily equal in perturbed state. As will be shown later, the nonzeroness of the starting and ending values makes the down-slope of inductor current play a role in the determination of duty ratio. This indirect dependence is a subtle point which has been overlooked by most previous authors writing on current programming.

To understand thoroughly current programming, a sound model is needed for current-programmed converters. A model for a current-programmed converter consists of two parts: 1) the model for the power stage, and 2) the model for the modulator, or interchangeably, the duty-ratio control law. Since the state-space averaged model [12] is frequently adopted as the model of choice for the power stage, the actual task is reduced to the establishment of a modulator model in a form consistent with the power stage model.

Since the duty ratio is related to the control current i_c, and the inductor current i_l, a modulator model is expected to be expressed in terms of the average inductor current i_l, the average control current i_c, and an effective voltage v_{off}, which determines the slopes of the inductor current (to be derived later). Therefore, a desired form of small-signal low-frequency model of a current-programmed converter can be drawn as shown in Fig. 2.2. This is essentially the same as in Figs. 11 - 13 of [5], except that a general canonical model for the power stage has been incorporated. Values of the parameters of the canonical model are well known and can be found in [12]. The modulator gain F_m and

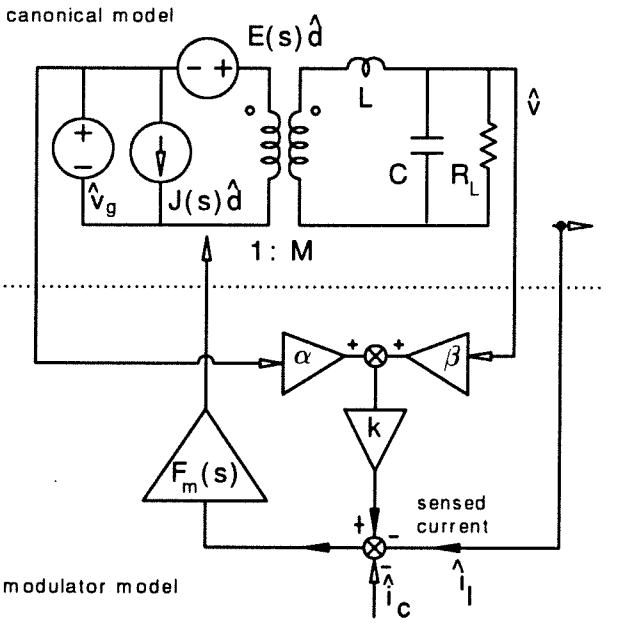

Figure 2.2: The small-signal low-frequency model of a current-programmed converter consists of two parts: a model for the power converter, and a model for the duty-ratio modulator. It is shown later that the frequency response of the modulator gain $F_m(s)$ is a simple pole at $\omega_p = (\omega_s/2)/Q_s$.

coefficients αk (replacing G_6) and βk (replacing H_3) reflect, respectively, the influence that the error current $\hat{i}_c - \hat{i}_l$, line voltage $\hat{v}_g$, and output voltage $\hat{v}$ may have on the duty ratio $\hat{d}$. The indicated frequency dependence for F_m is not due to the modulator; it will be shown later that its physical origin is the sampling effect.

What remains to be done is to determine values of various gain factors in Fig. 2.2. Before the derivation is pursued, some machineries are developed in the next section.

2.2 Definition of v_{off} and i_{on}, and Derivation of $\hat{v}_{off} = (\alpha\hat{v}_g + \beta\hat{v})$

Recent progress in understanding general behaviors of switching converters is the PWM tree structure, which is inherent to any switching converters. Analytical formulation of the structure provides a tool for unification of expressions for different converters.

Figure 2.3 shows the definition of v_{off} and i_{on} as originally proposed in [15]. Voltage

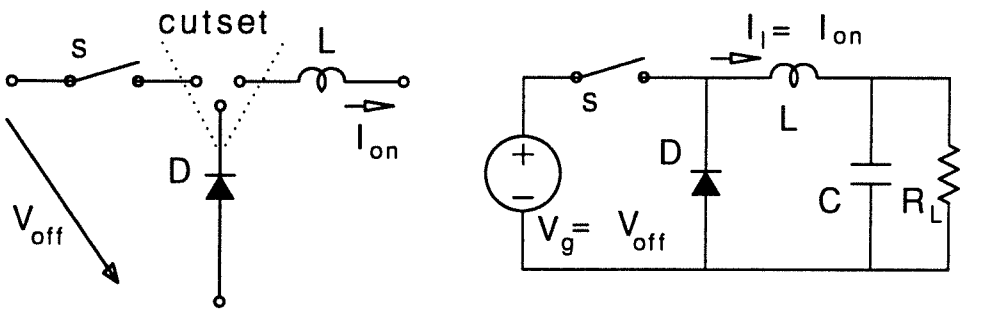

(a) The PWM structure (b) A buck example

Figure 2.3: Definition of v_{off} and i_{on} in the PWM tree structure. Voltage v_{off} is the sum of voltages across, and current i_{on} is the sum of currents through, the two switching devices.

v_{off} is the sum of the voltage across the transistor v_t and the voltage across the diode v_d, and current i_{on} is the sum of the current through transistor i_t and the current through the diode i_d, i.e.,

$$v_{off} = v_t + v_d, \tag{2.1}$$

$$i_{on} = i_t + i_d. \tag{2.2}$$

A physical interpretation of v_{off} is that, under small-ripple constraint, the value of v_{off} is the maximum voltage that either the transistor or the diode has to sustain when the other is in the off state. Similarly, the current i_{on} is the maximum current either the transistor or the diode has to sustain. The subcircuit in Fig. 2.3 is actually the underlying topological structure called the PWM tree in all PWM converters, which guarantees the desired PWM switching in a dc-to-dc converter [15, 16]. Voltage v_{off} is normally provided by a set of capacitances, and current i_{on} is supplied by a set of inductances [14, 16]. In other words, use of v_{off} and i_{on} has the potential of unifying expressions for variables in different PWM converters, which is evident in the derivation for the modulator model.

	$M(D)$	$E(s)$	J
Buck	D	$\frac{V_{off}}{D}$	I_{on}
Boost	$\frac{1}{D'}$	$V_{off}\left(1-\frac{sL}{D'V_{off}/I_{on}}\right)$	$\frac{I_{on}}{D'}$
Buck/Boost	$\frac{D}{D'}$	$V_{off}\left(1-\frac{sL}{D'V_{off}/I_{on}}\right)$	$\frac{I_{on}}{D'}$

Table 2.1: Simplified expressions for quantities in the canonical circuit model for three basic converters.

One of the useful results associated with v_{off} and i_{on} is the following identity established in [14, 15],

$$\frac{V_{off}}{I_{on}} = \frac{R}{M(D)}. \tag{2.3}$$

This identity reveals that the dc operating parameter R, defined as the ratio of output dc voltage over the dc output current, can also be interpreted as a transfer resistance which has the value of V_{off}/I_{on} scaled by $M(D)$. Table 2.1 presents modified expressions for the quantities in the canonical model. The unifying power of v_{off} and i_{on} is evident.

On the other hand, characterization of a converter is frequently pursued in terms of terminal quantities such as, for example, input voltage and output voltage. Under this circumstance, use of v_{off} is not always convenient since v_{off} is defined in terms of v_t and v_d, which are not necessarily terminal quantities. To remedy this, a relation is derived which connects $\hat{v}_{off}$ directly to input voltage $\hat{v}_g$, and output voltage $\hat{v}$.

For a dc-to-dc converter, it can be seen that input and output voltages v_g and v can be generally expressed as linear combinations of transistor voltage v_t and diode voltage v_d, i.e.,

$$\begin{cases} v_g = a_1 v_t + a_2 v_d \\ v = b_1 v_t + b_2 v_d, \end{cases} \tag{2.4}$$

where a_1, a_2, b_1, and $b_2 \in \{0, 1\}$.

Perturbation leads to the small-signal relationship

$$\begin{cases} \hat{v}_g = a_1\hat{v}_t + a_2\hat{v}_d \\ \hat{v} = b_1\hat{v}_t + b_2\hat{v}_d. \end{cases} \tag{2.5}$$

Solving leads to

$$\hat{v}_{off} = \hat{v}_t + \hat{v}_d = \frac{1}{(a_1b_2 - a_2b_1)}[(a_1 - b_1)\hat{v}_g + (b_2 - a_2)\hat{v}] \tag{2.6}$$

Since the two equations in Eq. (2.5) are linearly independent for any converters, one has $a_1/b_1 \neq a_2/b_2$, i.e., $a_1b_2 - a_2b_1 \neq 0$. This indicates that the above matrix inverse exists. Therefore, it can be concluded that perturbation of $\hat{v}_{off}$ is a linear combination of perturbations $\hat{v}_g$ and $\hat{v}$, or in equation form,

$$\hat{v}_{off} = a\hat{v}_g + b\hat{v}, \tag{2.7}$$

where $a, b \in \{0, 1\}$.

2.3 A Unified Modulator Model

Having developed the machineries in the previous section, the derivation for a unified modulator model can proceed.

Figure 2.4 shows inductor current waveforms in steady state (in solid lines) as well as in perturbed state (in dashed lines), where $-m_c$ is the slope of the compensating ramp, m_1 is the up-slope and $-m_2$ is the down-slope of the inductor current.

The geometries of the waveforms provide fundamental information for derivation of a modulator model. From the geometry of the inductor current waveform in steady state (in solid lines) and with slopes m_1, m_2, and m_c constant, one can write two equations:

$$\begin{cases} i_l = i_c - m_c dT_s - \frac{1}{2}m_1 dT_s \\ i_l = i_c - m_c dT_s - \frac{1}{2}m_2 d'T_s. \end{cases} \tag{2.8}$$

Note that these equations are written for steady state in order to be consistent with the canonical model for the power stage, which is derived by perturbation of a periodic steady-state solution to a linear time-varying system [12, 4].

Equation (2.8) is a set of simultaneous equations. They have to be met simultaneously. Many previous authors overlooked this point, which led to incomplete models.

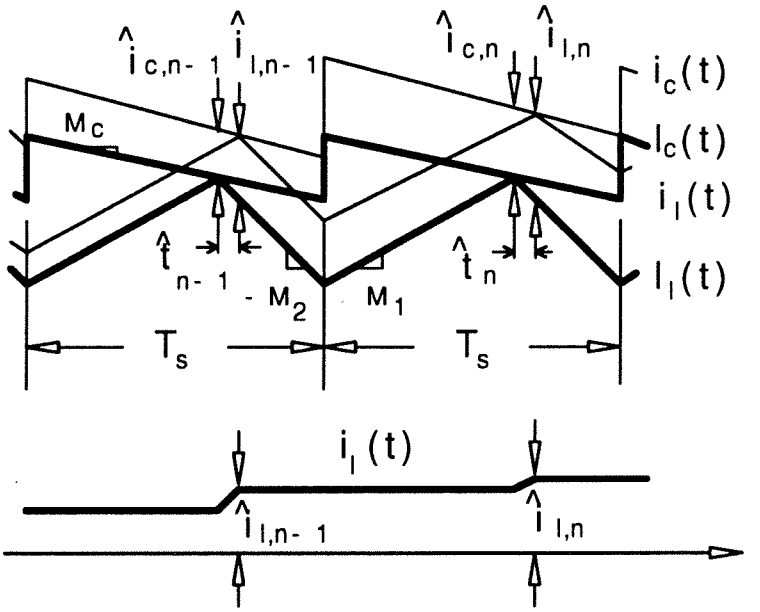

Figure 2.4: Geometries of inductor currents in steady (in thick lines) and perturbed (in thin lines) states. Essential information about the modulator model can be obtained from the geometries.

Another subtle point has to do with the way of meeting two equations simultaneously. Conventional approaches can not be simply applied. Elimination of variables is not useful, since all the variables need to be kept in order to obtain a complete characterization. Linear combination of two equations cannot be used either, since there are infinite possible combinations which yield the same average value of inductor current. Note that this uncertainty is actually a manifestation of the fact that the average value of inductor current is determined by the instantaneous value of inductor current at the time instant when i_l reaches the peak value set by i_c ($t = DT_s$), not the other way around. In fact, Eq. (2.8) can also be considered as the instantaneous value of the averaged current at the time instant DT_s.

The right way is to unify the two equations in Eq. (2.8) into a single expression, which can be accomplished by using the following general expressions, originated in [14],

for m_1 and m_2:

$$\begin{cases} m_1 = d' v_{off}/L \\ m_2 = d v_{off}/L, \end{cases} \tag{2.9}$$

where v_{off} is the sum of the two switch voltages [15] as discussed previously.

Substitution of Eq. (2.9) into either expression in Eq. (2.8) leads to the same expression:

$$i_l = i_c - m_c T_s d - \frac{dd'T_s}{2L} v_{off}. \tag{2.10}$$

That is to say, to satisfy Eq. (2.10) is equivalent to satisfying both equations in Eq. (2.8) simultaneously.

Equation (2.10) is a unified large-signal expression which describes how a duty ratio d is determined. Small-signal information can be derived by its perturbation, which yields

$$\hat{i}_l = \hat{i}_c - \left[M_c + \frac{(D' - D)V_{off}}{2L} \right] T_s \hat{d} - \frac{DD'T_s}{2L} \hat{v}_{off}. \tag{2.11}$$

Then, the unified modulator model is obtained as

$$\hat{d} = \frac{1}{[M_c + (D' - D)V_{off}/2L]T_s} \left[(\hat{i}_c - \hat{i}_l) - \frac{DD'T_s}{2L} (\alpha \hat{v}_g + \beta \hat{v}) \right], \tag{2.12}$$

where the expression $\hat{v}_{off} = \alpha \hat{v}_g + \beta \hat{v}$ has been used, with $\alpha = 1$, 0, and 1, and $\beta = 0$, 1, and 1, respectively, for the buck, the boost, and the buck-boost converters.

Hence, the following identifications can be made in Fig. 2.2:

$$F_m = \frac{1}{[M_c + (D' - D)V_{off}/2L]T_s}, \tag{2.13}$$

$$k = \frac{DD'T_s}{2L}. \tag{2.14}$$

The unified modulator model of Eq. (2.12) is a modification of that proposed in [5], and the modulator gain factor F_m is equivalent to that of [13]. In terms of F_m and k, Eq. 2.12 becomes

$$\hat{d} = F_m \left[(\hat{i}_c - \hat{i}_l) - k(\alpha \hat{v}_g + \beta \hat{v}) \right] \tag{2.15}$$

A useful parameter can be identified by rewriting Eq. (2.13) as

$$F_m = \frac{2L}{T_s V_{off}} \frac{1}{\left[\left(\frac{2LM_c}{D'V_{off}} + 2 \right) D' - 1 \right]}. \tag{2.16}$$

It reveals that F_m approaches infinity for $D' = 1/\left[\frac{2LM_c}{D'V_{off}} + 2\right]$, which is the minimum value for D' to maintain a finite positive value for F_m. Thus, it is useful to identify this particular value as

$$D'_{min} \equiv \frac{0.5}{\left(1 + \frac{M_c}{D'V_{off}/L}\right)}. \tag{2.17}$$

It is obvious that M_c, normalized with respect to a certain value, extends stability for $D'_{min} < 0.5$, or $D_{max} = 1 - D'_{min} > 0.5$, i.e., D'_{min} exhibits the stabilizing effect of M_c explicitly (more on this issue later).

In terms of D'_{min}, a low-entropy expression for F_m is obtained as

$$F_m = \frac{2L}{T_s V_{off}} \frac{1}{(D'/D'_{min} - 1)}. \tag{2.18}$$

Several physical interpretations are immediately available from low-entropy expressions for F_m and k in Eq. (2.15). The first factor in the right of Eq. (2.18) is a measure for the value of slopes since Eq. (2.9) shows that both M_1 and M_2 are proportional to the ratio V_{off}/L. The second factor represents the effect that the compensating ramp M_c has on the gain factor, to be elaborated in the next chapter. The value of k in Eq. (2.14) reflects the effect that perturbations of slopes M_1 and M_2 have on duty ratio. The larger the inductance L is, the smaller the effect is, since both slopes are in reciprocal proportion to inductance. The product DD' reveals that at both extremes of the duty ratio, the effect due to slope perturbations is vanishingly small.

Chapter 3

Current-Loop Gain

This chapter derives expressions for current-loop gain for three basic converters and discusses their salient features. An interpretation for D'_{min} is introduced, which represents the minimum value of D' to maintain stability of the current loop. Key steps of current-loop gain evaluation are shown on a buck converter by use of an analog signal injection technique. Essential quantities of interest are lumped together by drawing magnitude asymptotes of current-loop gains for three basic converters. Low-entropy expressions are also presented for the essential quantities. In addition, two general properties of current-loop gain are established, which provides added insight into the problem of modeling a current-programmed converter.

3.1 Interpretation of D'_{min}

In the light of Eq. (2.9), the definition for D'_{min} can be rewritten as

$$D'_{min} \equiv \frac{0.5}{(1 + M_c/M_1)}, \tag{3.1}$$

which exhibits explicitly the stabilizing effect that M_c, normalized with respect to M_1, has on the value of the complementary duty ratio D'. It is seen that $D'_{min} = 0.5$ if $M_c = 0$, and decreases with increasing M_c, corresponding to the well-known result that increasing compensating ramp extends stability upwards from $D = 0.5$.

Moreover, the unified modulator model indicates that a necessary condition for the current loop to be stable is that F_m remains positively finite, which in turn ensures that the current feedback remains negative and finite. The condition for F_m to be positively finite is simply

$$D' > D'_{min}, \tag{3.2}$$

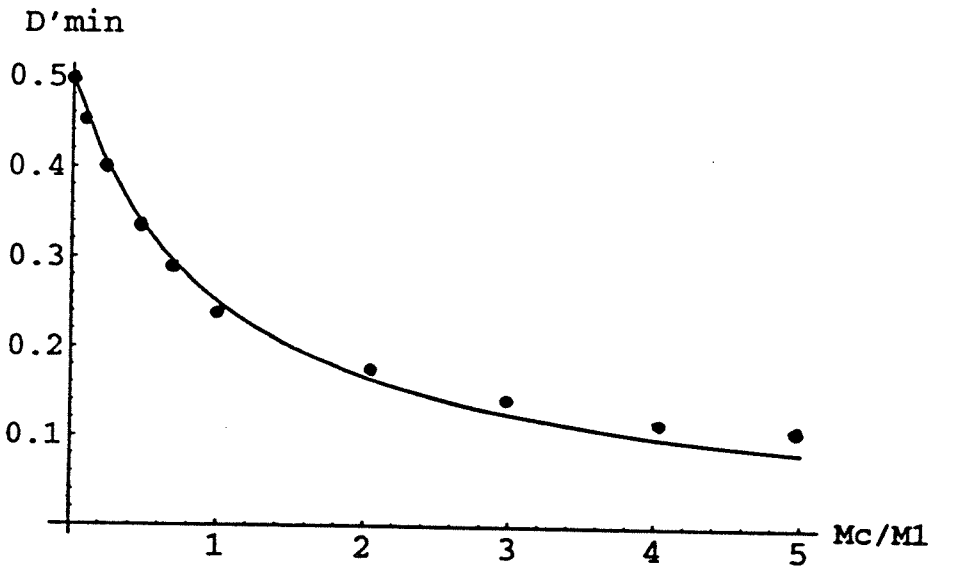

Figure 3.1: Measured data for D'_{min} show good agreement with predicted data, validating the identification of D'_{min}.

which is exactly the conventional condition for stability of the current loop detailed in [5].

Hence, the physical meaning associated with D'_{min} is that it represents the minimum value for the complementary duty ratio D' to have in order to maintain stability for the current loop. Indeed, investigation of the current loop, with sampling effect accounted for, shows that the current loop becomes unstable when D' approaches D'_{min}. D'_{min} can be reduced from 0.5, the value when M_c is zero, to a value approaching zero when M_c approaches infinity, a theoretical limit.

Figure 3.1 shows a plot of D'_{min} as a function of M_c/M_1 in solid line together with a set of measured data on a buck converter in dots. Measured data show good agreement with prediction, justifying the identification of D'_{min}.

3.2 Evaluation of Current-Loop Gain

Current-loop gains can be evaluated by application of an analog current injection technique used as an analysis tool in the unified model. Steps in [5] can be followed.

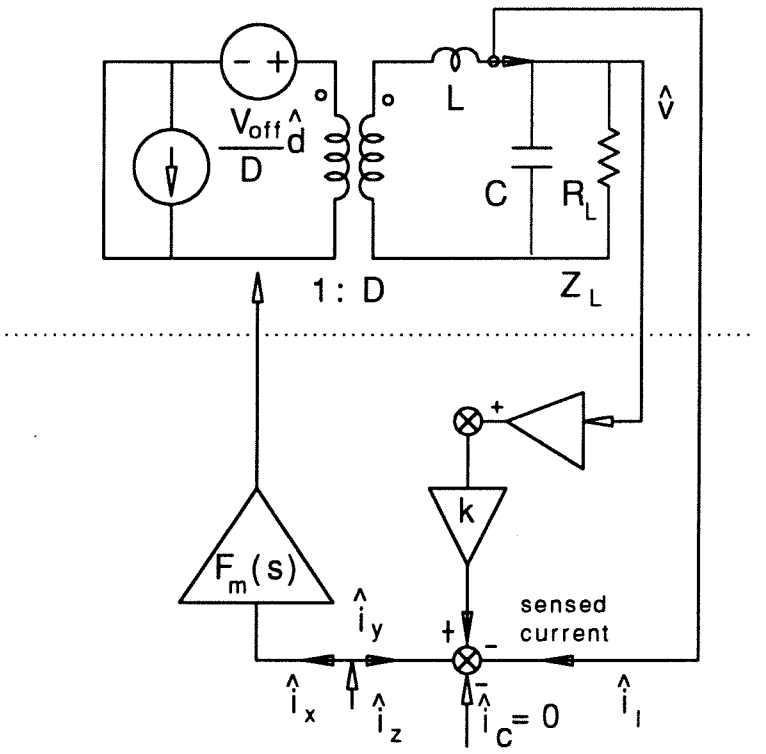

Figure 3.2: Evaluation of a current-loop gain for a buck converter by an analog current injection under the condition $\hat{v}_g = 0$ and $\hat{i}_c = 0$. A nested loop exists due to the presence of $\hat{v}_{off}$ $(= \hat{v})$, which gives the current-loop gain an additional factor.

To illustrate key steps, a buck converter is analyzed. Figure 3.2 shows the equivalent circuit for evaluating a current-loop gain for a buck converter. A test current $\hat{i}_z$ is injected and a current-loop gain is obtained by evaluating the ratio $T_c = \hat{i}_y/\hat{i}_x$ under the condition that $\hat{i}_c = 0$ and $\hat{v}_g = 0$.

A nested voltage loop, which does not exist physically in the converter, is introduced into the unified model because of the presence of $\hat{v}_{off}$, which gives T_c an extra factor. Voltage V_{off} in a buck is related to input as well as output voltages by $V_{off} = V_g = V/D$, where D is the voltage conversion ratio of a buck converter. The corresponding nested

voltage loop gain can be obtained by inspection of Figure 3.2 as

$$\begin{aligned} T_v(s) &= \beta k F_m \frac{V_{off}}{D} D \frac{z_L}{sL_e + z_L} \\ &= \frac{\beta k F_m V_{off}}{1 + \frac{1}{Q_0}\left(\frac{s}{\omega_0}\right) + \left(\frac{s}{\omega_0}\right)^2} \end{aligned} \tag{3.3}$$

where

$$\omega_0 = \frac{1}{\sqrt{LC}} \tag{3.4}$$

$$Q_0 = \frac{R_L}{R_0} \tag{3.5}$$

$$R_0 = \sqrt{\frac{L}{C}} \tag{3.6}$$

The feedback factor for the nested voltage loop is given by

$$\begin{aligned} 1 + T_v(s) &= 1 + \frac{\beta k F_m V_{off}}{1 + \frac{1}{Q_0}\left(\frac{s}{\omega_0}\right) + \left(\frac{s}{\omega_0}\right)^2} \\ &= \frac{[1 + T_v(0)]\left[1 + \frac{1}{Q_0\sqrt{1 + T_v(0)}}\left(\frac{s}{\omega_0\sqrt{1 + T_v(0)}}\right) + \left(\frac{s}{\omega_0\sqrt{1 + T_v(0)}}\right)^2\right]}{1 + \frac{1}{Q_0}\left(\frac{s}{\omega_0}\right) + \left(\frac{s}{\omega_0}\right)^2}, \end{aligned} \tag{3.7}$$

where

$$T_v(0) \equiv \beta k F_m V_{off}. \tag{3.8}$$

Current-loop gain is then obtained as

$$\begin{aligned} T_c(s) &= \frac{1}{1 + T_v(s)} F_m \frac{V_{off}}{D} D \frac{1}{sL + z_L} \\ &= \frac{F_m V_{off}/R_L}{1 + \beta k F_m V_{off}} \frac{\left(1 + \frac{s}{\omega_l}\right)}{1 + \frac{1}{Q_0\sqrt{1 + T_v(0)}}\left(\frac{s}{\omega_0\sqrt{1 + T_v(0)}}\right) + \left(\frac{s}{\omega_0\sqrt{1 + T_v(0)}}\right)^2}, \end{aligned} \tag{3.9}$$

where

$$\omega_l = \frac{1}{R_L C} \tag{3.10}$$

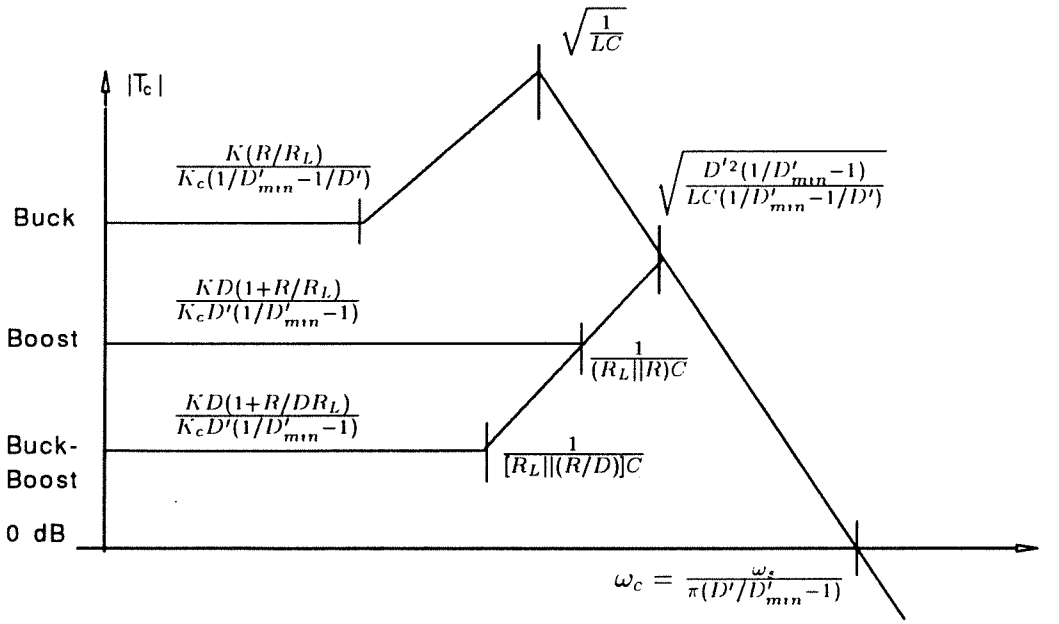

Figure 3.3: Current-loop gains for three basic converters. The extrapolated crossover frequency ω_c approaches infinity if $D' \rightarrow D'_{min}$, the stability limit. Expressions for $T_c(0)$ reveal that the mechanism for instability for the buck is different from those for the boost and the buck/boost converters.

Similar procedures are applied to boost and buck/boost converters. Results are graphically summarized in Figure 3.3. Expressions for all converters are for the case where $R_e = 0$ for clarity and simplicity, and D'_{min} has been used.

Characteristics of current-loop gain can be extracted from the low-entropy expressions and are discussed as follows.

The results, shown in Fig 3.3, are qualitatively the same as those in [5]. The most salient feature is that the final asymptote is the same for all three converters, crossing zero dB at ω_c. This property reflects the fact that at high-frequencies, converter dynamics is determined by switches and inductances only. The expression for ω_c is of the form

$$\omega_c = \frac{\omega_s}{\pi(D'/D'_{min} - 1)}, \tag{3.11}$$

which is in terms of the operating point parameter D' relative to its minimum value D'_{min} for stability, and ω_c approaches infinity when D' approaches D'_{min}, i.e., in the stability limit. Note also that the value of ω_c is directly proportional to the value of the modulator

gain.

Extension of $T_c(s)$ to include the sampling effect shows that ω_c is not necessarily the current loop crossover frequency because of the presence of an additional pole in $T_c(s)$. For this reason, ω_c will from now on be called the extrapolated crossover frequency of current-loop gain.

The dc value of the current-loop gain $T_c(0)$ is expressed in terms of $K/K_c \equiv K/K_{crit}$ which, as described in [5], represents the ratio of the inductance L to its minimum value L_c to maintain continuous conduction. The minimum inductance can be derived by equating K to K_c, and then solving for L_c. For all three converters, the minimum value of inductance is given by a unified expression

$$L_c = \frac{DD'T_s}{2}\frac{V_{off}}{I_{on}}. \tag{3.12}$$

Having introduced L_c, respective values for $T_c(0)$ can be written as

$$T_c(0) = M(D)\left(\frac{L}{L_c}\right)\frac{(V_{off}/I_{on})/R_L}{(1/D'_{min} - 1/D')}, \qquad \text{buck} \tag{3.13}$$

$$T_c(0) = DM(D)\left(\frac{L}{L_c}\right)\frac{[1 + (V_{off}/I_{on})/D'R_L]}{(1/D'_{min} - 1)}, \qquad \text{boost} \tag{3.14}$$

$$T_c(0) = M(D)\left(\frac{L}{L_c}\right)\frac{[1 + (V_{off}/I_{on})/D'R_L]}{(1/D'_{min} - 1)}. \qquad \text{buck/boost} \tag{3.15}$$

It is interesting to note that expressions for $T_c(0)$ can be shown to be identical to those presented in [5], where a different value for the modulator gain F_m was used. This surprising result seems to suggest that the dc value of a current-loop gain is independent of the value of the modulator gain. Indeed, it can be shown that this is generally true. A discussion of it is presented in the following section.

Expressions for current-loop gains reveal that there are two different mechanisms for a current loop to become unstable. For a buck converter, the double pole is fixed in position. The extrapolated crossover frequency ω_c approaches infinity when $T_c(0)$ becomes unlimited. Note that in reality, $T_c(0)$ will be limited by parasitic resistance that inevitably exists in a converter. For a boost or a buck/boost, the double pole changes in position with different values of the compensating ramp and the duty ratio. $T_c(0)$ is

always finite. In these two cases, ω_c goes to infinity together with the double pole in the stability limit.

The values ω_c and $T_c(0)$ can be effectively controlled by introducing different values for the compensating ramp, if duty ratio and inductance are kept the same. The larger the ramp slope is, the lower the values of ω_c and dc gain are. A rule of thumb is that for $M_c = M_2$, $\omega_c \approx \omega_s/3$. In an actual design, it is suggested that a value of M_c larger than M_2 be selected to accommodate possible degradation caused by possible parasitic reactances associated with current sensing circuitry.

3.3 Other Properties of Current-Loop Gain

In this section, additional properties of current-loop gain are derived, which provide deep insight into the way how different values of the modulator gain factor influence two essential quantities of current-loop gain, $T_c(0)$ and ω_c. $T_c(0)$ is important since it decides the degree of regulation that a converter has against low-frequency disturbances. The extrapolated crossover frequency ω_c is important because it determines pole locations of transfer functions when the current loop is closed. Together, these two properties give added insight into the problem of modeling a current-programmed converter.

A note about notation is due here. Parameter $n \equiv (1 + 2M_c/M_1)$ used in [5] is kept only in this section for easy reference to and comparisons with previous results.

It can be shown that the following two statements are true:

- the dc value of current-loop gain $T_c(0)$ is independent of the value of the modulator gain factor F_m,
- the extrapolated crossover frequency of the current-loop gain ω_c is directly proportional to the value of the modulator gain factor F_m.

The first property can be established by working with three basic converters, respectively. If the modulator gain factor is not specified, the modulator model for a current-programmed converter can be written as (recall Eq. (2.15)),

$$\hat{d} = F_m \left[(\hat{i}_c - \hat{i}_L) - \alpha' k \hat{v}_g - \beta' k \hat{v} \right], \tag{3.16}$$

where $\alpha', \beta' \in \{-1, 1\}$. Note that feedback coefficients α' and β' are allowed to have negative values here to accommodate potential positive feedback in the minor loop.

The task is to obtain expressions for $\alpha' k$ as well as $\beta' k$. The approach proposed in [8] is used, which derives values of the feedback coefficients by perturbation of expression for average value of inductor current. Then, this expression is equated to another expression obtained from an equivalent circuit model, which can then be solved for the desired coefficient. This approach is applied here with the help of Figure 2.2 and Eq. (2.10) (Note that Eq. (2.10) is different from that used in [8]).

Results are collected as follows.

$$\alpha' k = D\left[\frac{1}{F_m V_{off}} - \frac{(nD' - 1)}{KR}\right], \qquad \text{buck,buck/boost} \qquad (3.17)$$

$$\alpha' k = \left[\frac{1}{F_m V_{off}} - \frac{(nD' - D)}{KR}\right], \qquad \text{boost} \qquad (3.18)$$

$$\beta' k = \left[\frac{(nD' - D)}{KR} - \frac{1}{F_m V_{off}}\right], \qquad \text{buck} \qquad (3.19)$$

$$\beta' k = D'\left[\frac{nD'}{KR} - \frac{1}{F_m V_{off}}\right]. \qquad \text{boost,buck/boost} \qquad (3.20)$$

It needs to be emphasized that the above expressions for $\alpha' k$ and $\beta' k$ are general formulas. They can be used to reproduce the same coefficients as in Eq. (2.12) as well as those in [5, 7, 8] if respective values for F_m are substituted in.

Having derived expressions for feedback coefficients, one can proceed to evaluate dc values of current-loop gain for three basic converters in the same way as shown in the previous section.

For the buck converter,

$$\begin{aligned} T_c(0) &= \frac{F_m V_{off}/R_L}{1 + |\beta'| k F_m V_{off}} \qquad (3.21) \\ &= \frac{F_m V_{off}/R_L}{1 + [(nD' - D)/KR] F_m V_{off} - 1} \\ &= \frac{KR/R_L}{(nD' - D)}. \end{aligned}$$

For the boost converter,

$$\begin{aligned} T_c(0) &= \frac{F_m V_{off}(1+R/R_L)/D'^2R}{1+|\beta'|kF_mV_{off}/D'} \\ &= \frac{F_m V_{off}(1+R/R_L)/D'^2R}{1+(nD'/KR)F_mV_{off}-1} \\ &= \frac{K(1+R/R_L)}{nD'^3}. \end{aligned} \tag{3.22}$$

For the buck/boost converter,

$$\begin{aligned} T_c(0) &= \frac{F_m V_{off}D(1+R/DR_L)/D'^2R}{1+|\beta'|kF_mV_{off}/D'} \\ &= \frac{F_m V_{off}D(1+R/DR_L)/D'^2R}{1+(nD'/KR)F_mV_{off}-1} \\ &= \frac{DK(1+R/DR_L)}{nD'^3}. \end{aligned} \tag{3.23}$$

F_m is cancelled out in all three expressions. Hence, it can be concluded that the dc value for the current-loop gain is independent of the value of F_m.

In short, $T_c(0)$ is given by

$$T_c(0) = \frac{KR/R_L}{nD'-D}, \qquad \text{buck} \tag{3.24}$$

$$T_c(0) = \frac{K(1+R/R_L)}{nD'^3}, \qquad \text{boost} \tag{3.25}$$

$$T_c(0) = \frac{DK(1+R/DR_L)}{nD'^3}, \qquad \text{buck/boost} \tag{3.26}$$

which are identical to those values for $T_c(0)$ presented in [5], and those in the previous section if D'_{min} is used instead of n.

The second statement is established in a straightforward manner. Figure. 3.4 shows a high-frequency equivalent circuit which a current-programmed converter can be reduced to. This is obtained by using the fact that at high-frequencies, all capacitances can be replaced by short circuits.

From the equivalent circuit, it is straightforward to see that high-frequency asymptote of current-loop gain is given by

$$T'_c = F_m \frac{V_{off}}{D} D \frac{1}{sL} = \frac{\omega_c}{s}, \tag{3.27}$$

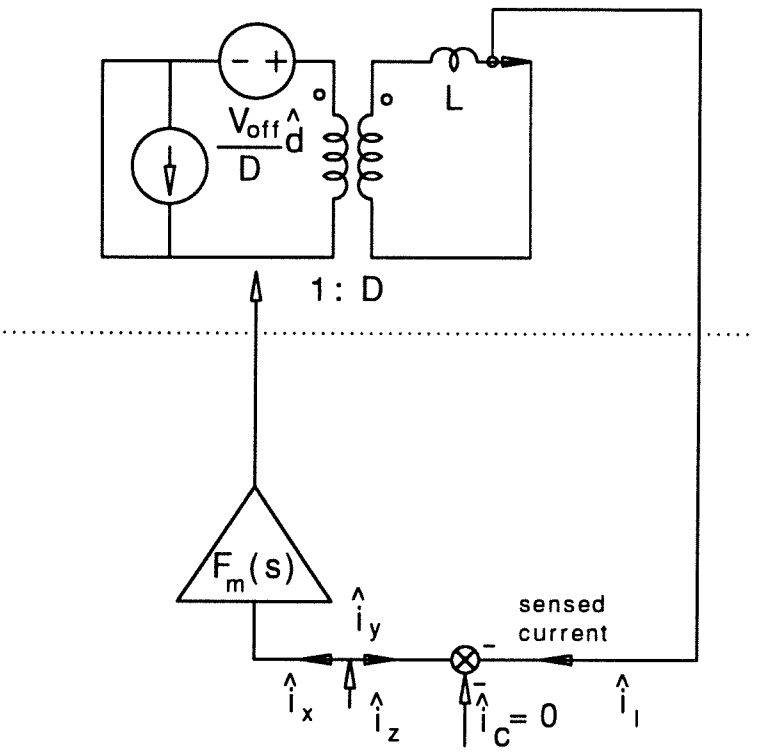

Figure 3.4: An equivalent circuit for a current-programmed converter at high frequencies. The load resistance is shorted out of the circuit by the low impedance presented by the output capacitance which is constrained to be large for small ripples.

where

$$\omega_c = F_m \frac{V_{off}}{L}. \tag{3.28}$$

Since V_{off} and L are real-valued constants, it can be concluded that the extrapolated crossover frequency ω_c is directly proportional to the modulator gain factor F_m.

Finally, a useful comparison can readily be made among different models for current programming with regard to predictions for values of ω_c. The duty-ratio modulator gain factor F_m has the value $\frac{KR}{V_{off}(nD'-D)}$, $\frac{KR}{V_{off}(nD')}$, $\frac{KR}{V_{off}(n-1)D'}$, and $\frac{KR}{(n+1)D'}$ for the unified model, the Middlebrook model [5], the Verghese model [7], and the Ridley model [8],

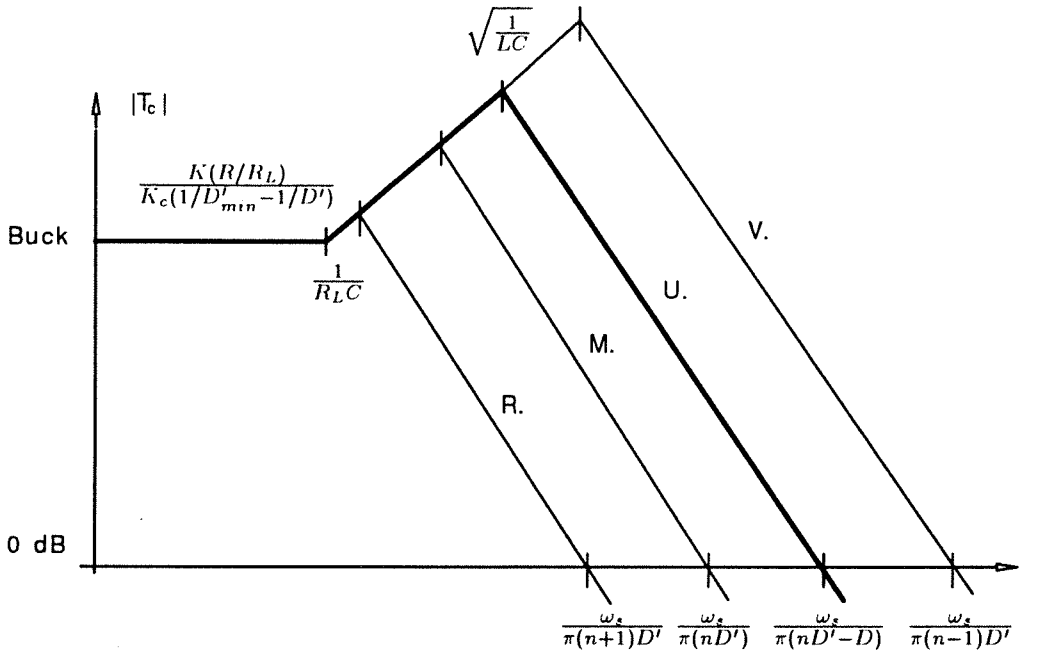

Figure 3.5: Comparison of predictions of different models for magnitude asymptotes of the current-loop gain. All previous models approach the unified model only in the limit when $D'_{min} \rightarrow 0$, i.e., when $M_c \rightarrow \infty$. Note that the Verghese model (V.) approaches the unified model (U.) from the above, and the Middlebrook (M.) and the Ridley (R.) models approach the unified model from the below.

respectively. Then, according to Eq. (3.28), the extrapolated crossover frequency ω_c has the value $\frac{\omega_s}{\pi(nD'-D)}$, $\frac{\omega_s}{\pi(nD')}$, $\frac{\omega_s}{\pi(n-1)D'}$, and $\frac{\omega_s}{\pi(n+1)D'}$, respectively. The resulting current-loop gain predictions are shown in Figure 3.5 for the case of the buck converter. Similar scenarios exist for the cases of the boost and the buck/boost converters.

It can be seen that models in [5, 8] give underestimates for the value of ω_c, while model in [7] presents an overestimate. Models in [5, 7, 8] all predict a variable double pole for a buck, while the unified model predicts a fixed value, which is supported by measured data to be presented later. Also, models in [5, 7, 8] approach the prediction by the unified model only when M_c goes to infinity. The difference among them is that the Verghese model [7] approaches it from above, while the Middlebrook and the Ridley models [5, 8] approach it from below.

Chapter 4

Sampling Effect

As indicated in the previous chapter, the current-loop gain can be considered wide-band. Consequently, predictions from a low-frequency model may not be sufficient. Therefore, the high-frequency behavior of the current-loop gain needs to be thoroughly understood if the reliability of design is to be guaranteed.

High-frequency dynamics is predominantly due to the sampling mechanism inherently present in a switching converter. The term inherent sampling mechanism is used here to refer to the fact that duty ratio is determined only once in a switching cycle and ideally instantaneously. Influences due to parasitic inductances and capacitances can normally be well controlled to be small. Even if these influences are not negligible, conventional circuit theory can be used to handle them.

Hence, the influence of the sampling mechanism on current-loop gain, hereafter referred to as the sampling effect, is the focus of discussion.

The basic philosophy adopted here is to find a high-frequency correction factor to augment current-loop gain derived from a low-frequency model. Accuracy of modeling beyond half the switching frequency will be sacrificed willingly to trade for simplicity of the correction factor. As will be shown later, a surprisingly simple expression can be derived, thanks to the property that the crossover frequency of current-loop gain is limited to half the switching frequency.

Two approaches are developed in the first two sections to derive the same result, which can be stated as follows:. To predict high-frequency dynamics of current-loop gain with good accuracy up to half the switching frequency, only one additional pole ω_p needs to be added to a current-loop gain derived from the low-frequency model to represent the sampling effect.

The last section presents complications of characteristics for current-loop gain intro-

duced by the existence of the additional pole.

4.1 Additional Pole ω_p: First Approach

The first approach is to find a rational function approximation of the sampled representation of the closed-loop transfer function $\hat{i}_l/\hat{i}_c$ of the current-programmed power stage, from which the presence of one additional pole in $T_c(s)$ is inferred.

From the geometry of the currents in Fig. 2.4, one can write two discrete-time equations:

$$\begin{cases} \Delta i_{c,n+1} = \Delta i_{l,n} + M_1 \Delta t_{n+1} + M_c \Delta t_{n+1} \\ \Delta i_{l,n+1} = \Delta i_{c,n+1} - M_c \Delta t_{n+1} + M_2 \Delta t_{n+1}. \end{cases} \tag{4.1}$$

Two results can be obtained from this set of equations: one is the duty-ratio modulator gain F_m, and the other is a discrete-time transfer function $\Delta i_l/\Delta i_c$.

Information about the duty ratio can be obtained by solving for Δt_{n+1} in Eq. (4.1). Subtraction of the first expression from the second and then rearranging yields

$$\hat{d}_{n+1} \equiv \frac{\Delta t_{n+1}}{T_s} = \frac{\Delta i_{c,n+1} - (\Delta i_{l,n+1} + \Delta i_{l,n})/2}{[M_c + (M_1 - M_2)/2]T_s}. \tag{4.2}$$

With the restriction of low-frequency perturbation, one has $\Delta i_{l,n+1} \approx \Delta i_{l,n}$, which in turn gives

$$\hat{d} = \frac{\hat{i}_c - \hat{i}_l}{[M_c + (M_1 - M_2)/2]T_s} = \frac{2L}{T_s V_{off}} \frac{1}{(D'/D'_{min})}, \tag{4.3}$$

which shows the same coefficient as in Eq. (2.12) and verifies the result for the modulator gain F_m derived above.

The discrete transfer function from control Δi_c to inductor current Δi_l is derived by introduction of the z-transform into the two equations in Eq. (4.1), which leads to

$$\frac{\Delta i_l(z)}{\Delta i_c(z)} = a \frac{z}{z - 1 + a}, \tag{4.4}$$

where $a \equiv (M_1 + M_2)/(M_1 + M_c) = 2D'_{min}/D'$.

To derive a continuous expression for the current transfer function, two more relationships are needed: 1) the connection between the z domain and the sampled-Laplace

domain; and 2) the connection between the sampled- and the continuous-Laplace domains.

The first is the identity $z=e^{sT_s}$. The second is provided by the concept of "equivalent hold" proposed in [18], which states: In the small-signal limit, the continuous quantity $\hat{i}_l$ is related to its sampled counterpart by the transfer function of a zeroth-order-hold circuit.

Applying this property, one obtains

$$\hat{i}_l(s) = a\frac{e^{sT_s}}{e^{sT_s}-1+a}\frac{1-e^{-sT_s}}{s}\hat{i}_c^*(s), \tag{4.5}$$

where the asterisk represents a sampled quantity and

$$\hat{i}_c^*(s) = \frac{1}{T_s}\sum_{n=-\infty}^{\infty}\hat{i}_c\left(s+\frac{j2n\pi}{T_s}\right) \approx \frac{1}{T_s}\hat{i}_c(s). \tag{4.6}$$

The approximation is made possible by the fact that the control current can be taken to be a pure sinusoid, and hence contributions of sidebands are negligible if a narrow-band analyzer is used for measurement.

To simplify further the current transfer function, one can invoke the following modified Padé approximation for the complex exponential, originated implicitly in [8]:

$$e^{-sT_s} = \frac{1-\frac{1}{2/\pi}\left(\frac{s}{\omega_s/2}\right)+\left(\frac{s}{\omega_s/2}\right)^2}{1+\frac{1}{2/\pi}\left(\frac{s}{\omega_s/2}\right)+\left(\frac{s}{\omega_s/2}\right)^2}. \tag{4.7}$$

This above approximation enjoys good accuracy up to half the switching frequency. Substitution of Eq. (4.7) into Eq. (4.5) yields

$$\frac{\hat{i}_l(s)}{\hat{i}_c(s)} = \frac{1}{1+\frac{1}{Q_s}\left(\frac{s}{\omega_s/2}\right)+\left(\frac{s}{\omega_s/2}\right)^2}, \tag{4.8}$$

where $Q_s = \frac{2}{\pi(2/a-1)}$, or

$$Q_s \equiv \frac{2}{\pi(D'/D'_{min}-1)}. \tag{4.9}$$

It is seen that the current transfer function is a standard low-pass quadratic with its corner located at half the switching frequency, and whose Q-factor Q_s can be effectively controlled by the compensating ramp M_c through the parameter D'_{min}.

Moreover, the expression for Q_s reveals explicitly that oscillation is possible if Q_s goes to infinity, that is, if the inequality $D' > D'_{min}$ is violated, which is exactly the conventional criterion for stability of the current loop [3, 5]. Since this potential oscillation will be at half the switching frequency, it is commonly referred to as subharmonic oscillation.

The denominator of Eq. (4.8) is typical of the closed-loop response of a system having a two-pole loop gain in the neighborhood of the crossover frequency. If in this neighborhood the loop gain is $T'_c(s)$, then $T'_c(s)$ can be inferred from

$$\frac{T'_c}{1+T'_c} = \frac{1}{1+\frac{1}{Q_s}\left(\frac{s}{\omega_s/2}\right)+\left(\frac{s}{\omega_s/2}\right)^2}, \tag{4.10}$$

which leads to

$$T'_c(s) = \frac{1}{\frac{s}{\omega_c}\left(1+\frac{s}{\omega_p}\right)}, \tag{4.11}$$

where

$$\omega_p = \frac{(\omega_s/2)}{Q_s} = \frac{\pi\omega_s(D'/D'_{min}-1)}{4}, \tag{4.12}$$

$$\omega_c = (\omega_s/2)Q_s = \frac{\omega_s}{\pi(D'/D'_{min}-1)}. \tag{4.13}$$

It is seen that ω_c is identical to that shown in Fig. 3.3 which identifies the high-frequency asymptote of $T_c(s)$, and hence the sampling effect can be considered responsible for introducing an additional pole ω_p in $T_c(s)$.

It can therefore be concluded that the current-loop gains T_c of Fig. 3.3 may be augmented by the additional pole ω_p to account for the sampling effect.

4.2 Additional Pole ω_p: Second Approach

Another approach to derive the additional pole is presented in this section. The first approach is elegant mathematically, but it is not straightforward physically.

The second approach gives straightforward physical insight into the problem of how to include the sampling effect in current loop at the price of a longer derivation. It uses analog injection as an analytical tool in the context of classical sampled-data theory to

derive a correction factor for current-loop gain. This correction factor is exactly the additional pole derived before. This approach represents a further development of and a significant departure from its original form presented in Part II of [4].

Figure 4.1 shows a sequence of events for deriving a high-frequency correction factor for current-loop gain. Figure 4.1 (a) is a block-diagram representation of a current-programmed converter for the evaluation of current-loop gain. Current-loop gain T_c is the one derived from a low-frequency model such as the unified low-frequency model.

To represent the sampling mechanism, a practical sampler can be introduced immediately in front of the duty-ratio modulator as shown in Fig. 4.1 (b). The term "practical" is used here to imply two things: 1) the sampling is done by a series of pulses, not impulses; 2) the sampling is quasi-periodic. The former will have profound impact on the evaluation of sampled-data current-loop gain. The latter has, as shown before in the previous section, negligible consequence.

Because of the presence of the sampler, current-loop gain is not uniquely defined. Different injection points can produce different current-loop gains. For example, injection at point "b," shown in Fig. 4.1 (c), will define a current-loop gain which corresponds to digital signal injection [19] (more details later).

Injection at point "a," shown in Fig. 4.1 (d), defines a current-loop gain which corresponds to analog signal injection. This is so because the difference of two continuous signals, $(\hat{i}_c - \hat{i}_l)$, is still a continuous signal. An important feature of analog injection at point "a" is that it is possible to absorb the sampler to yield an equivalent analog current-loop gain with the sampling effect accounted for. Indeed, if the big box in Fig. 4.1 (d) is treated as a black box, the block diagram can be reduced to the one shown in Fig. 4.1 (e) with continuous input and output. The resultant gain is a new current-loop gain $T_{cs}(s)$, where subscript "s" indicates the fact that the sampling effect has been accounted for.

The next step is the evaluation of the new current-loop gain $T_{cs}(s)$, which is pursued in the following. Figure 4.1 (d) shows an analog injection measurement, from which one can write

$$\hat{i}_y = \hat{i}_x T_c(s) \tag{4.14}$$

$$\hat{i}_x = \hat{i}_z - \hat{i}_y. \tag{4.15}$$

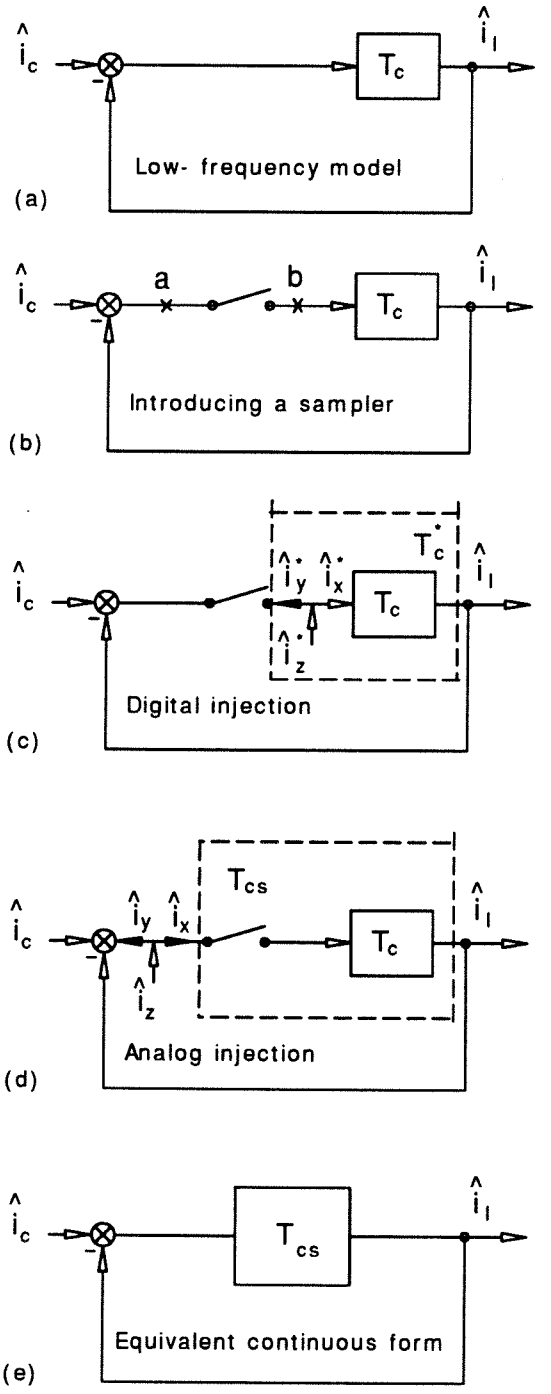

Figure 4.1: Derivation of the additional pole: second approach. A low-frequency current-loop gain is shown in (a); a practical smapler is introduced to account for the sampling effect (b); a digital injection measures a sampled current-loop gain $T_c^* \equiv \hat{i}_y^*/\hat{i}_x^*$ *(c); an analog injection measures a hybrid current-loop gain* $T_{cs} \equiv \hat{i}_y/\hat{i}_x$ *(d); and* T_{cs} *absorbs the sampler to give an equivalent continuous form (e).*

Sampling both sides of the two equations leads to

$$\hat{i}_y^* = \hat{i}_x^* T_c^*(s) \tag{4.16}$$

$$\hat{i}_x^* = \hat{i}_z^* - \hat{i}_y^*, \tag{4.17}$$

where rules for sampling quantities have been applied. From the above four equations, one can derive

$$\hat{i}_y = \frac{T_c}{1+T_c^*}\hat{i}_z^* \tag{4.18}$$

$$\hat{i}_x = \hat{i}_z - \frac{T_c}{1+T_c^*}\hat{i}_z^* \tag{4.19}$$

Since the injected signal $\hat{i}_z$ can be constrained to be a pure sinusoidal signal without loss of generality, the spectrum of the sampled signal $\hat{i}_z^*$ is discrete. Hence, the sidebands generated by sampling will not be seen by a narrowband analyzer. As a consequence, one can write the following equation

$$\hat{i}_z^*(j\omega_{iz}) \approx \hat{i}_z(j\omega_{iz}). \tag{4.20}$$

Using the above simplifying relationship, one can derive the desired expression in a straightforward way. The expression is found to be

$$T_{cs}(s) = T_c(s)\left(\frac{1}{1+T_c^*(s)-T_c(s)}\right). \tag{4.21}$$

Therefore, it is seen that $T_{cs}(s)$ is simply $T_c(s)$, the current-loop gain obtained from the low-frequency model, multiplied by a correction factor $\frac{1}{1+T_c^*(s)-T_c(s)}$.

It needs to be pointed out that one can find the original form of Eq. (4.21) in [4]. What is different here is that the evaluation of $T_c^*(s)$ will depart from the original approach in [4] as elaborated below.

In-depth discussion of sampled-data modeling in [4] collected three equivalent ways to evaluate $T_c^*(s)$ for a given $T_c(s)$. Here, only one approach will be discussed for brevity. For a given Laplace spectrum, say $T_c(s)$, the corresponding sampled-data spectrum $T_c^*(s)$ is given by

$$T_c^*(s) = \frac{1}{T_s}\sum_{n=-\infty}^{\infty} T_c\left(s+\frac{j2n\pi}{T_s}\right), \tag{4.22}$$

which is one particular form of the well-known Shannon's sampling theorem [21], showing explicitly the well-known phenomenon of frequency folding and aliasing.

Unfortunately, this formula cannot be applied directly to the evaluation of the sampled current-loop gain. The reason is that in Shannon's theorem, the sampling process is modeled by a series of impulses. For a physical switching converter, this constraint is too strong to be true. This point can be understood by careful examination of "the sampling process" in an actual switching converter.

Two things need to be discussed. First, in a switching converter, duty-ratio- or current-programmed, a value of duty ratio is determined when the ramp reaches the peak value set by the control signal. The control is actually exercised in a brief, but finite moment, once in a switching cycle, since a small, but finite time duration is required for the modulator to respond. To accomplish it instantaneously, an ideal modulator, i.e., a modulator with instantaneous response time, is needed.

Another aspect is that, in a measurement, duty ratio perturbation is still finite, even if a duty ratio is assumed to be determined instantaneously. This is so because in a measurement at least a perturbation of a few percent has to be provided in order to maintain a certain signal-to-noise ratio at the input port of the analyzer.

In short, "the sampling process" in an actual switching converter is better modeled by a practical sampler. That is, "the sampling" is better modeled by a series of pulses, not impulses. Evaluation of the sampled current-loop gain needs to be pursued accordingly.

Specifically, evaluation of the sampled current-loop gain is pursued by working with geometries of current waveforms to derive discrete expressions. The results from discrete analysis are then followed by application of the modified Padé approximation to translate them into corresponding results in the continuous Laplace domain.

From the geometries of current waveforms in Fig. 2.4, Eq. (4.2) is obtained. Introducing z-transform into it leads to

$$\hat{d}^*(z) = -\frac{1}{2}\left(1 + z^{-1}\right) F_m \hat{i}_l^*(z), \tag{4.23}$$

which, upon substitution of $z = e^{sT_s}$ and use of the concept of equivalent hold, yields

the following expression for the sampled current-loop gain,

$$\hat{d}^*(s) = -\frac{1}{2}\left(1 + e^{-sT_s}\right) F_m \left(\frac{s}{1 - e^{sT_s}}\right) \hat{i}_l(s). \tag{4.24}$$

Substitution of the modified Padé approximation and simplification leads to

$$\hat{d}^*(s) = -F_m \left[1 + \left(\frac{s}{\omega_s/2}\right)^2\right] \frac{1}{T_s} \hat{i}_l(s). \tag{4.25}$$

Refer to Fig. (4.1) (c). The sampled current-loop gain can be written as

$$\begin{aligned} T_c^*(s) &= \frac{\hat{d}_y^*(s)}{\hat{d}_x^*(s)} = -\frac{\hat{d}^*(s)}{\hat{i}_l(s)} \cdot \frac{\hat{i}_l(s)}{\hat{d}_x^*(s)} \\ &= \left[1 + \left(\frac{s}{\omega_s/2}\right)^2\right] T_c(s). \end{aligned} \tag{4.26}$$

Since T_c^* differs from T_c only at the high frequencies, the high-frequency asymptote is sufficient for the expression for T_c, i.e,

$$T_c = \frac{\omega_c}{s}. \tag{4.27}$$

Therefore, the current-loop gain with the sampling effect accounted for is found to be given by

$$\begin{aligned} T_{cs}(s) &= \frac{T_c(s)}{1 + T_c^*(s) - T_c(s)} = \frac{T_c(s)}{1 + T_c(s)\left[1 + \left(\frac{s}{\omega_c/2}\right)^2 - 1\right]} \\ &= \frac{T_c(s)}{\left(1 + \frac{s}{\omega_p}\right)}, \end{aligned} \tag{4.28}$$

where $\omega_p = (\omega_s/2)^2/\omega_c = \pi\omega_s(D'_{min}/D - 1)/4$, which is identical to the value given in Eq. (4.12).

Also, it is seen that accounting for the sampling effect introduces an additional pole ω_p into the current-loop gain, confirming the conclusion in the previous section.

4.3 "Stability Parameter" Q_s and High-Frequency Dynamics

Having identified the additional pole, its influences on the high-frequency dynamics of the current-loop gain can be characterized. It turns out that the parameter Q_s plays an important role in determination of high-frequency dynamics.

The most striking feature of the high-frequency dynamics is that the high-frequency magnitude asymptote is fixed both in its slope and in its position. The asymptote is a straight line with a -40 dB/dec slope and crosses over 0 dB at half the switching frequency $\omega_s/2$. Choice of different values of parameters will only move the low-frequency asymptotes up or down all together. The shape of them remain unchanged. In other words, the actual crossover frequency of the current-loop gain is limited to half the switching frequency. Even though the extrapolated crossover frequency ω_c can approach infinity, the additional pole ω_p will provide sufficient attenuation at high frequencies which limits the actual crossover to half the switching frequency.

High-frequency dynamics are directly determined by the value of Q_s. Two cases of interest, for two values of Q_s, are shown in Figs. 4.2 and 4.3. In each, appropriate expressions for $T_c(0)$ and adjacent corner frequencies can be taken from Fig. 3.3 for the different converters. Increasing K/K_c (larger inductance) increases only the low-frequency range of $T_c(s)$.

In Fig. 4.2 for $Q_s > 0.5$, T_c crosses over at $\omega_s/2$ on a double slope and the resulting closed-loop response, represented by $T_c'/(1+T_c')$, has a corresponding peak at $\omega_s/2$.

In Fig. 4.3, for $Q_s < 0.5$, T_c crosses over at ω_c less than $\omega_s/2$ on a single slope, and the additional pole ω_p is beyond crossover. The resulting closed-loop response has two real poles ω_c and ω_p.

A wealth of useful design-oriented information is available from these low-entropy results. First, the final $-40dB/dec$ asymptote for T_c is fixed in position, crossing 0dB at $\omega_s/2$. Whether current-loop gain T_c crossover occurs at or below $\omega_s/2$ depends solely on Q_s, which is a function of the operating point D' relative to D'_{min} given by Eq. (4.9). In turn, D'_{min} is determined by the slope of the compensating ramp M_c, by Eq. (3.1).

Thus, if all quantities are considered constant except M_c, increasing M_c results in a smaller D'_{min} and a smaller Q_s, lowering ω_c and changing the configuration of T_c from that of Fig. 4.2 towards that of Fig. 4.3. Alternatively, if all quantities are constant except the operating point parameter D', increasing D' (lower D) also results in a smaller Q_s with the same consequences.

Since Figs. 4.2 and 4.3 illustrate the familiar loop-gain/closed-loop relationships for a

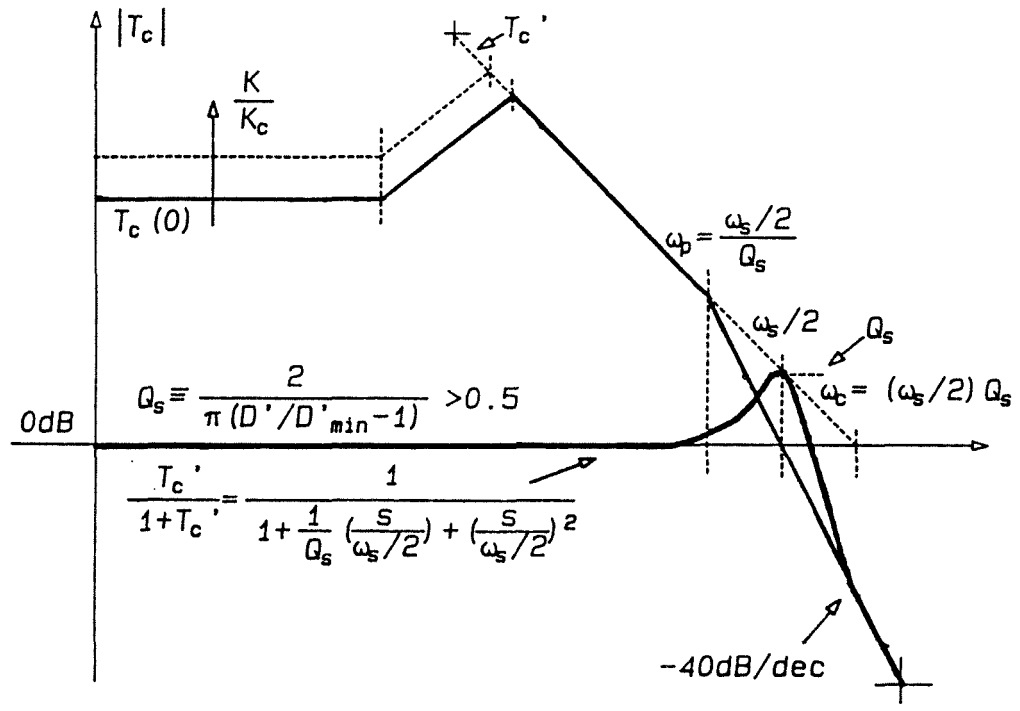

Figure 4.2: Current-loop gain for "stability parameter" $Q_s > 0.5$. T_c crosses over at $\omega_s/2$ on a double slope; closed-loop quadratic peaks up.

single-loop system, in which increasing loop-gain slope at crossover (lower phase margin) leads to peaking in the closed-loop response, it emerges that Q_s is the central quantity of interest in the current-loop gain and could be referred to as a "stability parameter," since Q_s approaches infinity in the stability limit of D' declining to D'_{min}. Further, a smaller Q_s inexorably results in a lower $T_c(0)$.

Finally, a unified model for current-programmed converters with the sampling effect accounted for is obtained by expression of the modulator gain $F_m(s)$ in Fig. 2.2 as $F_m/(1+s/\omega_p)$. Note that the frequency dependence of F_m is an "effective" representation of the sampling effect. A natural-sampled modulator alone does not have any frequency dependence [20].

Various closed-loop transfer functions of interest can be derived from this model, and the low-pass quadratic of Eq. (4.8), in terms of the stability parameter Q_s, appears in

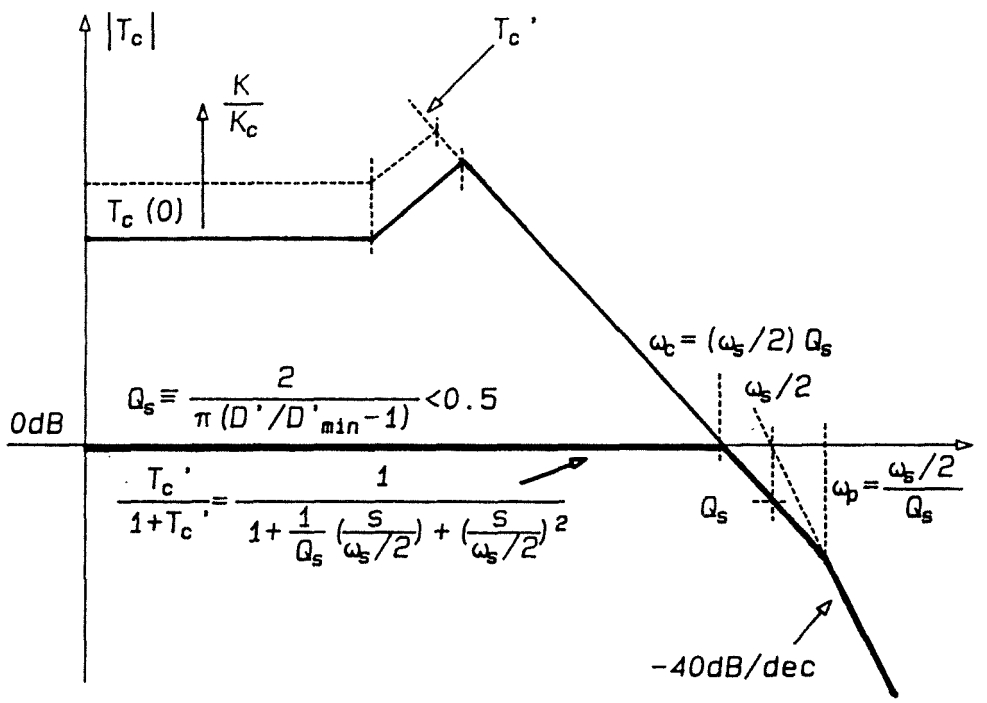

Figure 4.3: Current-loop gain for $Q_s < 0.5$. T_c crosses over at ω_c on a single slope; closed-loop quadratic has real poles at ω_c and ω_p.

all of them.

Chapter 5

Basic Transfer Functions

The unified model having been established, the characteristics of current-programmed converters with the current loop closed can be explored. These characteristics are obtained by derivations of basic transfer functions such as the control-to-inductor-current transfer function, the line-to-output transfer function, the output impedance, and the input impedance. These four transfer functions are important in that they represent the characteristics of a current-programmed converter with the current loop closed. Design of the outer voltage loop can then be pursued in the same way as design of a duty-ratio-programmed converter, treating the four basic transfer functions as those of a "new" plant [5].

5.1 The Preferred Approach

Since three basic converters have only two reactive elements, an inductor and a capacitor, transfer functions are normally second order. However, as discussed previously, the effect of the sampling process, existing inherently in a switching converter, introduces an additional pole ω_p into the current-loop gain. Hence, transfer functions are expected to be third order.

Factorization of a third-order characteristic equation symbolically is not always simple, especially if the factorization is performed to obtain closed-form expressions to gain physical insight. Control of algebra must be exercised at the outset of the derivation in order to lower entropies of expressions [17]. For a current-programmed converter, this can be done in the following fashion.

Recall that the value of the stability parameter Q_s determines the peaking in the closed-loop transfer functions, i.e., it determines locations of the poles. If Q_s is small,

there is no peaking in the closed-loop transfer function. That is, the closed-loop transfer function has two separated poles ω_c and ω_p, where ω_c is determined, among other parameters, by the inductance, and ω_p is the additional pole due to sampling. The only pole left to be found is the one due to the capacitance. Therefore, in the factorization of the third-order characteristic equation, if Q_s is small, one can start with the low-frequency model to find poles due to inductance and capacitance. Then, add ω_p as the third pole. Investigation of the third-order equation is reduced to that of a second-order equation, simplifying greatly the algebra and, in the mean time, lowering entropies of expressions.

Note that this procedure is pursued under the condition that Q_s is small. Extensions to the case where Q_s is large can be achieved readily by invoking the continuity of the transfer function. The unified model is a continuous-time model, and all transfer functions are rational functions which are continuous. By the continuity, any factorization which is valid for the case where Q_s is small should be valid for the case where Q_s is large. Therefore, the results obtained for the case where Q_s is small are equally applicable for the case where Q_s is large.

In addition, derivations of all transfer functions of interest are greatly facilitated by invoking two general properties of linear feedback systems. They are: 1) State variables have the same characteristic equation, provided there are no internal pole-zero cancellations; 2) State-feedback changes the locations of poles, but has no effect on locations of zeros. In other words, zeros are invariant under state-feedback. Establishments of these two properties can be found in standard books on linear systems using state-space formulation, for example, [23].

The first property indicates that once the third-order characteristic equation is found, it can be used for all transfer functions. The second property shows that in deriving transfer functions, one can directly use expressions for zeros obtained for the case of duty-ratio programming. Also, one should realize that once the poles are found, the only thing left to be derived is the dc gains of respective transfer functions.

A buck converter is used throughout this chapter as a working example to illustrate key steps of derivation.

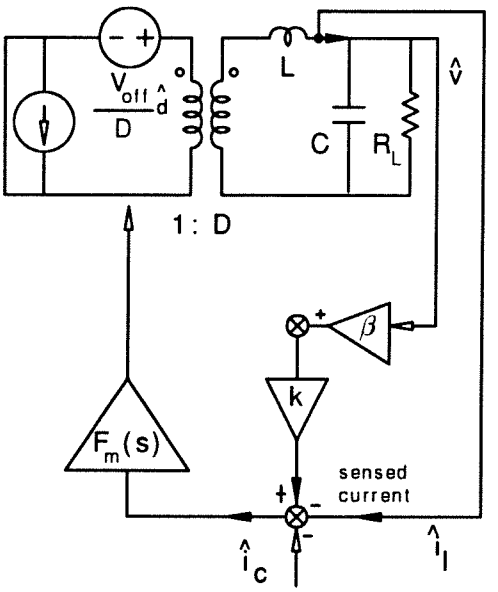

Figure 5.1: Circuit used for evaluation of the control transfer function $G_{vc} \equiv \hat{v}/\hat{i}_c$ for the buck converter under the condition $\hat{v}_g = 0$.

5.2 Control Transfer Functions

Fig. 5.1 is the equivalent circuit used for evaluating the control transfer function for a buck converter, where controlled sources are represented by feedbacks to facilitate evaluation.

From the equivalent circuit, one can write

$$\frac{\hat{v}}{\hat{i}_c} = \frac{F_m H_v(s)}{1 + F_m H_i(s)}, \tag{5.1}$$

where $H_v(s)$ is the duty-ratio-to-output transfer function, and $H_i(s)$ is the duty-ratio-to-current transfer function, which are derived in the following.

$$\begin{aligned} H_v(s) = \frac{\hat{v}}{\hat{d}} &= \frac{V_{off}}{D} \cdot D \cdot \frac{\frac{1}{sC} || R_L}{sL + \frac{1}{sC} || R_L} \\ &= V_{off} \frac{1}{1 + \frac{1}{Q_0}\left(\frac{s}{\omega_0}\right) + \left(\frac{s}{\omega_0}\right)^2}, \end{aligned} \tag{5.2}$$

$$H_i(s) = \frac{\hat{i}_{on}}{\hat{d}} = \frac{V_{off}}{D} \cdot D \cdot \frac{1}{sL + \frac{1}{sC} || R_L} \tag{5.3}$$

$$= \frac{V_{off}}{R_L} \frac{\left(1 + \frac{s}{1/R_L C}\right)}{1 + \frac{1}{Q_0}\left(\frac{s}{\omega_0}\right) + \left(\frac{s}{\omega_0}\right)^2},$$

where

$$\omega_0 \equiv \frac{1}{\sqrt{LC}}, \tag{5.4}$$

$$Q_0 \equiv \frac{R_L}{R_0}, \tag{5.5}$$

$$R_0 \equiv \sqrt{\frac{L}{C}}. \tag{5.6}$$

Substitutions and straightforward algebra leads to

$$G_{vc}(s) = \frac{G_{vc}(0)}{1 + \frac{1}{Q_{vc}}\left(\frac{s}{\omega_0\sqrt{1+T_c(0)}}\right) + \left(\frac{s}{\omega_0\sqrt{1+T_c(0)}}\right)^2}, \tag{5.7}$$

where

$$G_{vc}(0) = \frac{F_m H_v(0)}{1 + F_m H_i(0)} = \frac{R_L}{1 + 1/T_c(0)}, \tag{5.8}$$

$$Q_{vc} \equiv \frac{Q_0\sqrt{1+T_c(0)}}{1 + Q_0 T_c(0) R_L C \omega_0} = \frac{1}{Q_0}\frac{\sqrt{1+T_c(0)}}{T_c(0)}. \tag{5.9}$$

The value of Q_{vc} is small for a converter with a large value for Q_0, which is normally true since high efficiency is always desirable in practical designs. Hence the quadratic can be factored into two separated real roots. Expressions for these two roots are derived as

$$\omega_l = \left[\omega_0\sqrt{1+T_c(0)}\right] Q_{vc} \tag{5.10}$$

$$= \frac{\omega_0}{Q_0}\frac{1+T_c(0)}{T_c(0)}$$

$$= \frac{1}{R_L C}[1 + 1/T_c(0)]$$

$$\approx \frac{1}{R_L C},$$

$$\omega_l' = \frac{\omega_0\sqrt{1+T_c(0)}}{Q_{vc}} \tag{5.11}$$

$$= \omega_0 Q_0 T_c(0)$$

$$= \frac{\omega_s}{\pi}\frac{1}{D'/D'_{min} - 1}.$$

	$G_{vc}(0)$	ω_z	ω_l
Buck	$\frac{R_L}{[1+1/T_c(0)]}$	–	$\frac{1}{R_L C}$
Boost	$\frac{D'(R_L\|\|R)}{[1+1/T_c(0)]}$	$\frac{R}{L/D'^2}$	$\frac{1}{(R_L\|\|R)C}$
Buck/boost	$\frac{D'[R_L\|\|(R/D)]}{[1+1/T_c(0)]}$	$\frac{(R/D)}{L/D'^2}$	$\frac{1}{[R_L\|\|(R/D)]C}$

Table 5.1: Expressions for dc gains and corners of the control transfer function for three basic converters.

Note that $\omega_l' \equiv \omega_c$, the extrapolated crossover frequency of the current-loop gain, showing that the factorization is appropriate.

Therefore, the control-to-output transfer function is of the form

$$G_{vc}(s) = G_{vc}(0)\frac{1}{\left(1+\frac{s}{\omega_l}\right)\left(1+\frac{s}{\omega_c}\right)}. \tag{5.12}$$

As discussed in the previous section, the additional pole ω_p appears in all transfer functions. Also, ω_p, together with ω_c, forms the familiar quadratic. Therefore, for a buck converter, the final form of the control-to-output transfer function is given by

$$G_{vc}(s) = \frac{G_{vc}(0)}{\left(1+\frac{s}{\omega_l}\right)\left[1+\frac{1}{Q_s}\left(\frac{s}{\omega_s/2}\right)+\left(\frac{s}{\omega_s/2}\right)\right]}. \tag{5.13}$$

For the boost, or the buck/boost converter, derivation for $G_{vc}(0)$ is similar except that added algebra is involved caused by the presence of the right-half-plane zero. The right-half-plane zero appears in the transfer function, as revealed by the canonical circuit model for duty-ratio programmed converters. Therefore, the general form of the control-to-output transfer function is

$$G_{vc}(s) = \frac{G_{vc}(0)(1-\frac{s}{\omega_z})}{\left(1+\frac{s}{\omega_l}\right)\left[1+\frac{1}{Q_s}\left(\frac{s}{\omega_s/2}\right)+\left(\frac{s}{\omega_s/2}\right)\right]}, \tag{5.14}$$

where values for $G_{vc}(0)$, ω_z, and ω_l are summarized in Table 5.1 for three basic converters. Values for the boost and the buck/boost are derived by similar procedures.

Several remarks are due here with regard to salient features of the control transfer function. If no compensating ramp is used, Q_s is high, producing peaking at half the switching frequency. This peaking can compromise a designed phase margin if its existence is not recognized. For the well-damped case, i.e., when $Q_s \ll 0.5$, ω_p is well above half the switching frequency. The sampling effect is barely visible. This is precisely the reason why the model in [5] worked even though the sampling effect was not accounted for.

With an even smaller value of Q_s, ω_c will approach ω_l, inducing peaking at $\sqrt{\omega_l \omega_c}$. It can be shown easily that $\sqrt{\omega_l \omega_c}$ approaches ω_0 when Q_s is vanishingly small, where ω_0 is the value of the double pole in duty-ratio programming. In other words, with an increasingly large value for M_c, a current-programmed converter behaves more and more like a duty-ratio programmed converter.

The above remarks about the role that Q_s plays in determination of peaking are also applicable for other closed-current-loop transfer functions to be discussed below. Also, Q-factors similar to Q_s appeared in two previous contributions [8, 9], which described an identical role that Q_s plays.

For the buck converter, if $T_c(0)$ goes to infinity, $G_{vc}(0)$ approaches R_L. This is so because an infinite $T_c(0)$ makes the inductor current an ideal current source. $G_{vc}(0)$ is then simply given by the product of the value of the ideal current source and the load resistance R_L. A similar scenario exists for the boost or the buck/boost converter. The difference is that the load resistance is an effective value as shown in Table 5.1, because of the fact that the inductance is not directly connected to the load resistance.

5.3 Line Transfer Functions

As discussed previously, the line-transfer function is expected to have the same poles as those in the control transfer function. Its zeros will be the same as the duty-ratio-programmed case, which are unities.

All one has to do is to find $G_{vg}(0)$. Fig. 5.2 shows an equivalent circuit for evaluating

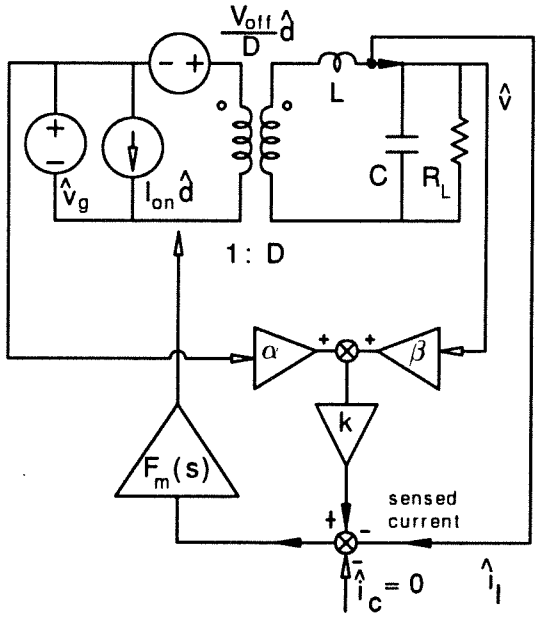

Figure 5.2: An equivalent circuit used for calculation of the line transfer function $G_{vg} \equiv \hat{v}/\hat{v}_g$ *for the buck converter under the condition* $\hat{i}_c = 0$.

the dc gain. Using straightforward circuit analysis techniques, one can find that

$$G_{vg}(0) = M(D)\frac{\left[1 - \frac{1}{1/D'_{min} - 1/D'}\right]}{1 + T_c(0)}. \tag{5.15}$$

For the boost, or the buck/boost converter, the right-half-plane zero does not appear in the line transfer function. Therefore, the line transfer function can be expressed in the following general form

$$G_{vg}(s) = \frac{G_{vg}(0)}{\left(1 + \frac{s}{\omega_l}\right)\left[1 + \frac{1}{Q_s}\left(\frac{s}{\omega_s/2}\right) + \left(\frac{s}{\omega_s/2}\right)\right]}, \tag{5.16}$$

where values of $G_{vg}(0)$ for the buck, boost, and buck-boost converters, are given in Table 5.2.

A significant advantage associated with current programming is that it has better line rejections than those in duty-ratio programming. For increasingly large K, i.e., for increasingly large $T_c(0)$, $G_{vg}(0)$ approaches 0 for the buck, $M(D)/(1 + R/R_L)$ for the

	$G_{vg}(0)$	$M(D)$
Buck	$M(D)\frac{\left[1-\frac{1}{1/D'_{min}-1/D'}\right]}{[1+T_c(0)]}$	D
Boost	$\frac{M(D)}{(1+R/R_L)}\frac{1}{[1+1/T_c(0)]}$	$\frac{1}{D'}$
Buck/boost	$\frac{M(D)}{[1+(R/D)/R_L]}\frac{1}{[1+1/T_c(0)]}\left[1+(1-\frac{1}{1/D'_{min}-1/D'})\right]$	$\frac{D}{D'}$

Table 5.2: Expressions for dc gains of line transfer functions for three basic converters.

boost, and $M(D)/(1+R/DR_L)$ for the buck/boost, revealing that, in general, a current-programmed converter has better line-noise rejection than a duty-ratio programmed one, since $M(D)$ is the dc gain of line transfer functions for duty-ratio programming.

Line noise can actually be rejected perfectly for a buck converter even if $T_c(0)$ is not infinite. For the buck converter, the line noise can be perfectly rejected if a compensating ramp is introduced with its slope equal to that of half the down-slope of inductor current, for which $1/D'_{min}-1/D' \equiv 1$, and $G_{vg}(0) \equiv 0$. This is due to the geometry of the average inductor current. It can readily be shown that this null is extremely sensitive to the value of M_c, hence it is not recommended for any practical designs.

$G_{vc}(0)$ can also be nulled for the buck by allowing $T_c(0)$ to go to infinity, i.e., by introducing an infinite value for the inductance. Its physical meaning is that an infinite value of inductance makes the inductor current behave like an ideal current source, which is insensitive to any perturbation (or noise) in the input. Note that this nulling effect is not present for the boost or buck/boost converter, which reflects the fact that the inductance is not directly connected to the output.

Finally, with an increasingly large value of M_c, i.e., increasingly small value for D'_{min}, $G_{vg}(0)$ approaches $M(D)$ for all three converters, which is exactly the respective dc values of line transfer functions for the case of duty-ratio programming.

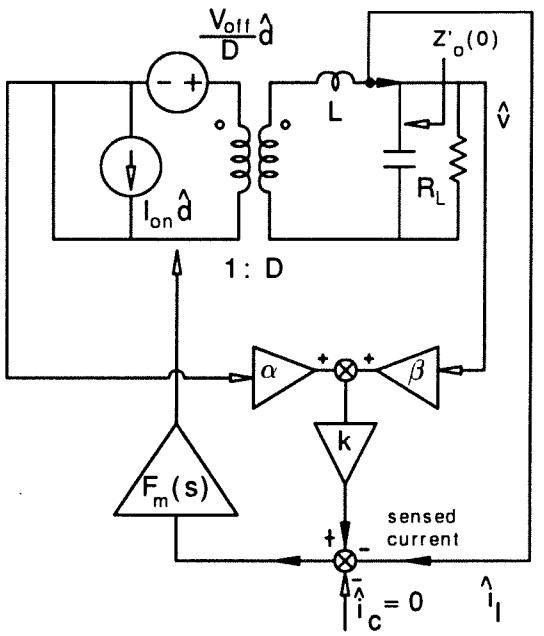

Figure 5.3: An equivalent circuit for evaluation of Z'_o for the buck converter under the condition $\hat{v}_g = 0$ and $\hat{i}_c = 0$. $Z_o(s) = Z'_o(s)||R_L$.

5.4 Output Impedances

The output impedance Z_o(s) is the parallel combination of R_L and Z'_o, where Z'_o is defined as the impedance seen looking into the converter at the two terminals of the load resistance (excluding the resistance).

Output impedances have the same poles as those in the control transfer function, and its zeros will be the same as those for the case of duty-ratio programming. What remains to be done is the evaluation of $Z'_o(0)$. Fig. 5.3 presents an equivalent circuit used for evaluating the dc value. Straightforward calculation yields the following expression for the buck

$$Z'_o(0) = R_L T_c(0). \tag{5.17}$$

Therefore, the output impedance takes on the general form

$$Z_o(s) = R_L||Z'_o(s) \tag{5.18}$$

	$Z_o(0)$
Buck	$R_L T_c(0)$
Boost	$\dfrac{R}{[1+(1+R/R_L)/T_c(0)]}$
Buck/boost	$\dfrac{(R/D)}{\{1+[1+(R/D)/R_L]/T_c(0)\}}$

Table 5.3: Expressions for dc gains of output impedance $Z_o'(0)$ for three basic converters.

$$= \frac{R_L || Z_o'(0)}{\left(1+\frac{s}{\omega_l}\right)\left[1+\frac{1}{Q_s}\left(\frac{s}{\omega_s/2}\right)+\left(\frac{s}{\omega_s/2}\right)\right]},$$

where respective values of $Z_o(0)$ are listed for the three basic converters in Table 5.3.

For a buck, with the increase of K, i.e., with the increase of $T_c(0)$, $Z_o'(0)$ increases monotonically, which reflects the fact that increasing K makes the inductor current behave more and more like an ideal current source, hence an increasingly large output impedance.

Note that with K being increasingly large, the inductor current will be less and less sensitive to any perturbation. In the limit, $Z_o'(0)$ is simply given by the negative value of the ratio of the two control sources, which is R for a boost, and R/D for a buck-boost. These are exactly the numerators of corresponding expressions for $Z_o(0)$ in Table 5.3.

Note also that with the increasingly large M_c, $Z_o'(0)$ goes to zero for all converters, another manifestation of the fact that a current-programmed converter behaves like a duty-ratio-programmed one.

5.5 Input Impedances

Since the driving signal is $\hat{v}_g$ and the response is $\hat{i}_g$, the input admittance, given by the ratio $\hat{i}_g/\hat{v}_g \equiv 1/Z_{in}(s)$, will have the same zeros and poles as other transfer functions.

What is left to be done is to find $Z_{in}(0)$. Fig. 5.4 is an equivalent circuit used for evaluating the dc value for the buck. Straightforward circuit analysis yields the following

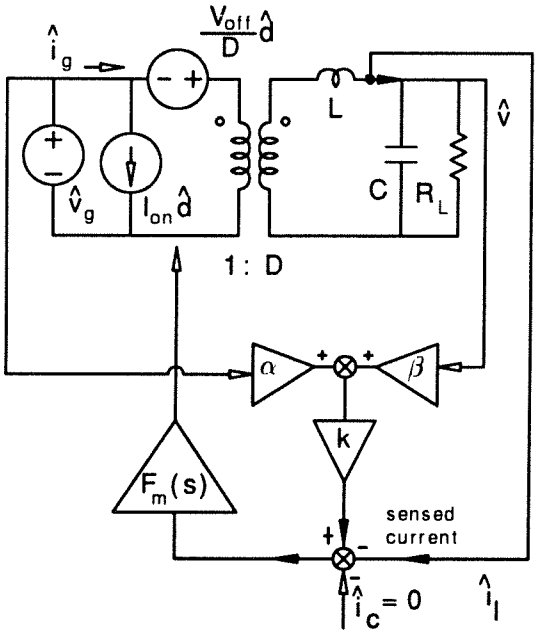

Figure 5.4: An equivalent circuit used for calculation of the input impedance $Z_{in} \equiv \hat{v}_g/\hat{i}_g$ for the buck converter under the condition $\hat{i}_c = 0$.

expression,

$$\begin{aligned} Z_{in}(0) &= \frac{R_L}{M(D)^2} \frac{[1 + T_c(0)]}{1 - (R_L/R)T_c(0)[1 + D'(1 + R/R_L)/K]}, \\ &\approx \frac{R_L}{M(D)^2} \frac{[1 + T_c(0)]}{1 - (R_L/R)T_c(0)}, \end{aligned} \tag{5.19}$$

where the approximation has been made on the ground that the omitted factor is typically in the order of unity.

Thus, the input impedance is of the general form

$$Z_{in}(s) = \frac{Z_{in}(0)\left(1 + \frac{s}{\omega_l}\right)\left[1 + \frac{1}{Q_s}\left(\frac{s}{\omega_s/2}\right) + \left(\frac{s}{\omega_s/2}\right)\right]}{\left(1 + \frac{s}{\omega_L}\right)}, \tag{5.20}$$

where values of $Z_{in}(0)$ for all three basic converters are collected in Table 5.4, and ω_L is the same as those for the case of duty-ratio programming, which is given by $\omega_L = \frac{1}{R_L C}$ for all three converters.

	$Z_{in}(0)$
Buck	$\frac{R_L}{M(D)^2}\frac{[1+T_c(0)]}{[1-(R_L/R)T_c(0)]}$
Boost	$\frac{R_L}{M(D)^2}\frac{[1+T_c(0)][1+T_v(0)]}{[1-(R/R_L)T_v(0)]}$
Buck/boost	$\frac{R_L}{M(D)^2}\frac{[1+T_c(0)][1+T_v(0)]}{[1-(D'/D+R/DR_L)T_v(0)]}$

Table 5.4: Expressions for dc gains of input impedances for three basic converters.

The fact that $Z_{in}(s)$ has the same pole for all three converters can be understood by examining the canonical circuit model for duty-ratio programmed case (recall that poles of $Z_{in}(s)$ are zeros of $1/Z_{in}(s)$, which are invariant under state-feedback). Input current $\hat{i}_g$ is nulled when $\hat{v}$ is zero, which gives $\omega_L = 1/R_LC$. Inductance has no effect on this null since it appears effectively in series with $\hat{i}_g$ in all three converters.

Note that for the buck, when $T_c(0)$ is large, $\omega_L \approx \omega_l$. Thus, Z_{in} has a pole-zero cancellation under this circumstance, reducing its dynamics to that of a double zero. Physical interpretation can be obtained from the canonical model. With an increasingly large value for $T_c(0)$, inductor current behaves more and more like an ideal current source, which decouples effectively the input from the output of the circuit. That is, the input side will not see any dynamics caused by the load resistance and the capacitance. In other words, the only dynamics that the input sees is that due to the inductance (ω_c), and the sampling (ω_p), which is exactly the double zero located at $\omega_s/2$ and characterized by Q_s.

For the buck, with increase of K, i.e., increase of $T_c(0)$, $Z_{in}(0)$ goes to $-\frac{R}{M(D)^2}$. This is similar to duty-ratio programming when the output voltage is tightly regulated. When output dc current is tightly regulated, an incremental increase of the input voltage will excite an incremental decrease of the input current in order to maintain a constant output power, hence resulting in a negative incremental input resistance, which is determined by the values and polarities of two controlled sources. This is precisely why $Z_{in}(0)$ is, among other parameters, in terms of R, the output operating point parameter [5], not

in terms of R_L.

For the boost or the buck/boost, expressions in Fig. 5.4 reveal that a similar scenario exists with $Z_{in}(0)$ given by a similar expression, but with additional scaling factors which merely reflect the fact that for both converters the inductance is not directly connected to the output.

For an increasingly large value of M_c, i.e., an increasingly small value of $T_c(0)$, $Z_{in}(0)$ approaches $\frac{R}{M(D)^2}$ for all three converters, showing again that they are actually duty-ratio programmed under this circumstance.

Finally, the issue of negative input impedance is discussed in the following. Table 5.4 shows that $Z_{in}(s)$ can be a negative impedance at low frequencies for all three converters, if the value of $T_c(0)$ or $T_v(0)$ is large enough. Hence, care must be taken if an input filter is designed for a current-programmed converter to guard against possible onset of oscillations caused by interactions between the output impedance of the input filter and the negative input impedance of the converter.

The buck converter is the most vulnerable, since a relatively low value of $T_c(0)$ can make $Z_{in}(0)$ negative. For example, if $R = R_L$, a value of $T_c(0)$ greater than unity will make $Z_{in}(0)$ negative.

For the boost, or a buck/boost converter, whether or not Z_{in} is negative depends on the value of $T_v(0)$, the dc gain of the nested voltage loop. Note that $T_v(0) = D/(D'/D'_{min} - 1)$ is determined by the duty ratio and the slope of the compensating ramp M_c, and it is independent of the value of inductance, which is different from the buck case where $T_c(0)$, in addition to being related to D and M_c, is proportional to inductance value. In other words, for the boost, or the buck/boost converter, $Z_{in}(0)$ can be made positive by introducing sufficient value for the compensating ramp, which is consistent with the desire to control the value of Q_s, avoiding peaking in the transfer function at half the switching frequency.

Chapter 6

Measurement of Current-Loop Gain

As discussed in Chapter 4, if a sampler is introduced into a model, current-loop gain is no longer uniquely defined. Different injection points define different loop gains. A problem tightly coupled with this ambiguity is measurement of current-loop gain. The uncertainty about proper ways of measuring current-loop gain and lack of thorough understanding of the issue have hindered progress in understanding of current programming, which may have been one of reasons for an unusually large number of different models competing with each other and, in some cases, with conflicting results.

In this chapter, two methods of measuring current-loop gain are discussed in detail. They are: the digital signal injection technique [19], and the analog signal injection technique [22].

It is shown that a digital measurement obtains a sampled version of the corresponding current-loop gain. A practical sampler degrades accuracy of a digital injection measurement, resulting in a measured value for the dc gain which is at least 10 dB below what it should be.

Analog signal injection can be used if the inductor current is sensed. An analog injection measurement is much easier to perform and provides more information. On top of that, contrary to a digital injection measurement, the existence of a practical sampler does not degrade the accuracy of an analog injection measurement. Hence, analog signal injection is the preferred technique for measurement of current-loop gain.

6.1 Digital Signal Injection Measurement

In some cases, current programming is implemented by sensing the transistor current which is pulsating in nature. If a perturbation is introduced, the sensed current is

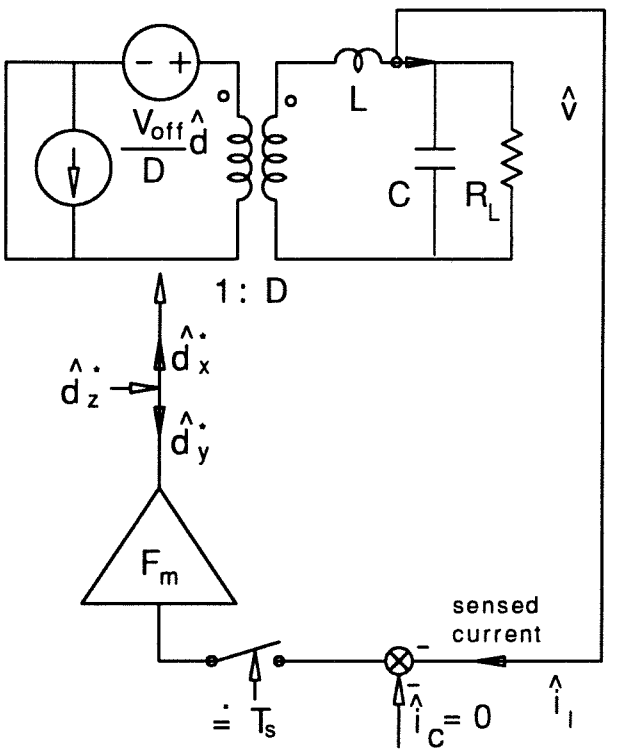

Figure 6.1: Measurement of current-loop gain using digital injection $\hat{d}_z^*$ under the condition $\hat{v}_g = 0$ and $\hat{i}_c = 0$. The measured result $T_c^* \equiv \hat{d}_y^*/\hat{d}_x^*$ is a sampled version of the low-frequency current-loop gain T_c.

both pulse width modulated and amplitude modulated. It is straightforward to see that both modulations contain components at the perturbation frequency. Hence, if a narrowband analyzer is used to measure the perturbation, it will see contributions from both modulations. Data so measured are thus contaminated. To overcome this difficulty, a digital signal injection technique was proposed in [19].

Figure 6.1 illustrates one particular way of representing a digital injection measurement. A digital injection technique injects a perturbation of duty ratio $\hat{d}_z^*$ at the output terminal of the duty ratio modulator. A perturbation is introduced into the digital modulator by reconstruction of a square wave according to the input waveform, but with its

pulse-width determined proportional to an injected analog signal. Hence, one additional PWM driver is necessary for a digital injection measurement.

The following analysis of the digital injection measurement is performed to gain a better understanding of the technique.

To represent its discrete nature, a sampler, shown ahead of the modulator, is introduced. From the simple model in Fig. 6.1, one can write:

$$\hat{d}_y^* = [\hat{d}_x^* G_{di}(s)]^* F_m = [G_{di}(s)F_m]^* \hat{d}_x^*, \tag{6.1}$$

where $G_{di}(s)$ denotes the duty-ratio-to-inductor-current transfer function, and F_m denotes the modulator gain which has been taken to be a real number, although the actual values of these quantities are of no concern for this discussion.

The above equation gives

$$\frac{\hat{d}_y^*}{\hat{d}_x^*} = [G_{di}(s)F_m]^* = T_c^*(s). \tag{6.2}$$

Therefore, the digital injection technique actually obtains a sampled version of current-loop gain $T_c(s)$.

If the sampler is ideal, sampled current-loop gain can be easily evaluated. As shown before, the high-frequency asymptote of current-loop gain can be expressed as $T_c'(s) = \frac{\omega_c}{s}$, whose sampled version is given by, according to [4],

$$T_c'^*(s) = \frac{\omega_c/f_s}{e^{sT_s} - 1}. \tag{6.3}$$

Substitution of the modified Padé approximation and simplification leads to

$$\begin{aligned} T_c'^*(s) &= \frac{\omega_c}{s}\left[1 - \frac{1}{2/\pi}\left(\frac{s}{\omega_s/2}\right) + \left(\frac{s}{\omega_s/2}\right)^2\right] \\ &= T_c'(s)\left[1 - \frac{1}{2/\pi}\left(\frac{s}{\omega_s/2}\right) + \left(\frac{s}{\omega_s/2}\right)^2\right]. \end{aligned} \tag{6.4}$$

Therefore, the overall sampled current-loop gain is obtained as

$$T_c^*(s) = T_c(s)\left[1 - \frac{1}{2/\pi}\left(\frac{s}{\omega_s/2}\right) + \left(\frac{s}{\omega_s/2}\right)^2\right], \tag{6.5}$$

which is exactly the form proposed in [8]. In other words, the sampled current-loop gain can be approximated by adding a double right-half-plane (RHP) zero located at $\omega_s/2$

onto the current-loop gain derived from a low-frequency model, which is accurate up to half the switching frequency. Note that the Q-factor of the RHP double zero has a fixed value $2/\pi$.

As pointed out in the discussion about sampling effect, in a switching converter, a sampler needs to be modeled as a practical sampler, i.e., a sampler which is quasi-periodic and has a finite sampling pulse width. This quasi-periodicity is characterized in [18], where it is shown that in the small-signal limit, the quasi-periodicity is inconsequential. In other words, the sampler can be treated as a periodic device.

The finite sampling pulse width does have a consequence.

Consider a continuous-time signal $g(t)$ with a corresponding spectrum $G(j\omega)$. It can be shown that if sampling is performed with a series of pulses, instead of a series of impulses, the sampled spectrum is given by

$$G_s(j\omega) = \sum_{-\infty}^{\infty} \frac{1}{n\pi} \sin\left(n\pi \frac{t_w}{T_s}\right) G(j\omega - j\omega_s), \tag{6.6}$$

where t_w is the pulse width and T_s is the sampling period. One can see clearly that the finite pulse width introduces increasing attenuation for sidebands.

The attenuation can be better appreciated by considering the fundamental component. If $t_w \ll T_s$, the sampled spectrum is reduced to

$$G_s(j\omega) \approx \frac{1}{\pi} G(j\omega). \tag{6.7}$$

Therefore, the sampled spectrum will have a reduced amplitude. The attenuation is about one third, approximately -10 dB. This provides an explanation of the puzzling question: Why dc gains measured by digital injection are much lower than those obtained by analog injection measurement. This is precisely because of the uniform attenuation inflicted by the finite sampling pulse width, since uniform attenuation appears as dc gain attenuation. More mathematical details are presented in Appendix A at the end of this thesis.

In addition to the attenuation caused by the finite pulse width, the aliasing effect will introduce additional attenuation, since it can be seen that, according to Eq. (6.5),

$$T_c^*(0) = T_c(0) - \frac{1}{D'/D'_{min} - 1}. \tag{6.8}$$

Note that attenuation due to aliasing is proportional to the value of the extrapolated crossover frequency ω_c, which is consistent with the prediction of Shannon's sampling theorem.

Hence, it is concluded that attenuation of at least -10 dB is inherently associated with a digital injection measurement.

Another disadvantage associated with digital injection is that, according to Eq. (6.5), the sampled current-loop gain will always be folded over along half the switching frequency, regardless of the details of the loop gain around half the switching frequency. In other words, information about loop gain there and above will be lost.

In short, a digital signal injection measurement obtains a sampled version of current-loop gain. It is inconvenient to use. The measured value will be at least 10 dB below the actual value. Information around and above half the switching frequency is lost by the effect of frequency folding.

6.2 Analog Signal Injection Measurement

Since a digital injection measurement has several limitations with regard to its accuracy and implementation, an alternative is needed.

This alternative can be found if one property of switching converters is fully appreciated. It can be easily seen that in a 2-switch converter, the transistor current is identical to the up-going portion of the inductor current (in the case of multiple inductors, it will be the sum of all the inductor current). Hence sensing an inductor current is equivalent to sensing a transistor current. As a consequence, the sensed current is nonpulsating, which in turn suggests that a conventional analog signal injection technique [22] can be used. Indeed, an analog signal injection technique can be directly used since the inductor current is normally converted into a voltage in proportion.

Advantages of analog injection are almost exactly the disadvantages associated with digital injection technique. Analog signal injection is easy to use, with no need for special hardware. Practical and analytical details for its applications are well-known throughout the power electronics community, and they are not repeated here.

Since it injects and measures analog signals, no complications associated with sam-

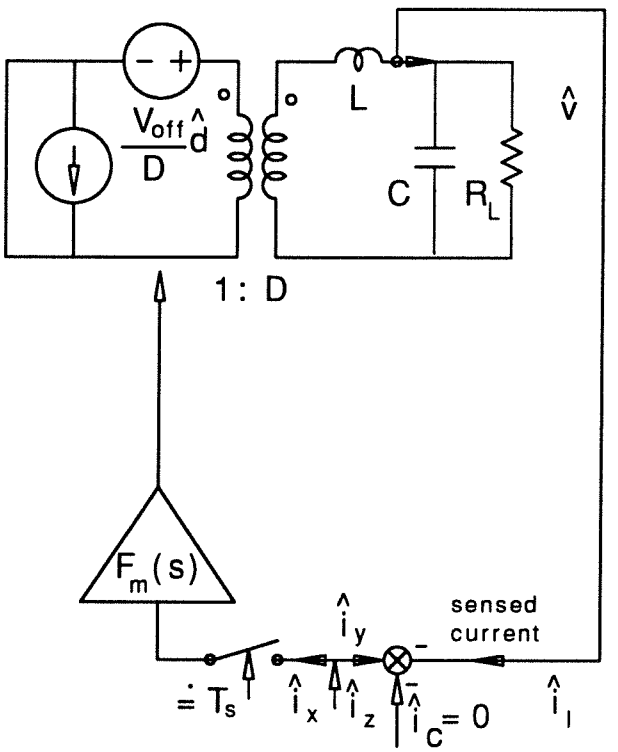

Figure 6.2: Measurement of a current-loop gain by using analog injection $\hat{i}_z$ under the condition $\hat{v}_g = 0$ and $\hat{i}_c = 0$. The measured result $T_{cs} \equiv \hat{i}_y/\hat{i}_x$ is a hybrid version of T_c and T_c^*. Whether a sampler is ideal or practical does not have any impact on the accuracy of an analog injection measurement.

pling exist. In other words, whether a sampler is ideal or practical does not have any impact on analog injection measurement. Thus, information around and beyond half the switching frequency can be obtained accurately at no extra cost. No attenuation associated with finite sampling pulse width exists.

The only requirement is that the inductor current needs to be sensed, which is hardly a constraint at all for the following reason. For the purpose of measuring a current-loop gain, inductor current needs to be sensed. In practical implementations of designs, either transistor current or inductor current can be sensed (because of their equivalence),

depending totally on practical considerations such as circuit reliability, cost, etc., as well as individual preferences.

In summary, analog injection can be used to measure current-loop gain if inductor current is sensed. Its application is just like any conventional analog injection measurement without any further complications. For cases where both techniques are applicable, analog injection is the preferred technique since it outperforms digital injection in all aspects. In the following chapter, measured data by using analog injection exhibit good agreements with analytical prediction, verifying the usefulness of analog signal injection for measurement of current-loop gain.

Chapter 7

Experimental Verifications

To verify theoretical predictions from the unified model and to check the proposed measurement technique, a prototype boost converter and a prototype buck converter have been constructed. Extensive measurements are performed. Analog signal injection is used to measure current-loop gain for the very first time. Good agreements between predictions and measurements are consistently seen for various different values of the duty ratio and the compensating ramp.

Measured current-loop gains for the boost converter are compared with asymptotes of prediction, emphasizing salient features of a current loop, especially the existence of the additional pole ω_s. Measured data for the buck converter are compared with smooth curves of prediction to show accuracy of the proposed unified model. Both sets of measured data support analytical predictions of the unified model, and hence verify the validity of application of analog injection for measurement of current-loop gain.

7.1 Measurements on a Boost Converter

Figure 7.1 shows a test boost converter switching at $50kHz$. The nonpulsating inductor current is sensed, and the input voltage source is floated to permit the current sense resistor to be connected to power ground. The LM234 is introduced to reduce noise in the sensed current waveform and to allow convenient analog voltage injection at its output for measurement of current-loop gain T_c.

Various values of compensating ramp slope M_c are used to establish corresponding values of D'_{min} and stability parameter Q_s. All measurements are made at a converter operating point $D = 0.4$, $D' = 0.6$ which allows both a margin for modulation and a large value of Q_s so that possible peaking at $f_s/2$ is exposed.

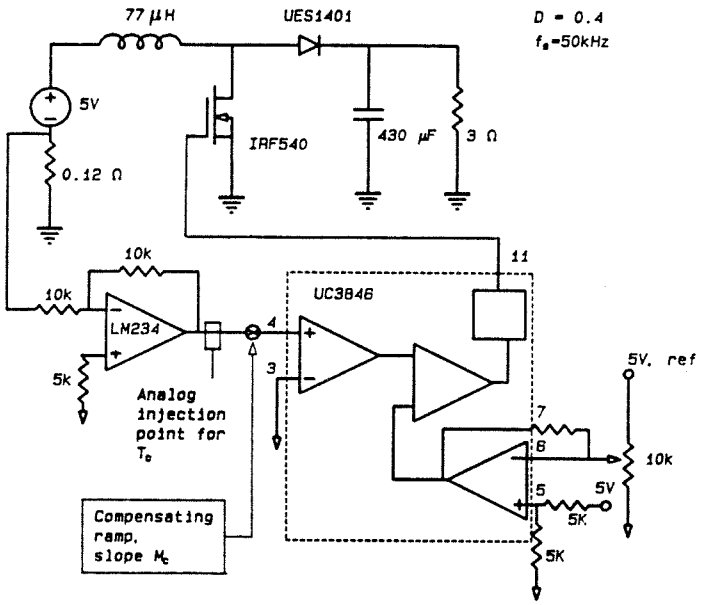

Figure 7.1: Test boost converter.

Figure 7.2 shows the predicted asymptotes and measured results of current-loop gain for $D'_{min} = 0.5$ (no compensating ramp, $M_c = 0$). Since the operating point is $D' = 0.6$, little larger than D'_{min}, Q_s is high: from Eq. (4.9) $Q_s = 3.2 > 1$, from Eq. (4.12) the additional pole is at $f_p = 7.9kHz$, and the unified model predicts that T_c crosses over at $f_s/2 = 25kHz$ on a double slope. Agreement between prediction and measurement is good, and the presence of the additional pole ω_p can clearly be seen, especially from the phase measurement.

Figure 7.3 shows the same comparison for $D'_{min} = 0.37$ ($M_c = M_2/2$), together with additional magnitude asymptotes as predicted from models in [5, 7, 8], respectively. Since in the unified model $Q_s = 1.1 > 1$, $f_p = 25/1.1 = 24kHz$ and $f_c = 25 \times 1.1 = 27kHz$ are very close to $f_s = 25kHz$, in good agreement with measurement. On the other hand, f_c is predicted respectively at $16kHz$, $40kHz$, and $10kHz$ by the models in [5, 7, 8]. Because of the fact that the corner ω_p is very close to the crossover frequency ($25kHz$), the measured result crosses over at less than $20kHz$. It can therefore be concluded that predictions from [5, 8] tend to be lower, while the prediction from [7] tends to be higher than the actual value. The existence of ω_p is also seen in the amplitude and phase

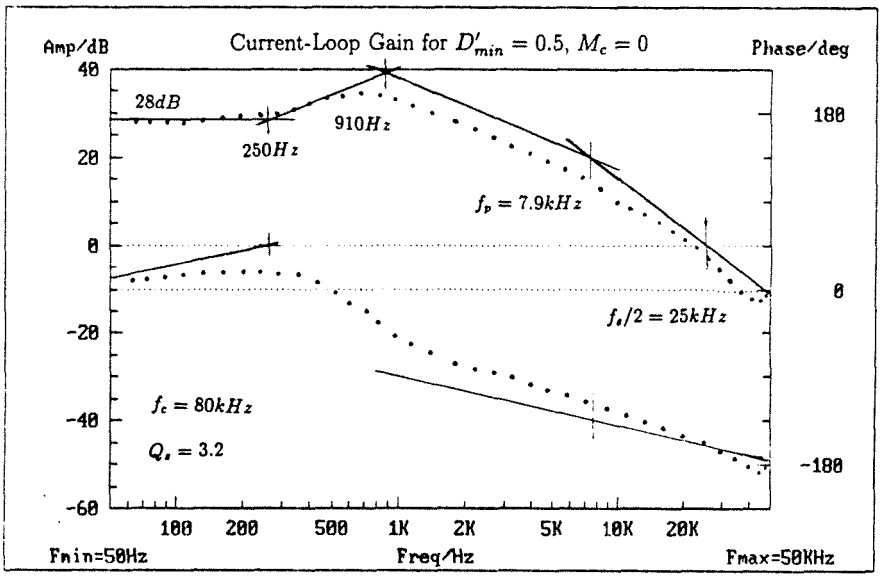

Figure 7.2: Measured results (data points) and prediction (in asymptotes) of current-loop gain for a boost converter with $D'_{min} = 0.50$. Existence of ω_p is clearly seen.

measurements.

Figure 7.4 shows again good agreement between the unified model prediction and the measured results of current-loop gain for $D'_{min} = 0.3$ ($M_c = M_2$). Since $Q_s = 0.64$ is now less than unity, T_c crosses over on a single slope near $f_c = 0.64 \times 25 = 16kHz$, showing that improved stability is obtained by increasing the compensating ramp to give a lower Q_s.

Figure 7.5 shows one more time good agreement between the unified model prediction and the measured data for the case where $D'_{min} = 0.2$ ($M_c = 2M_2$). Since $Q_s = 0.35$, much less than unity, T_c crosses over on a single slope near $f_c = 0.35 \times 25 = 8.8kHz$. It is seen that the effect of the additional pole is negligible, since it is located at $f_p = 25/0.35 = 71kHz$, well above half the switching frequency. The current-loop for this case is fairly much like a single pole system at high frequencies.

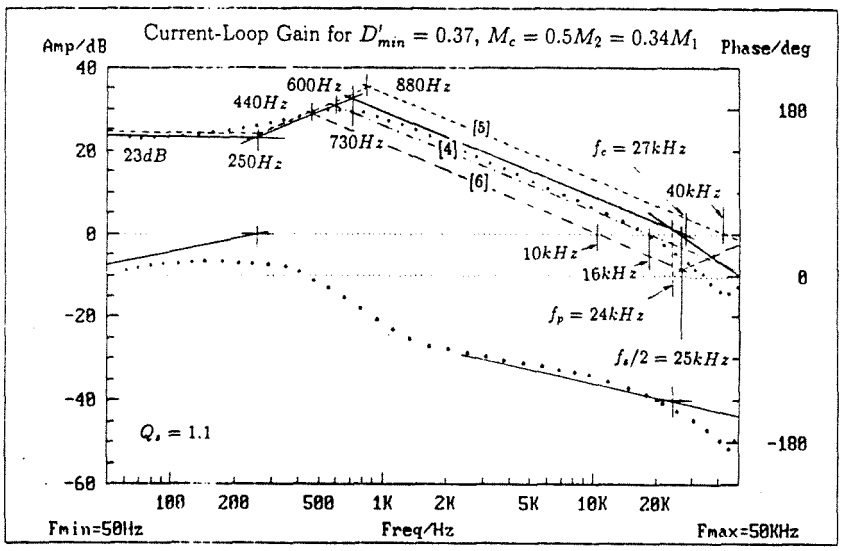

Figure 7.3: Measured results (data points) and predicted asymptotes of current-loop gain for a boost converter with $D'_{min} = 0.37$. Solid asymptotes: unified model; others: according to indicated Reference numbers.

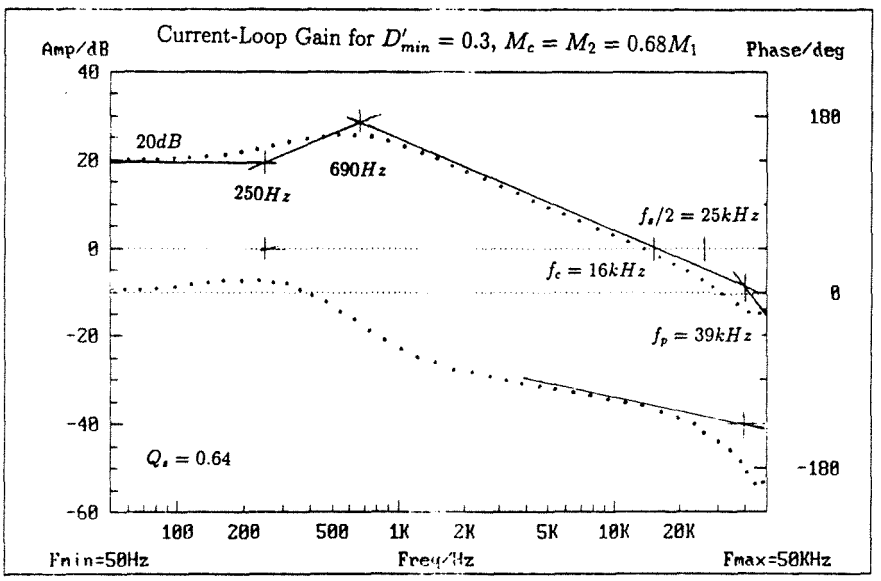

Figure 7.4: Measured results (data points) and predicted asymptotes of current-loop gain for a boost converter with $D'_{min} = 0.30$. The additional pole ω_p lies above $\omega_s/2$.

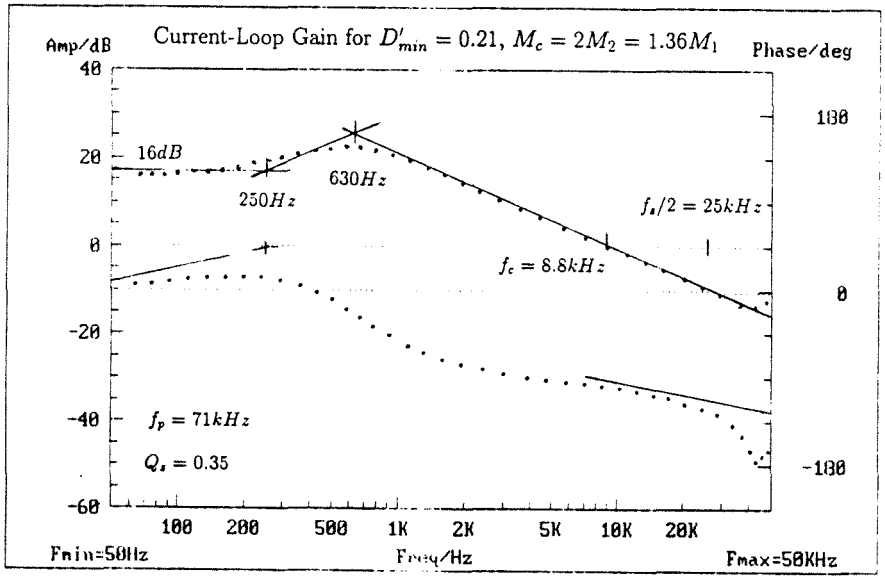

Figure 7.5: Measured results (data points) and predicted asymptotes of current-loop gain for $D'_{min} = 0.20$. The additional pole ω_p lies well above $\omega_s/2$.

7.2 Measurements on a Buck Converter

Figure 7.6 shows a test buck converter operating at $50kHz$. The nonpulsating inductor current is sensed resistively. Two LM234s are used to reduce noise in the sensed inductor current, and to allow convenient analog signal injection.

Various values of compensating ramp slope M_c are used to establish corresponding values of D'_{min} and Q_s. All measurements are made at a converter operating point $D = 0.45, D' = 0.55$. A high value for duty ratio is intentionally chosen for the buck converter to test the accuracy of prediction of the unified model, since predictions are expected to degrade drastically as current-loop approaches its limit for stability. This is so because of one unique feature of a buck converter, which is that the dc gain $T_c(0)$, unlike the cases for a boost or a buck/boost, is expected to become unbounded in the stability limit. Hence, test under this situation is more demanding than lower values of duty ratio for the unified model.

Figure 7.7 shows the predicted smooth curves and measured results of current-loop gain for $D'_{min} = 0.5$ ($M_c = 0$). Since the operating point is $D' = 0.55$, little larger than

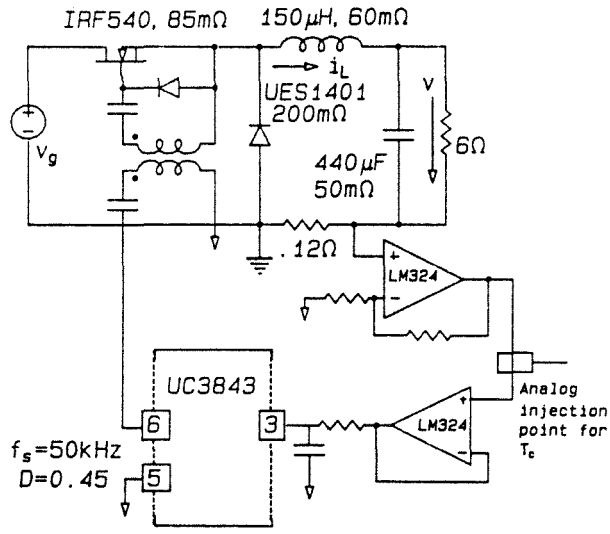

Figure 7.6: Test buck converter.

D'_{min}, Q_s is very high: from Eq. (4.9) $Q_s = 6.4 > 1$, from Eq. (4.12) the additional pole is at $f_p = 3.9kHz$, and the unified model predicts that T_c crosses over at $f_s/2 = 25kHz$ on a double slope. Agreement between prediction and measurement is good, and the presence of the additional pole ω_p can clearly be seen, especially from the phase measurement.

Figure 7.8 shows the same comparison for $D'_{min} = 0.37$ ($M_c = M_2/2$). Since $Q_s = 1.2 > 1$, $f_p = 25/1.1 = 21kHz$ and $f_c = 25 \times 1.2 = 29kHz$. Good agreement between two smooth curves is again seen in the entire frequency range of interest. The existence of ω_p is also seen in the amplitude and phase measurements.

Figure 7.9 shows again good agreement between the unified model prediction and the measured results of current-loop gain for $D'_{min} = 0.3$ ($M_c = M_2$). Since $Q_s = 0.64$ is now less than unity, T_c crosses over on a single slope near $f_c = 0.64 \times 25 = 16kHz$, showing that improved stability is obtained by increasing the compensating ramp to give a lower Q_s.

Figure 7.10 shows one more time good agreement between the unified model prediction and the measured data for the case where $D'_{min} = 0.2$ ($M_c = 2M_2$). Since $Q_s = 0.35$, much less than unity, T_c crosses over on a single slope near $f_c = 0.35 \times 25 = 8.8kHz$.

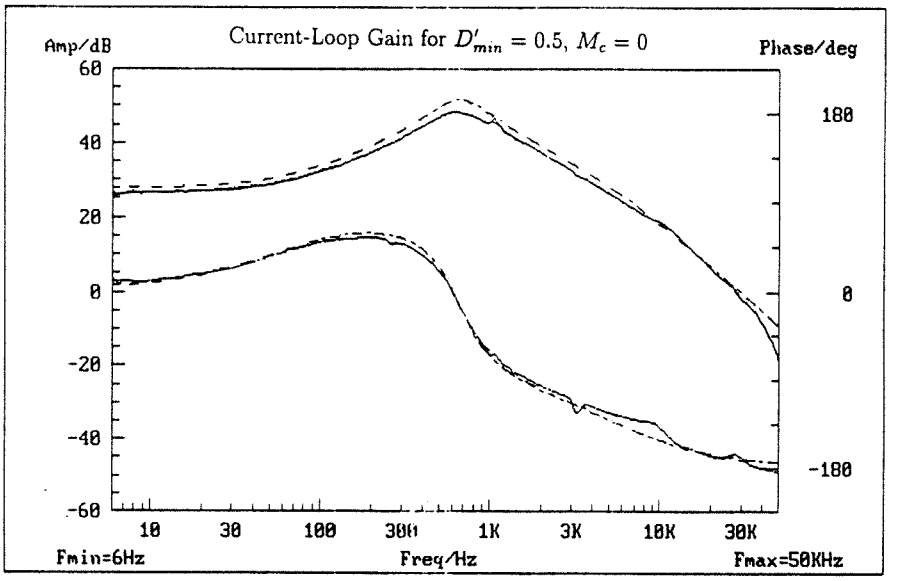

Figure 7.7: Measured results (data points) and prediction (in asymptotes) of current-loop gain for a buck converter with D'_{min} = 0.50. Good accuracy of the unified model predictions are clearly seen.

It is seen that the effect of the additional pole is negligible, since it is located at $f_p = 25/0.35 = 71kHz$, well above half the switching frequency. The current-loop for this case is much like a single pole system at high frequencies. Good agreement between two smooth curves is seen one more time.

Reviewing all comparisons, it is concluded that the predictions for a buck converter by the unified model are verified. Note also the double pole of the current-loop gain is shown to be fixed by the measured data for a buck converter. In other words, different mechanisms for current loop to go to instability are confirmed by measured data.

In summary, experimental measurements on boost and buck converters agree consistently well with predictions by the unified model. It is therefore concluded that the unified model is theoretically sound and experimentally verified.

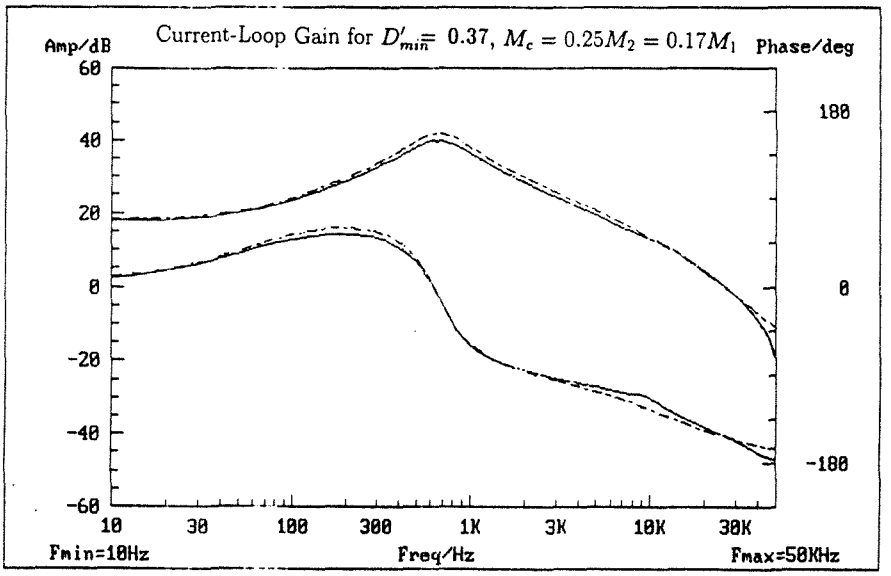

Figure 7.8: Measured results (data points) and predicted asymptotes of current-loop gain for a buck converter with $D'_{min} = 0.40$. Good accuracy of the unified model predictions are clearly seen.

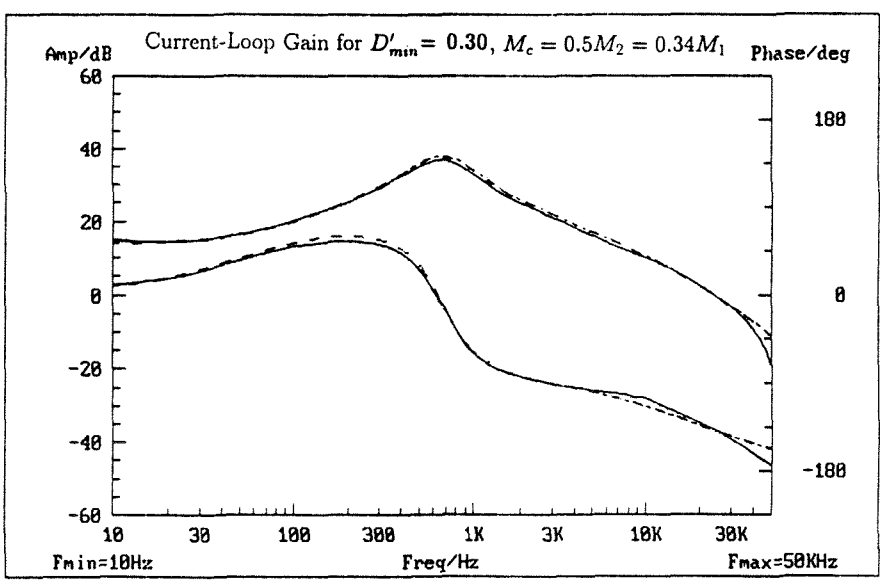

Figure 7.9: Measured results (data points) and predicted asymptotes of current-loop gain for a buck converter with $D'_{min} = 0.30$. The additional pole ω_p lies above $\omega_s/2$. Good accuracy of the unified model predictions are clearly seen.

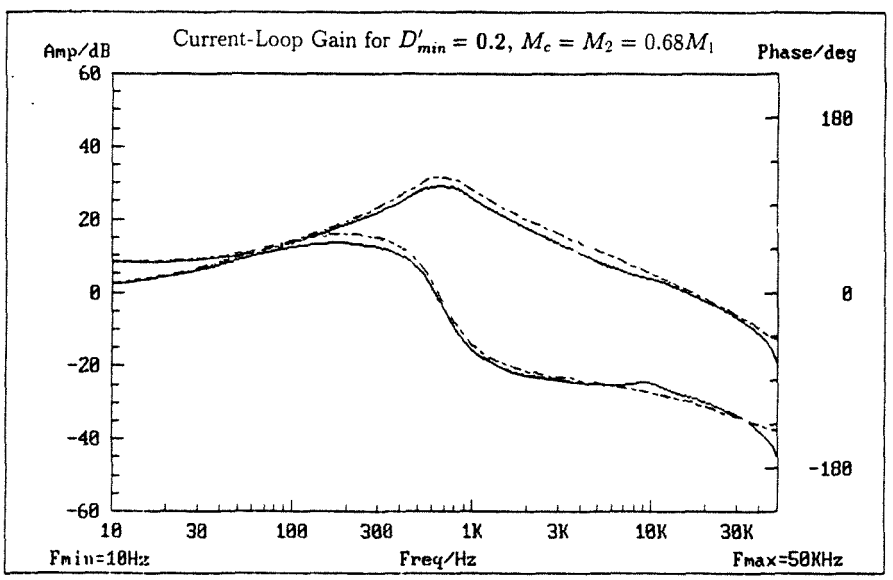

Figure 7.10: Measured results (data points) and predicted asymptotes of current-loop gain for a buck converter with $D'_{min} = 0.20$. The additional pole ω_p lies well above $\omega_s/2$. Good accuracy of the unified model predictions are clearly seen.

Chapter 8

Conclusions

A unified model for a current-programmed converter is established as in Fig. 2.2. Although the format is the same as in [5], a modified modulator model leads to correspondingly modified expressions for F_m and k as given in Eqs. (2.13) and (2.14), and also for the loop gain $T_c(s)$ shown in Fig. 3.3.

It is well-known that use of a compensating ramp of slope M_c extends upwards from 0.5 the limit of the duty ratio D for which stability is maintained. It is found convenient to introduce a new parameter D'_{min}, defined by M_c as in Eq. 3.1, which represents the minimum value of the complementary duty ratio $D' = 1 - D$ for which stability is maintained.

It is also well-known that the instability is caused by the sampling effect, which is not accounted for in the loop gain shown in Fig. 3.3. The sampling effect is here accounted for by an extension of the previous model from which the presence of an additional pole ω_p in $T_c(s)$, given by Eq. (4.12), is inferred and incorporated in the modulator gain $F_m(s)$ in Fig. 2.2, since they appear in cascade.

The presence of the additional pole ω_p causes the final high-frequency asymptote of $T_c(s)$ to be $-40dB/dec$, as shown in Figs. 4.2 and 4.3. A salient feature is that this final asymptote is fixed in position, crossing zero dB at $\omega_s/2$, and that consequently the loop-gain crossover frequency cannot exceed half the switching frequency regardless of any component values or converter operating point. Whether crossover occurs at or below $\omega_s/2$ is determined by the value of the operating point D' relative to D'_{min} through another parameter Q_s defined in Eq. (4.9). The "stability parameter" Q_s emerges as the central quantity of interest in the current-loop gain $T_c(s)$, since its value determines not only the crossover frequency but also the degree of peaking, which always occurs at $\omega_s/2$, in the low-pass quadratic of Eq. (4.8) that is contained in all of the closed-loop transfer

functions.

To answer the question: why in actual measurements, for the same converter and under the same test conditions, the measured value obtained by using digital injection is much less than the value obtained by using analog injection, an analytical investigation is conducted. It is revealed that inherent limitations exist for accuracy of a digital signal injection measurement [19]. The dc value of current-loop gain measured by digital injection is at least $10dB$ below what it should be because of the finite pulse width of the practical sampler, a model for the sampling process in switching converters. Aliasing effect is another source of the attenuation. To avoid complications caused by finite pulse width of the practical sampler, analog injection [22] can be used. It is found that analog injection outperforms digital injection in all aspects for the cases where both of them are applicable.

The unified model is verified by experimental measurements of current-loop gain on a test boost converter and on a buck converter, respectively. Agreements between predictions and measured data are consistently good. An analog signal injection technique is enabled by sensing the (nonpulsating) inductor current instead of the pulsating switch current, which does not change the nature of the current loop. Figure 7.2 and Fig. 7.7 show $T_c(s)$ for $Q_s = 3.2$, and 6.4, respectively, for a boost and for a buck. Q_s has a high value since $D' = 0.6, 0.55$ are little larger than $D'_{min} = 0.5$; the presence of the additional pole ω_p at $7.9kHz$, and $3.9kHz$, respectively, well below crossover, is clearly visible.

The effect that the compensating ramp M_c has on the current loop is clearly seen to be the stabilizing effect in Figs. 7.2 through 7.5, as well as in Figs. 7.7 through 7.10. Current loop loses its stability when the corresponding current-loop gain loses its phase margin, an identical mechanism to that of a classical second-order low-pass system. Subtle differences in the way that current-programmed converters go to instability are also verified.

Part II

A Generic Averaged Model for Switches in Dc-to-Dc Converters

Chapter 9

Introduction

Modeling of large- and small-signal dynamics in dc-to-dc switching converters is a fundamental and challenging issue. It is fundamental since a converter needs to be modeled properly to allow closed-loop design to form a regulator which meets the design specifications in a robust manner. It is challenging since, as far as the terminal relationship between voltage and current is concerned, switches are nonlinear elements [24].

One important step to take at the outset is the formulation of the modeling problem. Different formulations may lead to vastly different levels of difficulty in obtaining a model. If the modeling problem for a switching converter is approached in the context of nonlinear analysis, the solution is very likely to be complicated. Consequently, physical insight is obscured and hard to obtain. That is, one is likely to obtain results with high-entropy expressions (expressions that are complex and provide no insight into the physics going on behind the mathematics). In many cases, general closed-form solutions are very hard, if not impossible, to obtain.

Fortunately, for a switching converter, one can write a state-space description to formulate a linear time-varying system, or piecewise linear system, if a time-varying switching function is defined properly to describe the duty ratio [4]. Major advantages of this formulation include: 1) A sufficient condition for the existence and uniqueness of a solution can be established (see Appendix B for details); and 2) The solution can easily be found by direct integration of the state-space description over each respective subinterval, and then piecing together the results by using the continuity of the states at the switching instants [12].

In other words, the unique solution to the linear time-varying system can readily be found, without having to resort to complicated mathematical formalism for time-varying systems. Successful efforts in this direction have led to the establishment of the method

of state-space averaging, initiated in [28], and culminated in [12].

The end result is an elegant canonical circuit model for three basic converters. In essence, state-space averaging replaces a linear time-varying state-space description for a switching converter by a linear time-invariant state-space description by averaging (smoothing) out ripples at the switching frequency.

As discussed in [28, 12], averaging can be considered as low-pass filtering. Low frequency information is retained and high-frequency information is sacrificed purposely to trade for simplicity of the model, which in turn reveals a wealth of physical insight into the small-signal dynamics of switching converters. Because of its simplicity, state-space averaging has gained wide acceptance. The principle behind state-space averaging has found even wider applications in modeling dc-to-dc switching converters other than PWM (see, for example, [15] and [29]-[33]).

Another aspect of modeling a switching converter, which has received much attention recently, is applications of models for computer simulations. While the canonical circuit model is extremely useful in obtaining low-entropy analytical results, it is less powerful in simulation applications, because of the fact that the locations of switches and reactances in converters are not necessarily the same as those represented in the canonical model. This inconvenience is the consequence of the facts that the canonical model is a model for converters and that it is over-manipulated for elegance in form.

The model of PWM switches given in [34] remedies the situation by establishment of a model for two switches in a PWM converter. The derivation of the model of PWM switches taps into the fact that there exists an inherent PWM tree structure in any PWM converter, which consists of two switches and one inductance. Frequently, but not necessarily, this structure is connected as a three-terminal device [16, 15]. Interactions between two switches and the rest of the converter, which is time-invariant, can be characterized by its terminal voltages and currents, in much the same way as modeling a transistor by an equivalent small-signal circuit. The model of PWM switches is extended to cover converters in discontinuous conduction mode in the second part of [34], and in current programming [9] by rendering the model into an equivalent y-parameter form. While representing a step forward, the model of PWM switches is still inconvenient when

applied to some converters in which two switches don't share a common node. This is due to the fact that two switches don't necessarily have to share a common node in order to realize PWM switching [16]. Moreover, versions of the model for discontinuous conduction mode and for current programming have their forms different from the one for PWM converters, which may be inconvenient for simulations.

An internal report [38] proposed a brand-new way of modeling switches. This approach uses the volt-second and amp-second balance equations to derive large- and small-signal models for switches. The end result was a four-terminal model for two switches in PWM converters. Switches in converters in discontinuous mode, in current programming, and in other modes of operation were not tackled. Relationships of the four-terminal model to previous models, converter-wise or switch-wise, were not investigated.

One unique aspect of modeling for simulation purpose is that a large-signal model is sufficient to simulate large- and small-signal dynamics of a converter. This is so because of the ability of simulation software packages to predict small-signal dynamics if a large-signal model is available. Specifically, if a large-signal model is available, small-signal dynamics can be obtained by doing analog injection into the loop of interest in the simulated converter, in much the same way as doing analog injection to a real physical converter. Discussions and applications of averaged large-signal models can be found, for example, in [35, 36, 37].

Various efforts have focused on developing models which are "exact." See, for example, [4, 18]. A detailed discussion can be found in [4], where comparisons of discrete-time, sampled-data, and state-space averaging approaches are made to enhance the understanding of similarities and differences among three typical approaches. The modeling approach in [18] is exact in the small-signal limit. It starts from discrete-time analysis, and then translates important results from discrete-time to that of continuous-time by use of the concept of "equivalent hold," an important and useful technique. While all models enjoy better performance at high frequencies than state space averaging, they all suffer from complexity of the model which is typified by presence of complex exponentials in expressions for quantities of key interest. Quantities with expressions in terms of complex exponentials make physical interpretations very hard, if not impossible, to

obtain, which is exactly opposite to what low-frequency model is capable of.

Since the ultimate goal of any modeling technique is to aid design, simplicity is a virtue. Hence, in the following, efforts will be focused on predictions of large- and small-signal low-frequency dynamics. There are two main reasons for adopting this approach: 1) averaging can faithfully retain low-frequency information, while simplifying greatly the derivation; 2) even in cases where high-frequency information has to be retained, it is preferable to augment a low-frequency model with additional elements than to derive a new model from scratch.

Chapter 10 derives the balance equation for switches in dc-to-dc converters by introducing a time-varying model for individual switches. The approach here is a refined version of the one in [38]. Chapter 11 establishes a low-frequency small-signal model for two switches for constant-frequency, constant-on-time, and constant-off-time controls, respectively. Since the model has an identical form for three different control strategies, it is called the generic averaged model for two switches in dc-to-dc converters. Chapter 12 is devoted to extension of the generic model to converters with isolation transformers. Chapter 13 presents extension of the generic model to converters in discontinuous conduction mode by employing the concept of equivalent duty ratio. A discussion about the theoretical aspects of the equivalent duty ratio is presented. A significant result is that averaging can always retain low-frequency information contained in the original quantity regardless of its ripple content as long as the average value of the original quantity is not vanishingly small. Salient features of the model are discussed. Chapter 14 discusses the extension to current-programmed converters. This extended model provides a convenient alternative for simulations, with respect to the unified model presented in part 1 of the thesis. A y-parameter version of the generic model reveals that y_{22} is always positive. Hence, one can see explicitly that current programming introduces lossless damping to give improved small-signal dynamics. Chapter 15 addresses the issue of extension to converters with multiple switches. A three-switch converter is characterized for its large- and small-signal dynamics to illustrate the usefulness and generality of the proposed approach. Design guidelines are also discussed for the three-switch converter. Chapter 16 summarizes major results obtained.

Notation conventions adopted here are as follows. Capital letters are used to indicate quantities associated with steady-state, hatted letters are quantities associated with small-signal perturbations, and small letters represent quantities associated with perturbed state, i.e., quantities which are the sum of capital and hatted letters.

Chapter 10

The Balance Equation for Two Switches

In a circuit, volt-seconds for an inductance and/or ampere-seconds for a capacitance have to be balanced within one switching cycle in order to maintain a steady state. Equations describing these required balances are frequently called balance equations. Balance equations are used more frequently in power electronics than other fields of electrical engineering. This is so because, in addition to meeting fundamental circuit laws such as Kirchhoff voltage and current laws (KVL and KCL), a switching converter has to satisfy all the balance equations for inductances and capacitances in order to have a non-trivial steady state. In other words, balance equations for switching converters are equally as fundamental as KVL and KCL. More important, it opens up a brand-new avenue for characterizations of switching converters.

If balance equations for switches in the environment of a converter can be established, one can expect that the balance equations will play a fundamental role in modeling behaviors of switches. The difficulty lies in the fact that switches are not energy-storage elements, and hence no balance equations can directly be written for them. A time-varying model for a switch is established to provide the means for writing the balance equation.

For convenience of discussion, the constraint of small-ripples for inductor current and capacitor voltage is assumed in this and the next chapters. The constraint is later relaxed by introduction of the concept of the equivalent duty ratio.

It needs to be pointed out that the idea of using balance equations to investigate dynamic behaviors of switches was originated in [38], of which discussion here is a much refined version.

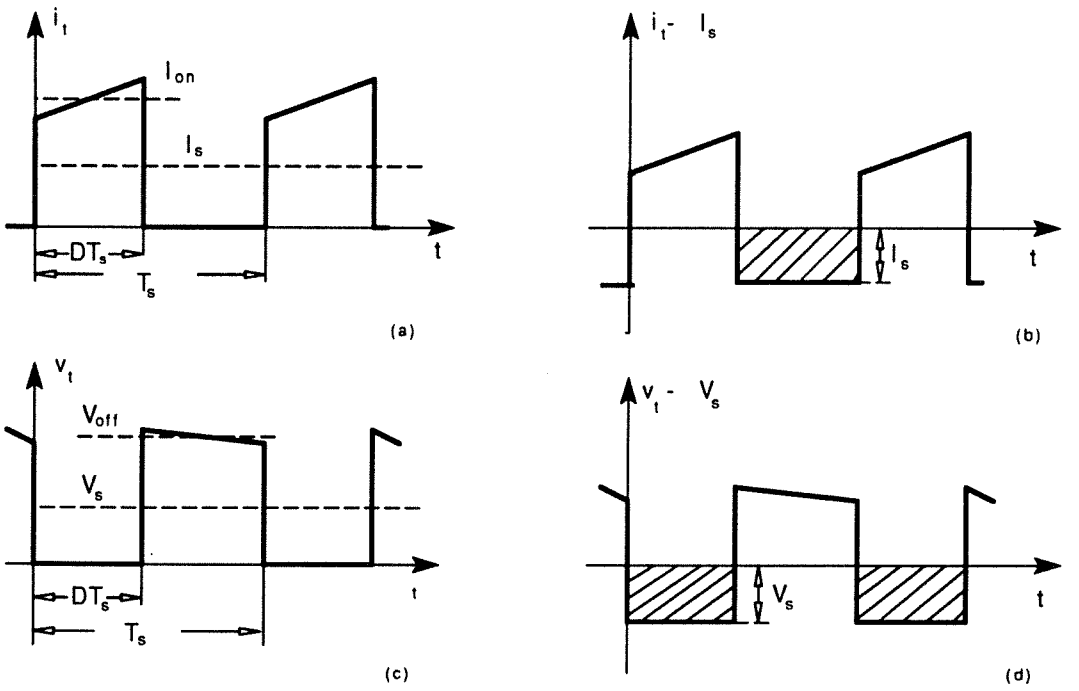

Figure 10.1: Typical waveforms of switch voltage and current in a dc-to-dc converter with small ripples. Removal of the dc component V_s from v_t, shown in (a), results in a pure ac waveform $v_t - V_s$ (b). Removal of the dc component I_s from i_t, shown in (c), results in a pure ac waveform $i_t - I_s$ (d).

10.1 A Time-Varying Model for a Switch

Figure 10.1 (a) and (c) shows typical waveforms of the voltage across, and the current through, a switch. The average values of the voltage and the current over one switching cycle can be defined respectively as

$$V_s = \frac{1}{T_s}\int_{nT_s}^{(n+1)T_s} v_s dt, \tag{10.1}$$

and

$$I_s = \frac{1}{T_s}\int_{nT_s}^{(n+1)T_s} i_s dt. \tag{10.2}$$

One can then decompose the waveforms into two parts: the first part is the dc value of the waveform, and the second is the first (at the switching frequency) and the higher harmonics. Removal of the dc component V_s from v_t, shown in Fig. 10.1 (a), results in a pure ac waveform $v_t - V_s$ shown in Fig. 10.1 (b). Removal of the dc component I_s from i_t, shown in Fig. 10.1 (c), results in a pure ac waveform $i_t - I_s$ shown in Fig. 10.1 (d).

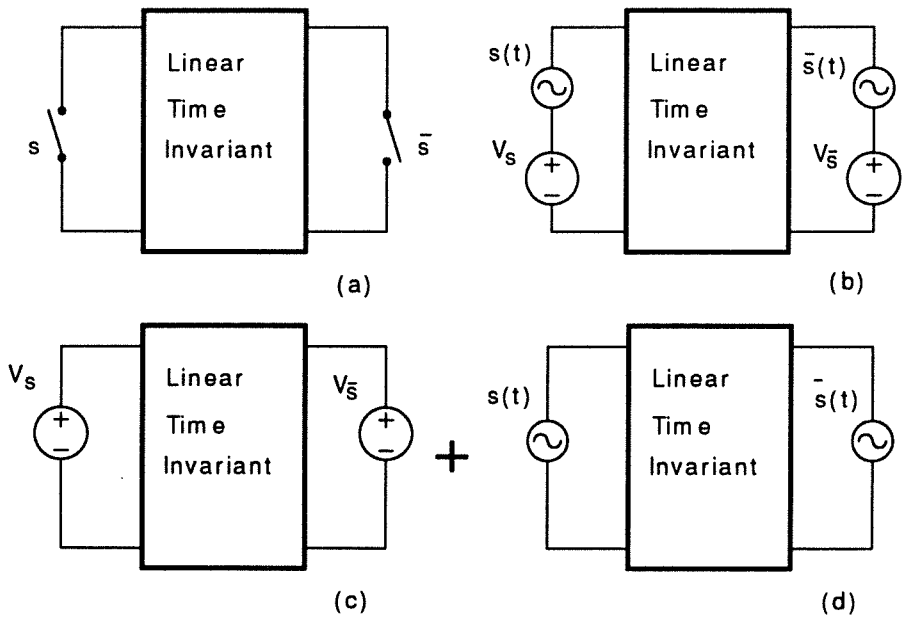

Figure 10.2: A two-switch converter has two switches and a linear-time-invariant subcircuit (a); the time-varying model for a switch is substituted in to obtain an equivalent circuit (b); then the circuit can be characterized at two equivalent circuits (c) at dc, and (d) at ac (the switching frequency).

The decomposition shows explicitly an important feature of the waveforms. First, both the waveforms have flat bottoms regardless of what dc values they may have. Second, the negative values are given exactly by the corresponding dc values. If one defines a model by using the bottom part of the waveform, the model will be given in terms of dc quantities. Therefore, one can see that the following dc and ac models can be defined according to the waveforms.

The dc model can be defined as

$$v_s = V_s. \tag{10.3}$$

The ac model can be defined as

$$s(t) = \begin{cases} -V_s, & \text{switch on} \\ -I_s, & \text{switch off.} \end{cases} \tag{10.4}$$

Several remarks are in order here.

The dc model has been defined in terms of averaged switch voltage V_s for convenience, since switching converters are predominately used for voltage-to-voltage conversions. Of course, if desired, the dc model can be defined in terms of dc current I_s as well. This is true because of the well-known property of substitution for a linear circuit [24].

The modeling approach is unique in that the model focuses on the value of switch current (zero value) when the switch is off, and on the value of switch voltage (zero value) when the switch is on. That is, zero values of switch current and voltage are unfolded to allow analysis to proceed in places where it has been considered impossible to do. This approach is different from all previous modeling efforts, which focused on the voltage when the switch is off (since switch voltage is determined by outside circuitry when switch is off), and on the current when the switch is on (since switch current is determined by outside circuitry when switch is on).

The ac model for the switch is time-varying, which reflects the time-varying nature of a switching converter. Although it is not useful per se for any analysis, it does provide a powerful tool to investigate switch dynamics as to be shown later.

Another useful feature of the model is that it is fully determined if the dc values of voltage and current are known. That is, the ac model is in terms of dc quantities.

Characteristics of a converter with small ripples can be obtained by obtaining its behaviors at dc (zero frequency) and at ac (the switching frequency), respectively. That is to say, analysis of a converter can be pursued at separate frequency scales: one at dc and the other at ac (the switching frequency). Figure 10.2 is a block-diagram representation of the idea. A two-switch converter is represented by two switches and a linear-time-invariant subcircuit in Fig. 10.2 (a). When the time-varying model for a switch is substituted in, one obtains an equivalent circuit in Fig. 10.2 (b). Then the circuit can be characterized at two equivalent subcircuits: Fig. 10.2 (c) at dc and Fig. 10.2 (d) at ac (the switching frequency). The overall converter characteristics can then be obtained by the principle of superposition, which is applicable here since the rest of the converter is linear and time-invariant.

Finally, note that the time-varying model for the switch is applicable to analysis of a converter in transients as well, since average values for switch voltage and current are

defined locally (in one switching cycle).

10.2 Concepts of Dc and Ac Circuits

One important feature of the equivalent circuits for dc and for ac (switching frequency) is that the linear time-invariant part of the converter is reduced to simple wire connections in both cases. Hence, further investigation of the phenomenon may be useful, which leads to the concepts dc and ac equivalent circuits.

Behaviors of switches in a converter are determined by two basic constraints. One is that in any converter, there must exist a PWM tree structure [15, 16], which guarantees the required turn-on and turn-off of the switches (commutations). The other is the requirement that a converter has to have a connected graph at dc in order to ensure proper voltage conversion.

The dc equivalent circuit for a converter is obtained by shorting all inductances and opening all capacitances. Fig. 10.3 shows dc circuits for six basic converters, respectively, where the plus and minus signs indicate the assumed positive direction for the voltage drops across switches.

Salient features of the dc circuit can now be seen. The dc circuit consists of switches, input, and output elements. No reactances are associated with it. The dc circuit is a connected graph which ensures proper voltage conversion. The dc conversion ratio can be found from the dc circuit when the dc model for switches are substituted in.

The ac circuit is the equivalent circuit at the switching frequency. It is determined by the PWM structure alone. At switching frequency, under the constraint of small ripples, inductances can be taken to be open circuits, and capacitances can be taken to be short circuits. Thus, the PWM tree structure is reduced to a parallel combination of two switches as illustrated in Fig. 10.4. Note that the input voltage source is considered as a stiff capacitance as well.

It needs to be emphasized that the ac circuit consists of switches only. If the ac model for a switch is substituted into the ac circuit for a converter, one can investigate behaviors of switches in terms of dc quantities, which are the balance equations introduced next.

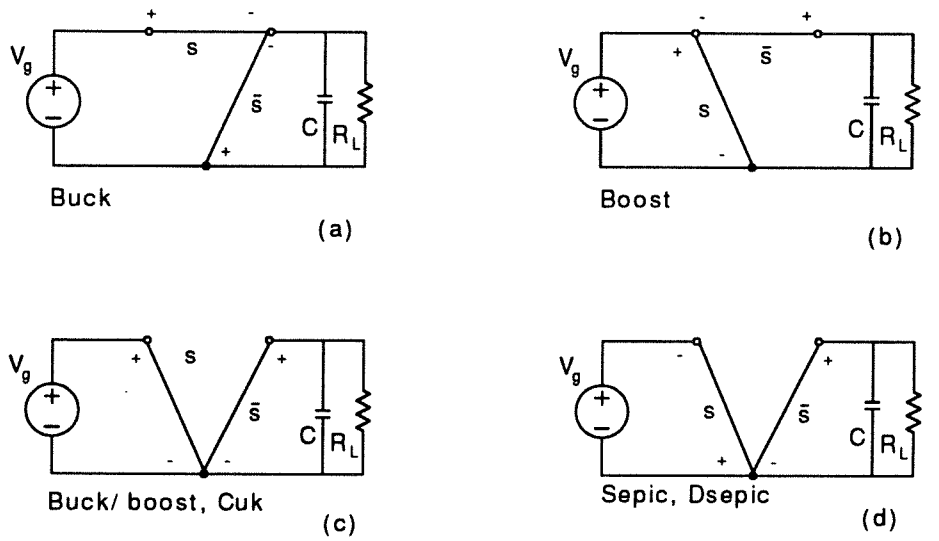

Figure 10.3: The dc circuit identified for six basic converters. The plus and minus signs indicate the assumed positive directions for the voltage drop across switches.

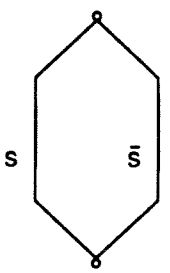

Figure 10.4: The ac circuit identified for six basic converters.

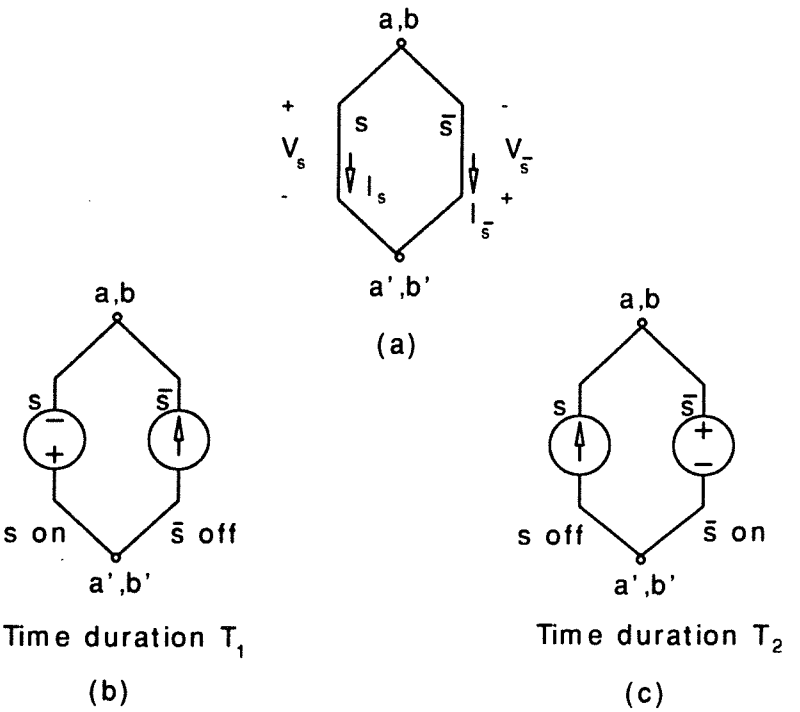

Figure 10.5: Writing the balance equation for two switches. The plus and minus signs indicate the assumed positive directions for voltage drops across switches and the arrows show the assumed positive directions for currents through respective switches (a); the equivalent circuit for time duration T_1 when s is on and $\bar{s}$ is off (b); the equivalent circuit for time duration T_2 when s is off and $\bar{s}$ is on (c).

10.3 The Balance Equation

Establishment of the ac circuit for converters provides a way of writing the balance equation for switches.

Consider a converter with a switch s, and a switch $\bar{s}$, switching in a complementary manner. The ac equivalent circuit is shown in Fig. 10.5 (a), in which the plus and minus signs indicate the assumed positive directions for voltage drops across switches and the arrows show the assumed positive directions for currents through respective switches. Substitutions of the time-varying model for switches s and $\bar{s}$, respectively, into the ac circuit yields the equivalent circuits shown in Fig. 10.5 (b) and (c). The equivalent circuit shown in Fig. 10.5 (b) is for the time duration T_1 when s is on and $\bar{s}$ is off. The equivalent circuit shown in Fig. 10.5 (c) is for the time duration T_2 when s is off and $\bar{s}$ is on.

Recall that the ac circuit has no dc component. Hence, in a steady state, volt-

seconds and ampere-seconds accumulated for the time duration T_1 should be equal to those accumulated for the time duration T_2, i.e.,

$$\begin{cases} V_s T_1 - V_{\bar{s}} T_2 = 0, \\ I_{\bar{s}} T_1 - I_s T_2 = 0, \end{cases} \tag{10.5}$$

where again T_1 is the on-time of the active switch, and T_2 the off-time of the active switch.

Equation (10.5) is the balance equation for two switches in a switching converter with small ripples. The balance equation (ac phenomenon at switching frequency) is given in terms of dc quantities, V_s, $V_{\bar{s}}$, I_s, $I_{\bar{s}}$, T_1, and T_2, and hence provides inherent connections between ac and dc quantities.

A physical interpretation of the balance equation is presented here to help drive home the idea. The balance equation is a modeling tool developed to model dynamics of switches in a converter. In general, the volt-second balance is actually dictated by the inductance which would appear in parallel with switches if it were retained during modeling steps, and the ampere-second balance is actually decided by the capacitance which would be in series with the switches if it were kept during the modeling process. In other words, the balance equation for switches are in fact a set of respective balance equations for inductance and capacitance, but in terms of dc quantities associated with switches.

Establishment of the balance equation provides the means to derive large- and small-signal models for switches in a systematic manner, which is explored in the next chapter.

Chapter 11

A Generic Averaged Model for Switches in Dc-to-Dc Converters

The balance equation for switches derived in the previous chapter is studied further. Perturbation of the balance equation yields a generic averaged equivalent circuit model for two switches in the environment of a switching converter with small ripples. This equivalent circuit incorporates large- and small-signal dynamics for switches into a single circuit model in a way similar to the canonical model derived for converters from the method of state-space averaging.

One important feature of the approach, which separates it from previous modeling approaches, is that it can readily be generalized to N (a positive integer) switches in switching converters. Details about the generalization is presented in a later chapter.

The generic model is then applied to converters with three different control strategies: constant frequency (frequently referred to as PWM), constant on-time, and constant off-time. The reduced form of the generic model for the three control strategies suggests that understanding of converters with constant-frequency control (PWM converters) is fundamental.

It is also shown that the model of PWM switches [34] is a special case of the generic model. Also, if the generic model is applied to a particular converter, the resultant equivalent circuit is identical to the canonical circuit model proposed in [12].

In short, the results in [12, 34] are extended by perturbation of the balance equation to yield a generic averaged model. Low-frequency dynamics of switches can now be predicted truly at switch level, i.e., switches can be handled as linear-time-invariant two-terminal circuit elements if one is interested only in their low-frequency characteristics. One may conclude that a long journey for the power electronics community to find a

simple way to model switches is now completed.

11.1 Perturbation of the Balance Equation

For a converter with a complementary pair of switches s and $\bar{s}$, the balance equation for them is of the form

$$\begin{cases} V_s T_1 = V_{\bar{s}} T_2 \\ I_{\bar{s}} T_1 = I_s T_2, \end{cases} \tag{11.1}$$

which is a description of the energy balance in a converter under steady state.

According to the method of state-space averaging [12], the low-frequency dynamics can be obtained by introducing perturbations into the quantities corresponding to steady state (or dc operating point). Perturbation of the balance equation yields

$$\begin{cases} (V_s + \hat{v}_s)(T_1 + \hat{\tau}_1) = (V_{\bar{s}} + \hat{v}_{\bar{s}})(T_2 + \hat{\tau}_2) \\ (I_{\bar{s}} + \hat{i}_{\bar{s}})(T_1 + \hat{\tau}_1) = (I_s + \hat{i}_s)(T_2 + \hat{\tau}_2), \end{cases} \tag{11.2}$$

where perturbations for time are expressed as τ, instead of t, with proper subscripts to distinguish them from time instants.

Expansions and rearrangement leads to the following two sets of equations,

$$\begin{cases} V_s T_1 = V_{\bar{s}} T_2 \\ I_{\bar{s}} T_1 = I_s T_2, \end{cases} \tag{11.3}$$

and

$$\begin{cases} \hat{v}_s = -\dfrac{V_s}{T_1}\hat{\tau}_1 + \dfrac{T_2}{T_1}\hat{v}_{\bar{s}} + \dfrac{V_{\bar{s}}}{T_1}\hat{\tau}_2 \\ \\ \hat{i}_{\bar{s}} = -\dfrac{I_{\bar{s}}}{T_1}\hat{\tau}_1 + \dfrac{T_2}{T_1}\hat{i}_s + \dfrac{I_s}{T_1}\hat{\tau}_2, \end{cases} \tag{11.4}$$

where products of perturbations have been dropped because of the small-signal constraint.

Equation (11.3) can be rewritten as

$$\begin{cases} \dfrac{V_s}{V_{\hat{s}}} = \dfrac{T_2}{T_1} \\ \dfrac{I_s}{I_{\hat{s}}} = \dfrac{1}{(T_2/T_1)}, \end{cases} \tag{11.5}$$

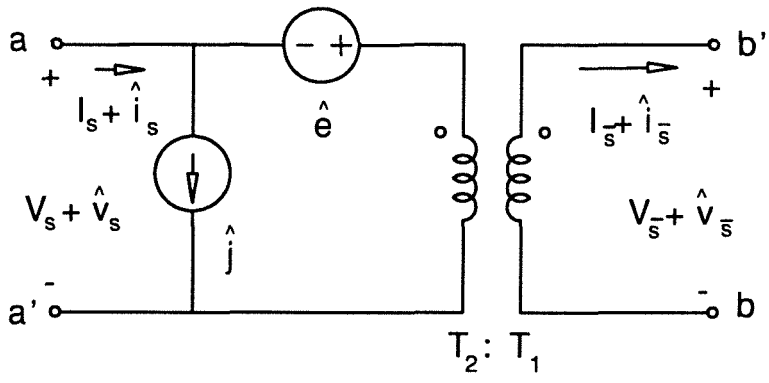

Figure 11.1: An equivalent circuit model for two switches generated by perturbation of the balance equation. The conceptual transformer has a "turns ratio" T_2/T_1, which reflects the inherent switching action in switching converters. The conceptual transformer is valid all the way down to dc.

which is identical to equations for an ideal transformer with "turns ratio" T_2/T_1, suggesting that an transformer equivalent circuit may be obtained.

From Eq. (11.3) and Eq. (11.4), one can derive an equivalent circuit model as shown in Fig. 11.1, where

$$\begin{cases} \hat{e} = \dfrac{1}{T_s}(V_s\hat{\tau}_1 - V_{\bar{s}}\hat{\tau}_2) \\ \hat{j} = \dfrac{1}{T_2}(I_{\bar{s}}\hat{\tau}_1 - I_s\hat{\tau}_2). \end{cases} \tag{11.6}$$

Since this model is valid for any converter topologies and for three typical control strategies, it is called the generic averaged model for two switches in converters with small ripples, or simply, the generic model.

Several remarks are in order here.

The generic model is similar to the well-known equivalent circuit model for an ideal conventional two-winding transformer. The equivalent circuit for the active switch s, implemented as a transistor, corresponds to "the primary," and the passive switch $\bar{s}$, implemented as a diode, corresponds to "the secondary." Furthermore, the positive directions of voltages and currents on both sides indicate that the active switch always

acts as a load, while the passive switch always behaves as a source, which is consistent with the fact that in a converter, the product of the voltage across and the current through the active switch (transistor) is always positive, and the corresponding product for the passive switch (diode) is always negative.

The "turns ratio" of the equivalent transformer is $T_2/T_1 = D'/D$, which is the ratio of the off-time over the on-time of the active switch. Hence, switching action in a converter makes two switch branches coupled together in a way similar to linear time-invariant controlled sources. The control quantity is the on-time duration of the active switch T_1. Note that the conceptual transformer is valid all the way down to dc.

The model has two major functions. The first one, described by Eq. (11.3), is to predict large-signal behaviors of switches in steady state. An additional function of the large-signal model, which is useful but less obvious, is that it can also be used for averaged large-signal transient analysis. This is true because there was not a single limitation placed on the value of duty ratio during the derivation of Eq. (11.3). Note that the only implicit condition for Eq. (10.5) to be true is that an average value can be well defined, which guarantees the existence of decompositions of switch voltage and current into respective dc and ac components, therefore validating Eq. (11.3).

The second function, described by Eq. (11.4), is to model averaged small-signal dynamics of switches around a steady state. In the model, the steady state is represented in the form of dc quantities V_{off}, I_{on}, and D, frequently called parameters for the dc operating point. (The two terms, "the steady-state solution" and "the dc operating point" are frequently used interchangeably in practice.) Since the generic model has four terminals, its applications are easier than the model of PWM switches in [34], truly simple point-by-point substitution. This advantage is particularly handy for applications of the model for computer simulations.

Another salient feature of the generic model is that it can be easily extended for converters in modes of operation other than PWM. Furthermore, all extended models will be exactly the same in form, an attractive feature for simulations.

The equivalent circuit model in Fig. 11.1 is a much refined version of that in [38]. The final form of the original model in [38] was not exactly a transformer equivalent circuit,

which obscures the physical insight.

Results to be derived from now on are original.

11.2 A Reduced Form of the Generic Model

In this section, three most common control strategies for converters with small ripples are discussed, which leads to a reduced form of the generic model.

The generic model for two switches is discussed specifically for three common control strategies: constant frequency control, constant on-time, and constant off-time. It is shown that a single reduced form of the generic model is representative of all three cases.

Constant-Frequency Control

Constant frequency control is also called pulse-width-modulation (PWM) control. In the control strategy, the switching frequency is kept constant, and regulation is realized by variations of the width of the control signal pulse. The pulse width is frequently characterized by introduction of a quantity known as duty ratio. Hence, constant frequency control is also known as duty-ratio programming.

Under this control strategy, any perturbation for the on-time will have to be balanced by a perturbation of the off-time with the same magnitude but in opposite direction, i.e.,

$$\hat{\tau}_2 = -\hat{\tau}_1. \tag{11.7}$$

Upon substitution of Eq. (11.7) into expressions for the voltage source and the current source, one has

$$\frac{1}{T_1}(V_s\hat{\tau}_1 - V_{\bar{s}}\hat{\tau}_2) = \frac{V_s + V_{\bar{s}}}{D}\frac{\hat{\tau}_1}{T_s} = \frac{V_{off}}{D}\hat{d}, \tag{11.8}$$

and

$$\frac{1}{T_2}(I_{\bar{s}}\hat{\tau}_1 - I_s\hat{\tau}_2) = \frac{I_s + I_{\bar{s}}}{D}\frac{\hat{\tau}_1}{T_s} = \frac{I_{on}}{D'}\hat{d}, \tag{11.9}$$

where $V_{off} \equiv V_s + V_{\bar{s}}$ and $I_{on} \equiv I_s + T_{\bar{s}}$. Voltage V_{off} is the voltage stress a switching device has to sustain when it is in off state, and current I_{on} is the current stress a switching device has to sustain when it is in on state.

	$E(V_{off}, D)$	$J(I_{on}, D)$
Constant frequency	$\frac{V_{off}}{D}$	$\frac{I_{on}}{D'}$
Constant on-time	V_{off}	$\frac{I_{on} D}{D'}$
Constant off-time	$\frac{V_{off} D'}{D}$	I_{on}

Table 11.1: Expressions for sources in the reduced form of the generic model for two switches.

Constant-On-Time Control

Under constant-on-time control, the on-time of the active switch s is kept constant, and regulation is realized by changing the switching period (variable frequency). Hence, there is no perturbation for the on time, and any perturbation in switching period is equal to that of the the off-time of the active switch s, i.e.,

$$\begin{aligned} \hat{\tau}_1 &= 0, \\ \hat{\tau}_2 &= \hat{\tau}_s. \end{aligned} \tag{11.10}$$

Then, one has

$$\frac{1}{T_1}(V_s\hat{\tau}_1 - V_{\bar{s}}\hat{\tau}_2) = \frac{V_{\bar{s}}}{D}(-\hat{d}') = V_{off}\hat{d}, \tag{11.11}$$

and

$$\frac{1}{T_2}(I_{\bar{s}}\hat{\tau}_1 - I_s\hat{\tau}_2) = \frac{I_s}{D'}(-\hat{d}') = \frac{I_{on} D}{D'}\hat{d}. \tag{11.12}$$

Constant-Off-Time Control

Under this control strategy, the off-time of the active switch s is kept constant, and regulation is realized by variations of the switching period (variable frequency). The control is described by

$$\begin{aligned} \hat{\tau}_1 &= \hat{\tau}_s, \\ \hat{\tau}_2 &= 0. \end{aligned} \tag{11.13}$$

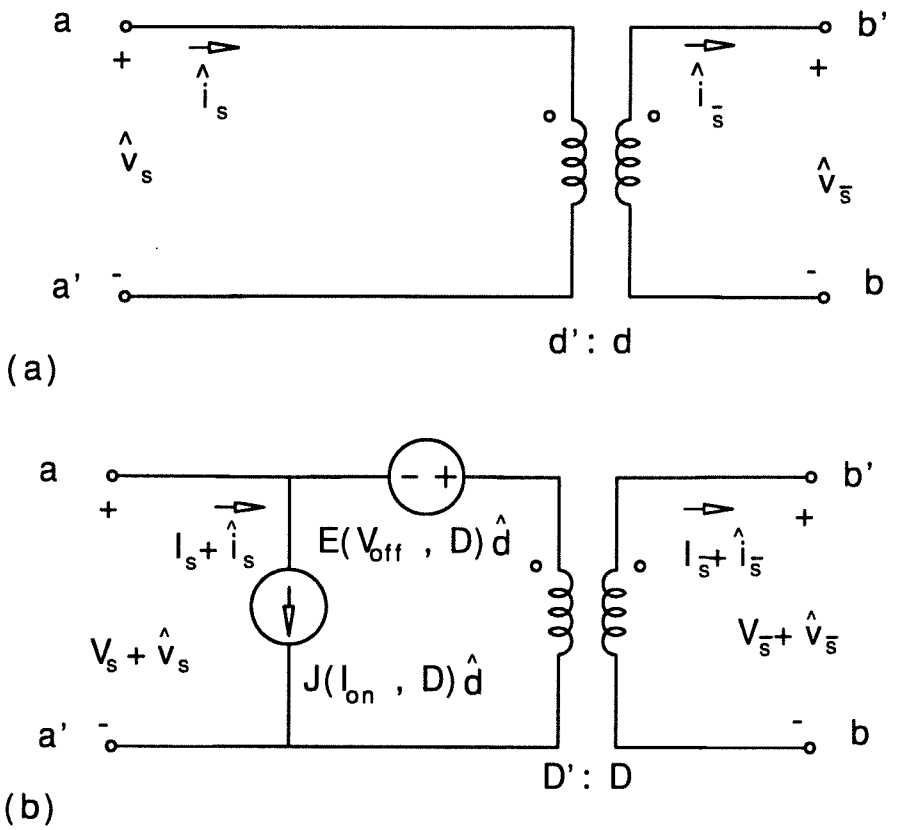

Figure 11.2: The large- and small-signal versions, (a) and (b), of a reduced form of the generic averaged model for two switches for three common control strategies. They are representative of all three cases, and hence it can be used interchangeably with the generic model.

One then has

$$\frac{1}{T_1}(V_s\hat{\tau}_1 - V_{\bar{s}}\hat{\tau}_2) = \frac{V_s}{D}(\hat{d}) = \frac{V_{off}D'}{D}\hat{d}, \tag{11.14}$$

and

$$\frac{1}{T_2}(I_{\bar{s}}\hat{\tau}_1 - I_s\hat{\tau}_2) = \frac{I_{\bar{s}}}{D'}(\hat{d}) = I_{on}\hat{d}. \tag{11.15}$$

Table 11.1 collects respective expressions for the voltage source and the current sources for the three control strategies. Note that expressions for the sources for constant on-time and constant off-time controls have been written in terms of the perturbation of duty ratio $\hat{d}$. Differences in control strategies are represented by different values for the sources. The fact that two variable-frequency controls can be rendered into equivalent constant-frequency control indicates that understanding of constant-frequency control (PWM) is fundamental, and is representative of all three control strategies. Hence, without loss of generality, discussions and extensions on the generic model can be focused on the reduced form for converters with constant-frequency control (PWM converters). Furthermore, since the three control strategies cover practically all potential control strategies, the reduced form for constant-frequency control in Fig. 11.2 is used interchangeably with the generic model in Fig. 11.1.

11.3 Relationships Among Different Models

In this section, relationships among the generic model, the model of PWM switches [34], and the canonical circuit models [12] for converters are discussed.

It is shown that the model of PWM switches is a special case of the generic model. Both the model of PWM switches and the generic model are equivalent to the canonical circuit model (for converters) if they are applied to a specific converter.

The relationships are revealed with the aid of circuit transformation techniques. One of them, which is particularly useful, is the shifting of sources [24, 25].

Another one is the reflection of impedances and sources from the primary to the secondary, and vice versa. Actually, the fact that the generic model is in an equivalent transformer form is one advantage over previous models, which, in addition to

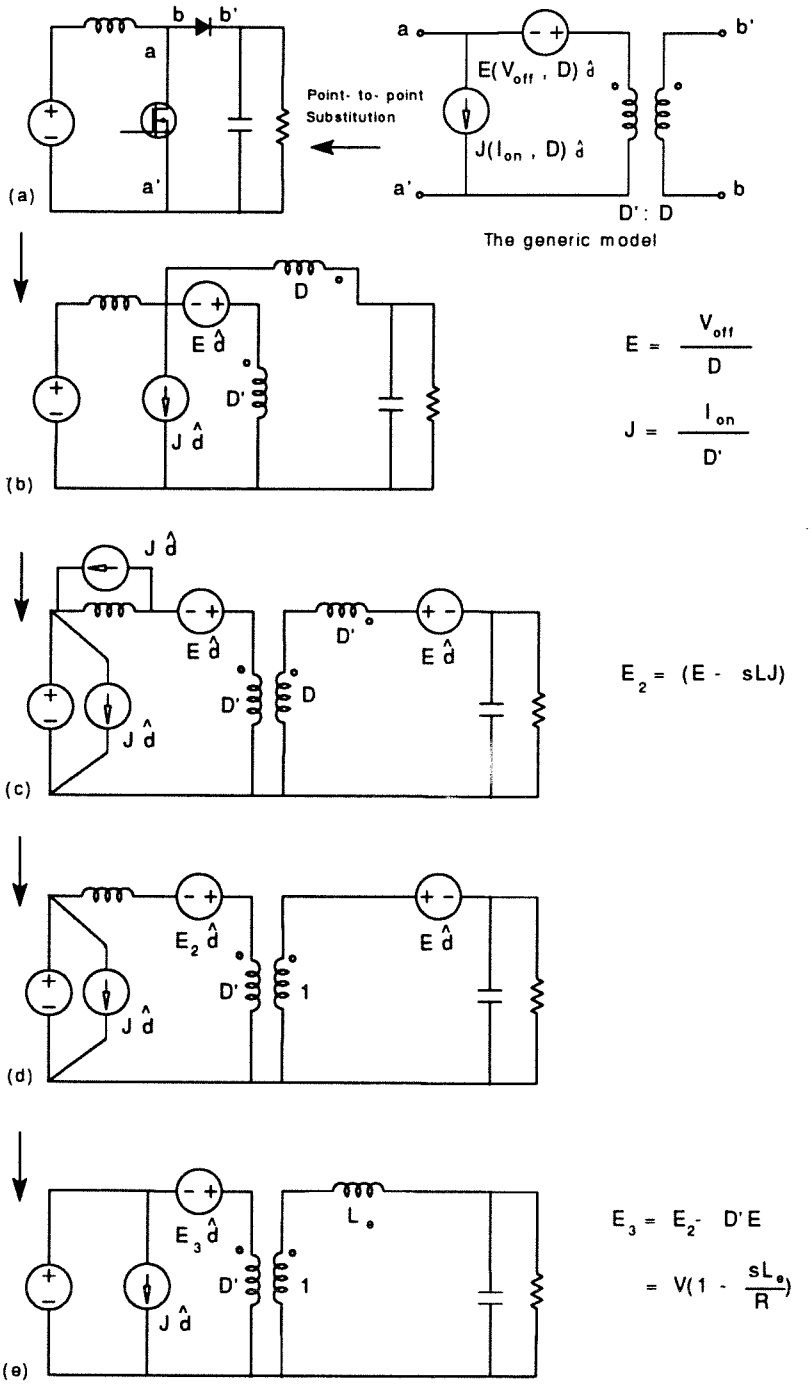

Figure 11.3: Key steps of circuit transformation. Substitution of the generic model into a boost converter (a) leads to an equivalent circuit (b); shifting $J\hat{d}$ and the combination of $E\hat{d}$ and D' "turns ratio" gives (c); absorbing one of the current source leads to (d); reflecting $E\hat{d}$ to the "primary" and L to the "secondary" yields (e), which is found to be identical to the canonical model.

other circuit manipulation techniques, allows application of the technique of impedance reflection.

Relationship with the Canonical Model

Figure 11.3 (a) shows a boost converter and the generic small-signal model. Simple point-to-point substitution of the model into the converter to replace switches one at a time leads to the equivalent circuit in Fig. 11.3 (b).

Shifting the current source $J\hat{d}$, the combination of $E\hat{d}$, and the part of transformer with D' "turns," one obtains the equivalent circuit shown in Fig. 11.3 (c).

Absorbing the current source in parallel with the inductance and the secondary two turns ratios into one ($D + D' = 1$), one arrives at the equivalent circuit shown in Fig. 11.3 (d).

Reflecting the voltage source in the secondary to the primary and the inductance from the primary to the secondary, one derives the equivalent circuit in Fig. 11.3 (e), where

$$J = \frac{I_{on}}{D'} = \frac{I_g}{D'} = \frac{V}{D'^2 R}, \tag{11.16}$$

$$E_3 = E_2 - D'E = E - sLJ - D'E = V(1 - \frac{sL_e}{R}), \tag{11.17}$$

$$L_e = \frac{L}{D'^2}. \tag{11.18}$$

Comparing Fig. 11.3 (e) with Fig. 11 and Table 1 in [12], one can see that circuit topologies and expressions on both circuits are identical. Hence, it is verified that the generic model is identical to the canonical model when it is applied to a particular converter.

Relationship with the Model of PWM Switches

The relationship between the generic model and the model for PWM switches is revealed in Fig. 11.4.

Start with the generic model. Connect b' to a' to form a three terminal device as shown in Fig. 11.4 (a), which is also called "the common passive connection."

Shift the current source as shown in Fig. 11.4 (b).

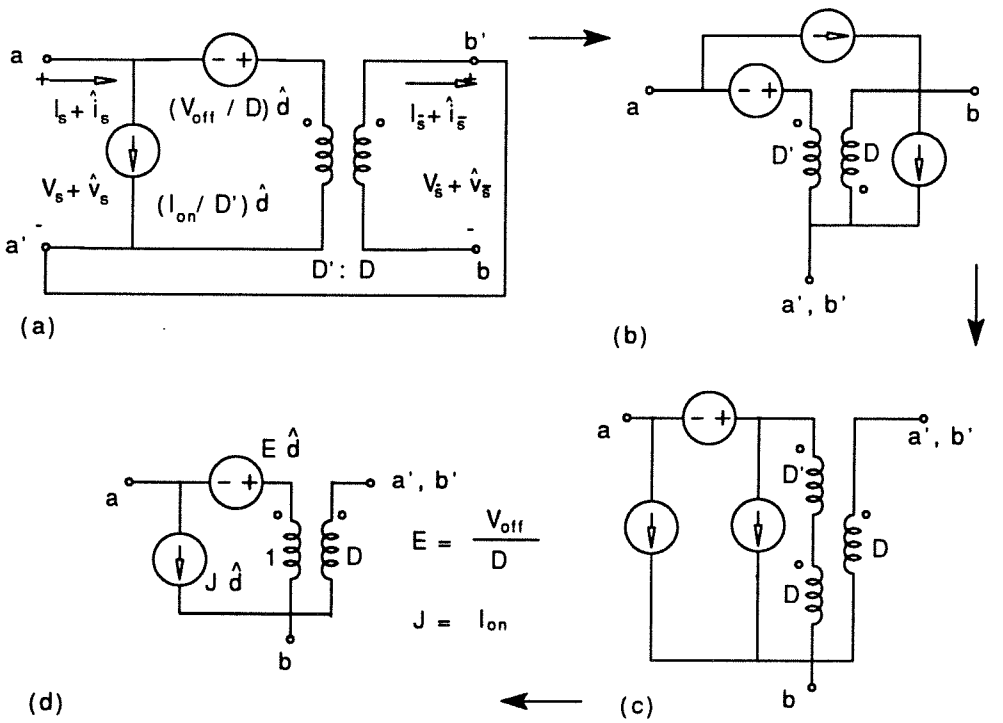

Figure 11.4: Key steps of circuit transformation: Connect b' to a' in the generic model (a) to from a three-terminal circuit (b); shifting the secondary to the primary and reflecting the current source to the overall winding with $D + D'$ turns lead to (c); Combine the current sources to obtain (d).

Shifting the secondary to the primary, and then reflecting the current source to the overall winding with "turns" $D + D' = 1$, one obtains the equivalent circuit Fig. 11.4 (c).

Combining two current sources, one obtains the equivalent circuit as shown in Fig. 11.4 (d), where the voltage and current sources are given by

$$E = \frac{V_{off}}{D} \tag{11.19}$$

$$J = \frac{I_{on}}{D'} - \frac{I_{on} D}{D'} = I_{on}. \tag{11.20}$$

Comparing Fig. 11.4 with Fig. 7 in [34], one can see that these two equivalent circuits are identical. Note that in [34] terminals a, $a'b'$, and b were named a, c, and p,

respectively, and v_{off} is denoted as v_{ap} and i_{on} as i_c. Hence, one can see that the model for PWM switches is a special case of the generic model.

Note that connecting a' to b' forms a so-called "common-passive" case. It can be shown that other connections are also special cases of the generic model.

In short, one may say that the generic model inherits advantages of previous models and extends those efforts to a new height: modeling switches as two-terminal linear-time-invariant circuit elements for their low-frequency characterizations. A long journey for the power electronics community to find a simple way to model switches is now successfully completed.

Chapter 12

Extension to Switches in Isolated Converters

The generic model has been limited so far to converters without isolation transformers. This constraint is relaxed in this chapter.

In most applications of switching power conversions, transformers are required to isolate the secondary from the primary. In addition, the presence of a transformer provides an additional avenue for obtaining large values of voltage conversion ratio. Hence, the generic model needs to be extended to cover converters with isolation transformers (isolated converters).

Isolated converters discussed here can in general be classified into two groups: 1) converters derived from basic converters such as, for example, the forward converter, the flyback converter, the isolated Ćuk converter, and the isolated Sepic converter; and 2) converters with parallel power paths developed primarily for high-power applications such as, for example, the push-pull, the half-bridge, and the full-bridge converters. The generic model will be extended to cover converters in both groups.

12.1 Basic Isolated Converters

One particular feature associated with isolated converters is the fact that they frequently use more than two switches. Additional switching devices are needed either to allow insertion of an isolation transformer, or to provide an additional parallel path to handle more power with similar device ratings.

A general rule for inserting an isolation transformer into a converter is that any alterations of the converter circuit do not change the dc and the ac circuits, except a scaling factor (turns ratio) associated with voltages and currents.

Figure 12.1 shows four basic isolated converters in the first group which are frequently

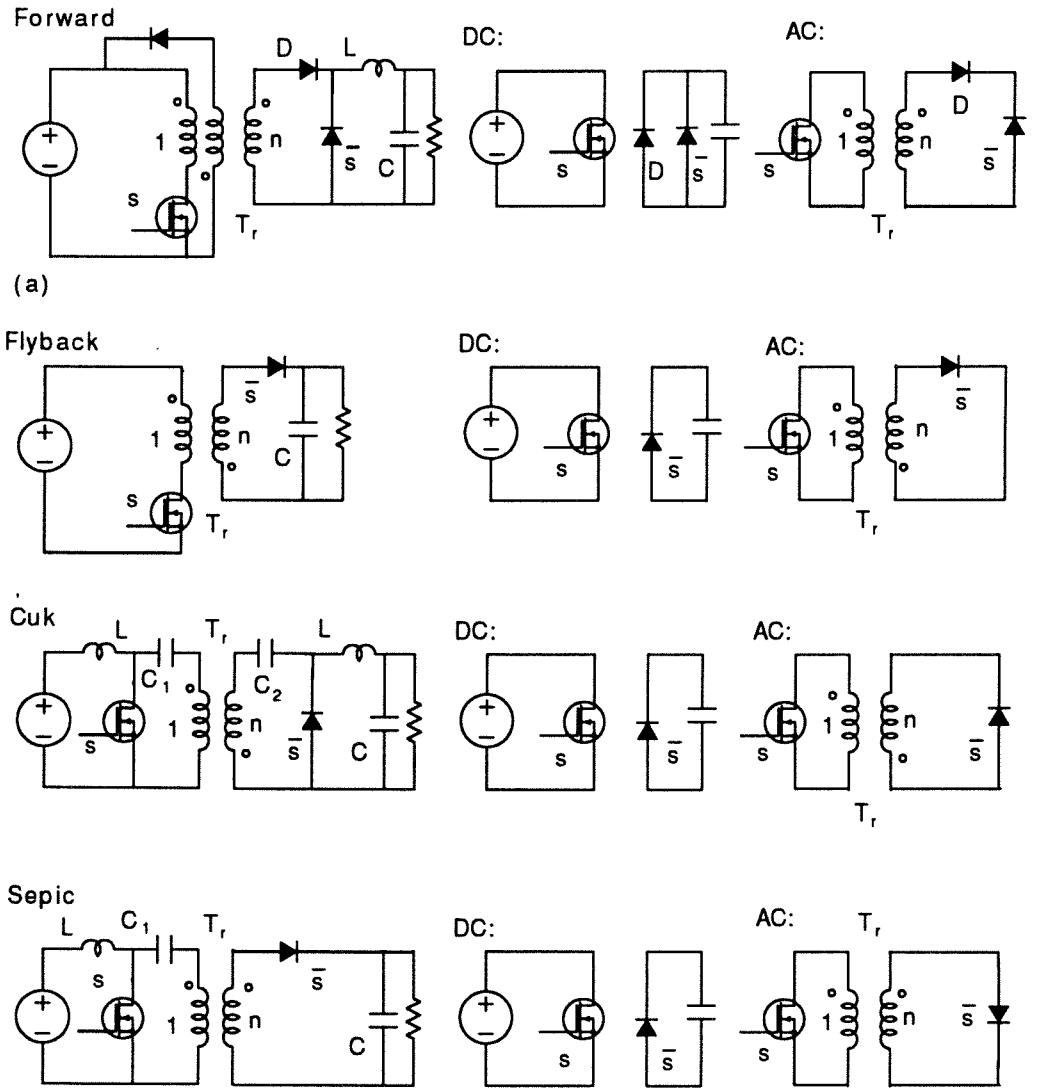

Figure 12.1: Isolated converters and their dc and ac circuits: the forward, the flyback, the isolated Ćuk, and the isolated Sepic converter cases.

encountered in practical designs. The corresponding dc and ac equivalent circuits are drawn next to them.

The forward converter in Fig 12.1 (a) is derived from the buck converter by inserting an isolation transformer T_r. The transformer is inserted by first splitting the switch into two (with identical duty ratios) and then connecting a transformer in between.

When switch s (the transistor) is on, the positive value of the voltage over diode D forces itself to turn on, hence the power is pumped through the transformer to the output. In the meantime, a certain amount of energy is stored in the transformer magnetic field. Diode D is necessary to provide a forward path for power to flow from the primary to the secondary, and then the output.

When switch s is off, diode D is off, and switch $\bar{s}$ is on. Power is supplied to the output through the freewheeling of the inductor current which is sustained by the energy stored in the magnetic field of the inductor. In the meantime, the energy associated with the transformer is fed back to the input voltage source through D_r, hence resetting the magnetic field, which prevents the onset of saturation of the magnetic core.

The flyback converter shown in Fig. 12.1 (b) is obtained by introduction of an isolation transformer into the buck/boost converter. Since the location of the inductor is at a place where the converter can be disconnected electrically by insertion of a transformer, no additional switching devices are needed.

When switch s (the transistor) is on, switch $\bar{s}$ (the diode) is off. Power is pumped into the transformer, and the output capacitor discharges its voltage, supplying power to the load. When switch s is off, switch $\bar{s}$ is on, providing power to the output and, in the meantime, re-supplying power to the capacitor (by charging-up of the capacitor voltage). It is seen that the isolation transformer acts similar to a two-winding inductor, and hence no additional switching devices are needed.

The isolated Ćuk converter shown in Fig. 12.1 (c) is realized by splitting the energy transfer capacitor into two and then inserting a true ac transformer in between. An ac transformer can be used since there is no dc current flowing through the capacitor. No additional switches are needed to maintain the same dc and ac circuits.

The isolated Sepic converter is shown in Fig. 12.1 (d). An isolation transformer can

be inserted in the way as in a flyback converter, since the location of the inductor provides a natural place for insertion of a transformer. No additional switches are needed.

Figure 12.2 shows isolated converters in the second group which have parallel power paths. Within one switching cycle, the parallel paths provides two pulses. The ripple frequency seen by the low-pass filter, formed by L and C, is twice of the switching frequency.

The complementary switch $\bar{s}$ is implicitly present. Its function for freewheeling of inductor current is actually undertaken by diode D_1 and D_2. This implicit freewheeling can be brought out to the surface by insertion of a catch diode across the input terminals of the low-pass filter.

Several features of these converters are transparent in the dc circuits. The output of the dc circuits for the push-pull, the half-bridge, and the full-bridge are identical. For the same device ratings for diodes, they can handle twice the power than a forward converter can, since the two diodes are in parallel in dc circuits.

At the input side, the maximum value of reverse voltage for a transistor is twice as high as the input source voltage for the push-pull, and it is the same value as the input voltage source in the half- and full-bridge converters. For the same current rating for transistors, the push-pull can sink twice the dc power from the input source as that of a half-bridge. The full-bridge converter can sink the same dc current as the push-pull, but with half the value of maximum reverse voltage as in a push-pull converter.

The striking feature of ac circuits is that they all have the same form, which says that small-signal dynamics of these converters are identical. Indeed, the ac circuits are equivalent to that for the forward converter. This can best be seen by inserting a catch diode D_c in the secondary, as shown in Fig. 12.3. Insertion of the catch diode brings out the freewheeling function to the surface, but it does not change the qualitative operation of these converters. The small-signal low-frequency dynamics will not be altered since the current waveform presented to the low-pass filter remains the same.

Figure 12.3 (a) shows the insertion of the catch diode D_c, which is equivalent, in one switching cycle, to the sum of Fig. 12.3 (b) and (c). Without loss of generality, take $n = 1$. Then, Fig. 12.3 (d) is derived, which shows equivalent circuits for two pulses, respectively.

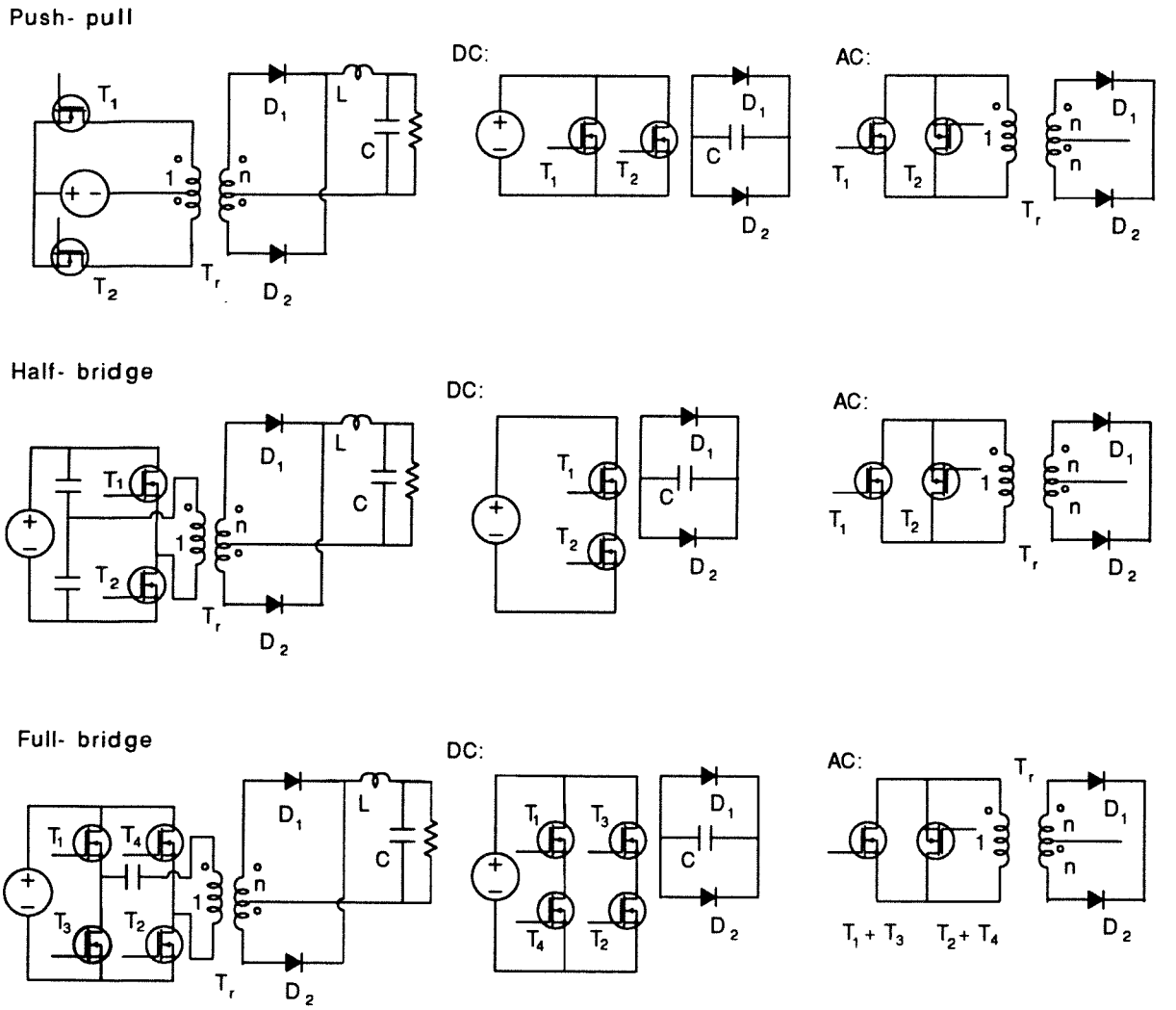

Figure 12.2: Isolated converters and their dc and ac circuits: the push-pull, the half-bridge, and the full-bridge cases.

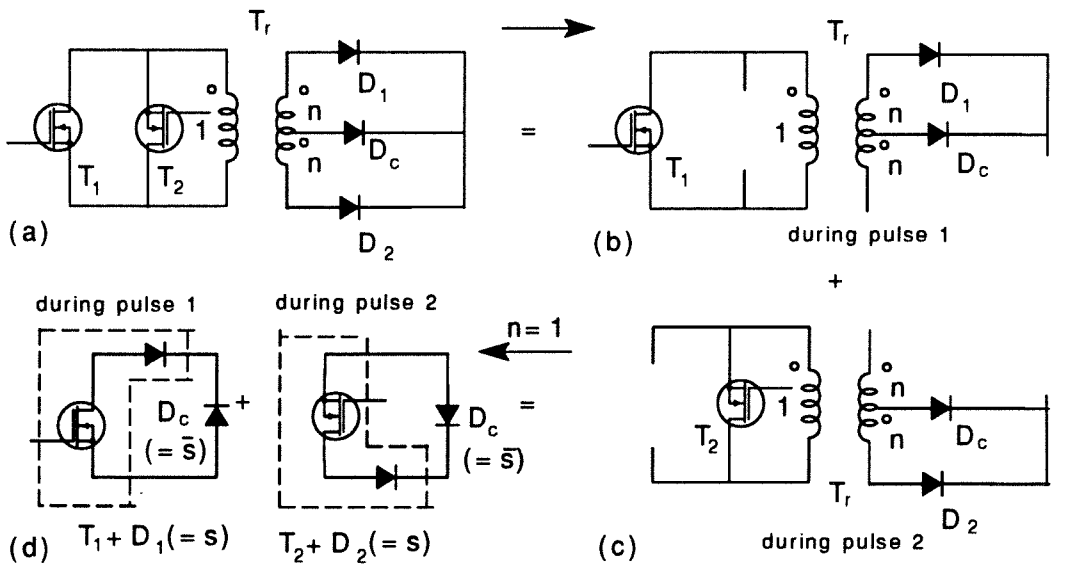

Figure 12.3: Insertion of a catch diode reveals that the push-pull, the half-bridge, and the full-bridge converters have the same ac circuit as that for the forward converter, except that there are two identical ac equivalent circuits within one switching cycle.

For each pulse-time duration, the combination of the transistor and the diode behave just as a single switch (switch s), and the catch diode is the complementary switch (switch $\bar{s}$).

Therefore, the ac circuit for converters with parallel paths is equivalent to that for the forward converter, except that there are effectively two identical ac equivalent circuits within one switching cycle.

Finally, the above approach handles converters in the second group of isolated converters (with multiple switches) in the framework of converters with two switches. The advantage of doing so is that knowledge about two-switch converters is sufficient to characterize isolated converters in the second group.

Another approach is to handle converters with multiple switches in the framework of multiple switches. The potential advantage would be to obtain a model for four (or six) switches, instead of for two switches. Characterization of a three-switch converter in

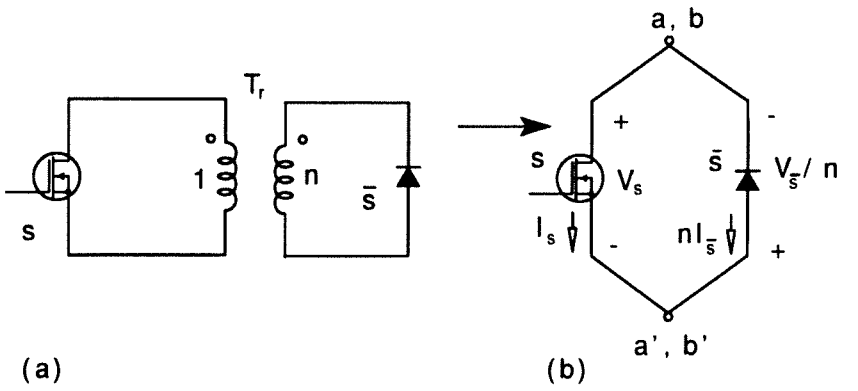

Figure 12.4: The general ac equivalent circuit for isolated converters (a); and its generalized ac equivalent circuit after the transformer T_r is absorbed (b).

Chapter 15 shows key steps of modeling in the general framework of multiple switches. The approach can be followed to handle converters with more than three switches, which remains to be done in the near future.

12.2 The Balance Equation and the Extended Generic Model

Figure 12.4 (a) shows the equivalent ac circuit for converters with isolation transformers, where n is the turns ratio defined as number of turns for the secondary of the isolation transformer N_2 over the number of turns for the primary N_1, i.e., $n \equiv N_2/N_1$. Voltage $V_{\bar{s}}$ and current $I_{\bar{s}}$ can be reflected from the secondary to the primary by conventional techniques for a two-winding transformer. Fig. 12.4 (b) shows the ac circuit with the transformer absorbed.

According to the ac circuit, the balance equation can be written as

$$\begin{cases} V_s T_1 = \dfrac{V_{\bar{s}}}{n} T_2 \\ n I_{\bar{s}} T_1 = I_s T_2. \end{cases} \tag{12.1}$$

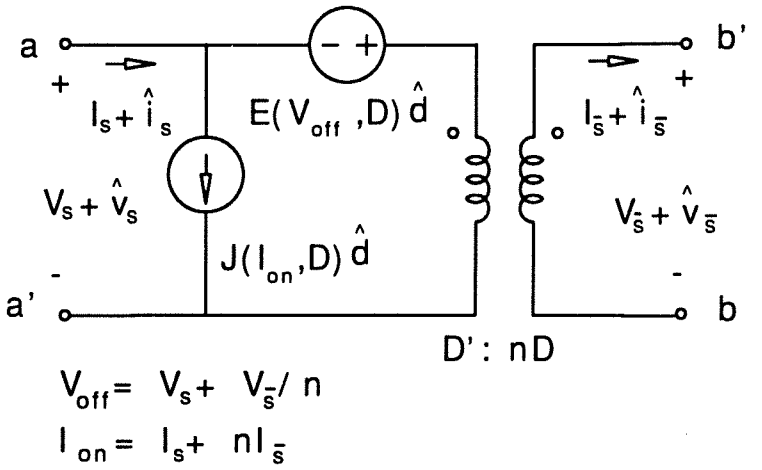

Figure 12.5: The extended generic model for switches in isolated converters, where the physical transformer T_r (turns ratio $1 : n$) has been combined with the conceptual transformer (turns ratio $D' : D$) to form a hybrid transformer with a turns ratio $D' : nD$.

Perturbation in turn leads to

$$\begin{cases} \hat{v}_s = -\dfrac{V_s}{T_1}\hat{\tau}_1 + \dfrac{T_2}{nT_1}\hat{v}_{\bar{s}} + \dfrac{V_{\bar{s}}}{nT_1}\hat{\tau}_2 \\ \\ \hat{i}_{\bar{s}} = -\dfrac{I_{\bar{s}}}{T_1}\hat{\tau}_1 + \dfrac{T_2}{nT_1}\hat{i}_s + \dfrac{I_s}{nT_1}\hat{\tau}_2. \end{cases} \tag{12.2}$$

Equation (12.2) can be rendered into a reduced form by introduction of the control constraint for constant-frequency control (PWM),

$$\hat{\tau}_2 = -\hat{\tau}_1 = -\hat{d}. \tag{12.3}$$

Then, Eq. (12.2) is reduced to

$$\begin{cases} \hat{v}_s = -\dfrac{1}{T_1}\left(V_s + \dfrac{V_{\bar{s}}}{n}\right)\hat{d} + \dfrac{T_2}{nT_1}\hat{v}_{\bar{s}} \\ \\ \hat{i}_{\bar{s}} = -\dfrac{1}{T_1}\left(I_{\bar{s}} + \dfrac{I_s}{n}\right)\hat{d} + \dfrac{T_2}{nT_1}\hat{i}_s. \end{cases} \tag{12.4}$$

Figure 12.5 shows the extended generic model derived from the above equations where

$$V_{off} \equiv V_s + \frac{V_{\bar{s}}}{n}, \tag{12.5}$$

$$I_{on} \equiv I_s + nI_{\bar{s}}. \tag{12.6}$$

The extended generic model for switches in isolated converter is the same as the generic model except that quantities associated with the secondary are scaled by the turns ratio. That is, voltages, $V_{\bar{s}}$ and $\hat{v}_{\bar{s}}$, are divided and currents, $I_{\bar{s}}$ and $\hat{i}_{\bar{s}}$, are multiplied by n. This reflects the effect of a transformer since insertion of transformer is to provide isolation and voltage scaling.

Note that the extended generic model combines the physical transformer T_r (turns ratio $1 : n$) with the conceptual transformer (turns ratio $D' : D$) to form a hybrid transformer with a turns ratio $D' : nD$. The physical transformer represents the magnetic coupling between the primary and the secondary, whereas the conceptual transformer represents "time coupling" between the "primary" and the "secondary." The time coupling between two switch branches in a converter is the result of the inherent switching action in a switching converter.

Application of the extended generic model is straightforward. First, put a conceptual transformer at the very front of the converter under discussion, which reduces the converter into a one with $1 : 1$ turns ratio, eliminating effectively the transformer. Second, substitute the extended generic model into the scaled circuit in the same way as for a non-isolated converter. And third, scale back the whole primary of the transformer, which is automatically restored into the circuit by the substitution because of the way the extended generic model is formulated.

12.3 The Effect of Leakage and Magnetizing Inductances

So far the discussion about switches in isolated converters has been limited to converters with ideal transformers. In practice, transformers are not ideal. Among the non-idealities, the leakage inductance and the magnetizing inductance are more important since they can change the small-signal dynamics of a converter drastically if no control is exercised on them.

Figure 12.6 (a) shows that ac circuit in converters with non-ideal transformers, where L_l is the leakage inductance and L_m is the magnetizing inductance. The leakage inductance in the secondary is assumed to be negligible for simplicity.

Figure 12.6 (b) is the general form of the ac circuit derived by scaling switch $\bar{s}$ to the

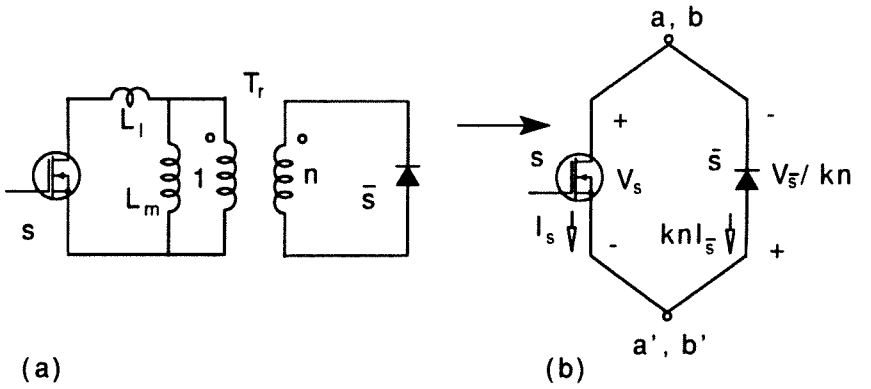

Figure 12.6: The general ac equivalent circuit for converters with non-ideal isolation transformers (a); and its generalized ac equivalent circuit after the transformer T_r, L_l, and L_m are absorbed (b).

primary. The leakage and the magnetizing inductances form an inductance divider with a ratio $k \equiv \frac{L_m}{L_l+L_m}$, which is frequently called the coupling coefficient of the transformer.

It is straightforward to see that the scaled value of the voltage across switch $\bar{s}$ is given by $V_{\bar{s}}/kn$. The scaled value of the current is obtained as $knI_{\bar{s}}$.

From the general form of the ac circuit in Fig. 12.6 (b), one can write the corresponding balance equation as

$$\begin{cases} V_s T_1 = \dfrac{V_{\bar{s}}}{kn} T_2 \\ knI_{\bar{s}} T_1 = I_s T_2. \end{cases} \tag{12.7}$$

Equation (12.7) suggests that it can also be obtained mathematically by replacement of n in Eq. (12.1) with kn. Hence, one can see that the extended generic model will be the same as that in Fig. 12.5, except the replacements of n with kn.

Therefore, one can obtain the model for switches in converters with non-ideal transformers as shown in Fig. 12.7, where

$$V_{off} \equiv V_s + \frac{V_{\bar{s}}}{kn}, \tag{12.8}$$

$$I_{on} \equiv I_s + knI_{\bar{s}}. \tag{12.9}$$

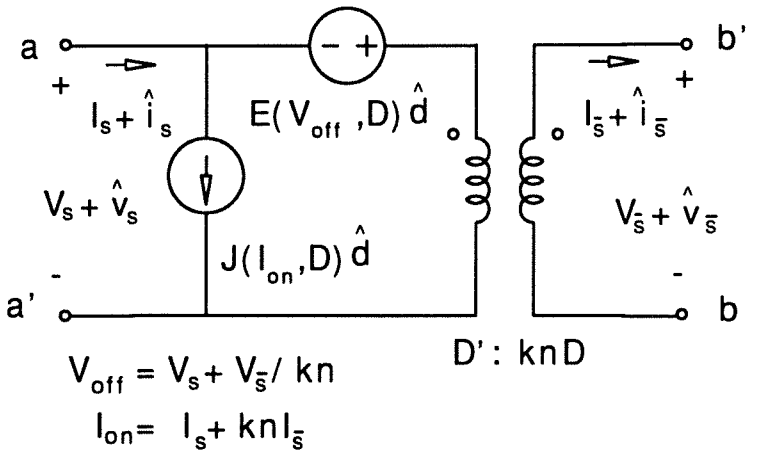

Figure 12.7: The extended generic model for switches in converters with non-ideal transformers, where the physical transformer T_r (turns ratio 1 : kn) has been combined with the conceptual transformer (turns ratio D' : D) to form a hybrid transformer with a turns ratio $D' : knD$.

One can now see that the impedance divider does introduce an additional scaling effect in the extended generic model. As expected, the scaling effect represents additional attenuation in the forward path of the power flow.

Consequently, one cannot simply add L_l and L_m into the model in Fig. 12.5 to obtain the model in Fig. 12.7, since both the "turns ratio" and small-signal sources in the model are changed when L_l and L_m are added.

The effect that L_l and L_m have on the small-signal dynamics of a converter can be best seen by derivation of the canonical model from the extended generic model.

In Fig. 12.8, key steps of deriving the canonical model for a forward converter are illustrated.

Figure 12.8 (a) is the equivalent circuit after the transformer is scaled to be a 1 : 1.

Figure 12.8 (b) is the equivalent circuit when the the 1 : 1 transformer is absorbed. The forward diode D is replaced by a wire since it is in synchronization with switch s, and it does not introduce additional dynamics into the circuit.

Figure 12.8 (c) is the circuit after point-by-point substitution of switches with the generic model.

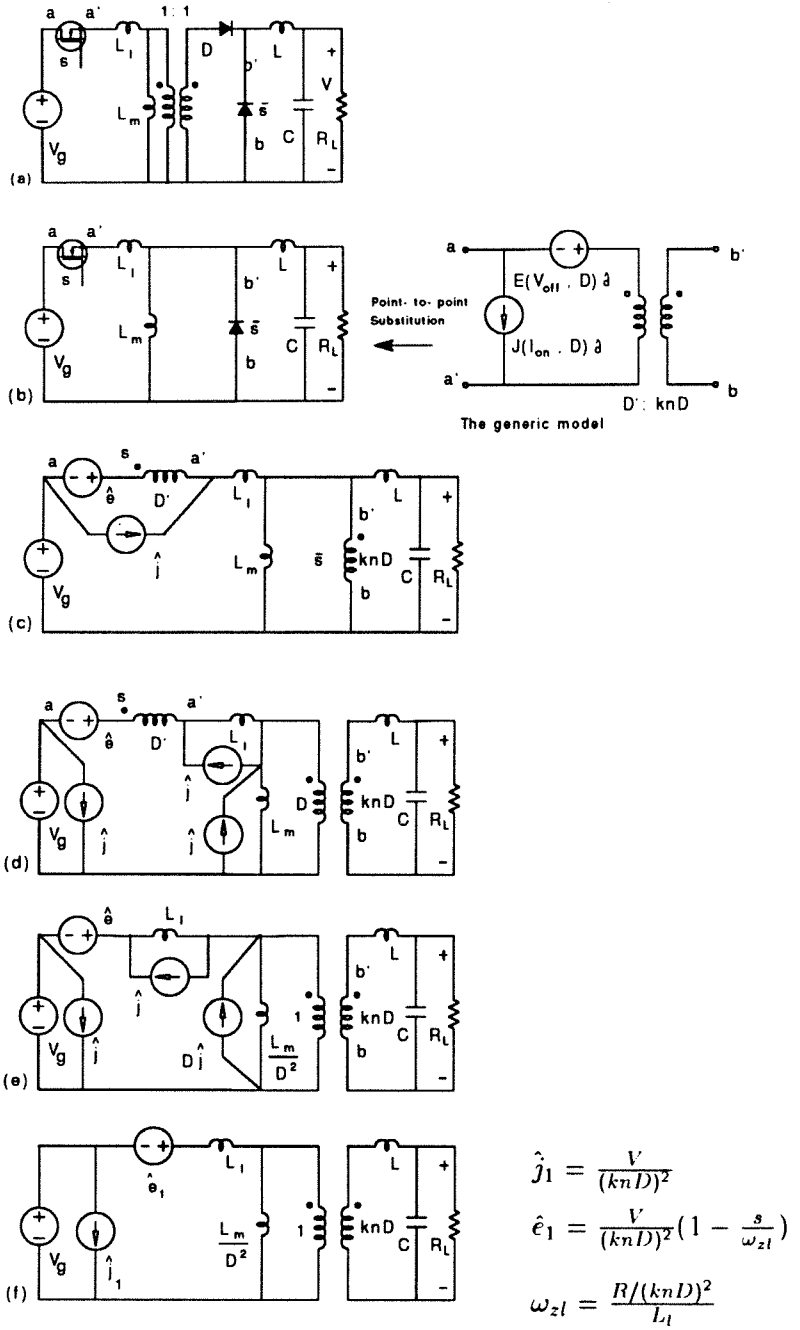

Figure 12.8: Key steps in derivation of a canonical model for the forward converter with a non-ideal isolation transformer: scaling the transformer (a); removing the transformer and the forward diode D (b); substitution of the generic model for switches (c); shifting the current source and introducing an equivalent transformer with turns ratio D : knD (d); combining two transformer turns ratios in the primary and scaling the current source and the magnetizing inductance into the side with turns ratio 1 (e); and turning the parallel connection of L_l and $\hat{j}$ into a series connection leads to the final form (f).

Shifting the current source $\hat{j}$, and splitting the the secondary with knD turns into an equivalent transformer, one obtains the equivalent circuit in Fig. 12.8 (d).

Putting the primary with D' turns together with the one with D turns, and then reflecting L_m and the current source in parallel with it to the side with turns $D + D' \equiv 1$, one derives the equivalent circuit shown in Fig. 12.8 (e).

Turning the parallel connection of L_l and $\hat{j}$ into a series connection, one has the final form in Fig. 12.8 (f), which is the desired canonical model for the forward converter with non-ideal transformer. The voltage source and the current source are found to be

$$\hat{j}_1 = (1-D)\hat{j} = I_{on} = \frac{knV}{R} \tag{12.10}$$

$$\hat{e}_1 = \hat{e} - \hat{j}(1-D)sL_l = \frac{V}{(knD)^2}\left(1 - \frac{s}{\omega_{zl}}\right), \tag{12.11}$$

where the RHP zero ω_{zl} is given by

$$\omega_{zl} = \frac{R/(knD)^2}{L_l}. \tag{12.12}$$

Several remarks are in order here.

One RHP zero ω_{zl} is introduced by the leakage inductance L_l, which represents a departure from the small-signal dynamics of a forward converter with an ideal transformer (which is basically the same as the buck converter). The introduction of ω_{zl} is not a real surprise since the physical position of L_l, with respect to that of switch s, is the same as that of the inductor in the boost converter which has a RHP zero.

The value of ω_{zl} is proportional to the dc operating point resistance R scaled by the turns ratio $1 : knD$ of the hybrid transformer, and is inversely proportional to L_l. For the forward converter, knD is less than unity, and L_l is frequently very small. Hence, ω_{zl} is frequently located at very high frequency. Its effect (phase lag) may not necessarily be seen if the measurement is not performed into high frequencies.

However, for converters with coupled inductors, the leakage inductance may not be small. Hence, the effect of ω_{zl} is more visible.

Note that the presence of L_l and L_m also introduce additional poles into the frequency response of the converter. Derivation of the poles are straightforward, and hence is not pursued here.

Finally, it is reiterated that the presence of the leakage inductance and the magnetizing inductance alters the small-signal dynamics of a forward converter qualitatively. In addition to the additional attenuation of the inductance divider, the leakage inductance brings a right-half-plane zero into the canonical model, experimental verification of which remains to be done.

Chapter 13

Extension to Switches in Discontinuous Conduction Modes

Switching converters operate sometimes in discontinuous modes. Discontinuous conduction modes normally include discontinuous inductor current mode and discontinuous capacitor voltage mode. Major benefits of discontinuous operation are reduced sizes for inductor or/and capacitor, improved small-signal dynamics, and the ability for input current to follow, to a variable degree, the shape of input voltage automatically.

In discontinuous conduction modes, the dc value of inductor current is no longer determined by the duty ratio alone. Additional work is needed to extend the generic model to cover switches in converters in discontinuous modes. A key step in extending the generic model to cover switches in discontinuous modes is the establishment of the concept of equivalent duty ratio δ, which was originally proposed in [15, 14] (the symbol used there was m) for modeling converters. A discussion about the theoretical aspect of the concept is presented for the first time, which reveals that the concept of equivalent duty ratio is useful in determining low-frequency small-signal dynamics for switches as long as the dc component of transistor current (or diode voltage) is not vanishingly small.

The end result of the extension is that the sources associated with duty ratio $\hat{d}$ in the generic model are replaced by the equivalent duty ratio $\hat{\delta}$, which is a function of system states. That is, feedbacks are identified by the introduction of the equivalent duty ratio to account for the effect of discontinuous inductor current (or discontinuous capacitor voltage).

The extended generic model also shows that the quadratic double pole in various transfer functions for discontinuous conduction mode can normally be separated into two real poles. An expression for the high-frequency pole is derived.

Since the discontinuous capacitor voltage mode is the dual mode of operation, results about discontinuous inductor current can be converted into corresponding forms easily for discontinuous capacitor voltage mode by use of the principle of duality [14]. Consequently, the following discussion focuses on the discontinuous inductor current mode.

13.1 Equivalent Duty Ratio δ

For converters operating in discontinuous inductor current mode, the generic model cannot be used directly since the small-ripple constraint is violated.

When the ripple is not small, v_{off} and i_{on} are no longer pure dc quantities. Instead, they have large ripples. The waveforms of switch current and voltage are no longer square waveforms. As shown previously, in the decomposition of the waveforms, a key step in modeling switches, the dc components are expressed as linear functions of V_{off}, I_{on}, and the duty ratio D. Referring to Fig. 11.1, one can find that, with the small-ripple constraint,

$$\bar{i}_t = DI_{on}, \tag{13.1}$$

$$\bar{v}_d = DV_{off}. \tag{13.2}$$

For switches with large ripples, it is no longer possible to express the average inductor current as a linear function of duty ratio, because the sharp edges associated with square waves are no longer present. The disappearance of the sharp edge(s) obscures the definition for the duty ratio (see Fig. 13.1).

This difficulty can be overcome by extending the method of state-space averaging. According to linear circuit theory (see, for example, [24]), two converters will have the same dc conversion ratio if both converters have the same dc components for their transistor currents and diode voltages, regardless what waveforms the voltages and currents may have.

Mathematically, the equivalent duty ratio can be defined as

$$\delta = \frac{\bar{i}_t}{I_{on}} = \frac{\bar{v}_d}{V_{off}}, \tag{13.3}$$

where the bar indicates the average value for the corresponding quantity (The equivalence of the two definitions can be established in a straightforward manner. See, for example,

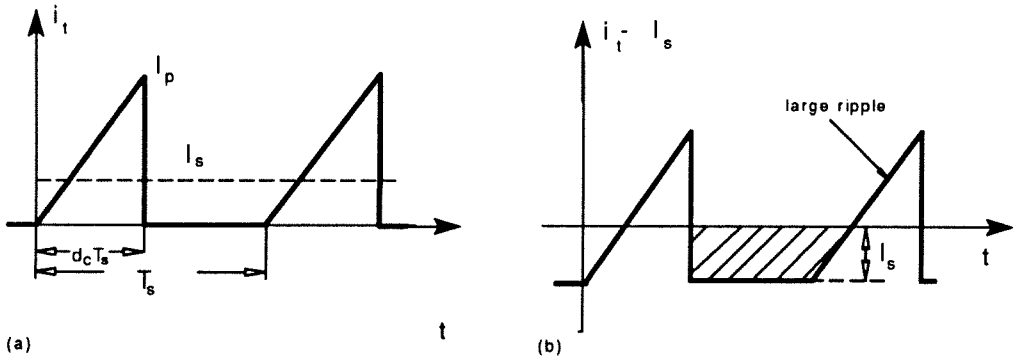

Figure 13.1: Waveform of inductor current in discontinuous mode, showing that the dc component of inductor current cannot be expressed as a linear function of duty ratio D.

[14]). Note that the equivalent duty ratio was originally denoted as m. A different symbol δ is used in the present work to avoid possible confusion of m with the voltage conversion ratio M for the cases where capitalizations are required.

The above definition suggests that as far as dc behavior is concerned, two converters are equivalent if both have the same dc values for switch currents and voltages. Of course, for a switch with large ripples associated with its current and/or voltage, the dc component is no longer uniquely controlled by the duty ratio. It is also related to those circuit parameters which determine modes of converter operation. Since the PWM tree switching structure is still existent for any converters with large ripples, one can see that in general, the transistor current i_t (or the diode voltage v_t) is a function of voltage v_{off}, current i_{on}, and independent control τ_c (note that τ_c may represent multiple controls).

An immediate question that one may ask is: Whether or not does the equivalent duty ratio δ retain the same information about low-frequency small-signal dynamics?

This issue can be addressed by looking into the Fourier expansion of the transistor current i_t (or v_d).

According to Fourier theory, for a periodic waveform such as i_t, the following expan-

sion can be written as

$$i_t = \bar{i}_t + \sum_{n=1}^{\infty} c_n \cos(n\omega_s t - \theta_n), \tag{13.4}$$

where

$$c_n = \sqrt{a_n^2 + b_n^2}, \tag{13.5}$$

$$\theta_n = tan^{-1}\left(\frac{b_n}{a_n}\right), \tag{13.6}$$

$$\bar{i}_t = \frac{1}{T_s}\int_t^{t+T_s} i_t\, dt, \tag{13.7}$$

$$a_n = \frac{2}{T_s}\int_t^{t+T_s} i_t \cos n\omega_s t\, dt, \qquad n = 1, 2, \cdots \tag{13.8}$$

$$b_n = \frac{2}{T_s}\int_t^{t+T_s} i_t \sin n\omega_s t\, dt, \qquad n = 1, 2, \cdots. \tag{13.9}$$

The Dirichlet conditions for Fourier expansion to exist (see, for example, [42]) accommodate virtually all cases arising in the the field of power electronics.

When a small-signal sinusoidal perturbation is introduced, the expansion can in general be written as

$$(i_t + \hat{i}_t) = (\bar{i}_t + \hat{\bar{i}}) + \sum_{n=1}^{\infty} (c_n + \hat{c}_n)\cos[n(\omega_s + \hat{\omega}_s)t - \theta_n], \tag{13.10}$$

where the phase angle θ_n has been taken to be constant. Assumption of a constant θ_n does not compromise the generality of the following discussion because of that phase perturbation has the same effect on the spectra as that of frequency perturbation.

One can easily observe that the frequency spectra of the perturbed i_t are discrete line spectra, since they are products of sinusoids. Furthermore, straightforward algebra shows that the line spectra are located respectively at

$$n\omega_s \pm (\omega_{lp} \pm \hat{\omega}_s), \qquad n = 1, 2, \cdots \tag{13.11}$$

where ω_{lp} is the perturbation frequency, and $\hat{\omega}_s$ denotes the low-frequency perturbation of the switching frequency, which is constrained to be small.

The lowest frequency of the line spectrum occurs when $n = 1$, which leads to frequency components at ω_s, $\omega_s + \omega_{lp} + \hat{\omega}_s$, and $\omega_s - \omega_{lp} - \hat{\omega}_s$, respectively.

If the perturbation is introduced with a fixed switching frequency, $\hat{\omega}_s = 0$. Then, the lowest frequency component locates at

$$\omega_s - \omega_{lp}. \tag{13.12}$$

This indicates that the averaged value of current $\bar{i}_t$ will carry the same low-frequency information as the current i_t itself as long as ω_{lp} is well below half the switching frequency, i.e., $\omega_{lp} << \omega_s/2$.

Consequently, one can conclude that the equivalent duty ratio δ retains the low-frequency information, since δ is directly proportional to $\bar{i}_t$.

If the perturbation is introduced into the switching frequency, and if the frequency perturbation $\hat{\omega}_s$ is constrained to be small, the lowest frequency component of the perturbed spectrum will be at

$$\omega_S - (\omega_{lp} + \hat{\omega}_s) = \omega_s - 2\hat{\omega}_s, \tag{13.13}$$

where $\omega_{lp} = \hat{\omega}_s$ has been used, since when the switching frequency is perturbed, the possible corresponding amplitude perturbation will be at the same frequency. This expression reveals that the average value of the current $\bar{i}_t$ carries the same low-frequency information as the current i_t itself as long as the frequency of the perturbation is well below one quarter of the switching frequency, i.e., $\hat{\omega}_s << \omega_s/4$.

Therefore, one concludes that the equivalent duty ratio δ retains low-frequency information of the current i_t.

A few additional useful observations can be made from the above discussion. For converters with frequency perturbation, the requirement is more stringent than for converters with amplitude perturbation. The highest perturbation frequency for amplitude perturbation is half the switching frequency, while for frequency perturbation, it is a quarter of the switching frequency.

Note that in practice, characterizations of small-signal dynamics are often focused on low frequencies. If the perturbation frequency is constrained to be sufficiently low, the conditions for the equivalent duty ratio δ are reduced to one: the dc value is not vanishingly small.

Another important feature of averaging revealed by the discussion is that the conclusion is true regardless whether or not the quantity of interest has small or large ripple. Hence, the small-ripple constraint can be relaxed for applications of the method of averaging.

Prominent examples in this regard are converters in discontinuous conduction modes and quasi-resonant converters, both of which have large ripples.

Averaging breaks down if the quantity of interest has a vanishingly small dc value.

Prominent examples are resonant converters where the inductor current (or capacitor voltage) has zero dc value. In other words, averaging can not be applied to resonant converters not because of their large ripples, but because of the zero value of the inductor current (capacitor voltage).

13.2 The Extended Generic Model for Switches in Discontinuous Inductor Current Mode

It has been established that the equivalent duty ratio is a useful concept for modeling small-signal low-frequency dynamics. To extend the generic model to cover discontinuous conduction modes is a straightforward task now. The only thing which remains to be done is to derive an expression for transistor current i_t (or v_d) in terms of v_{off}, i_{on}, and τ_c, based on which an equivalent small-signal duty ratio control law can be derived by perturbation.

Figure 13.2 shows a typical waveform for transistor current i_t. The dc value of the current is determined by the peak value I_p and the time duration d_cT_s. From the geometry, one can find the average value as

$$\bar{i}_t = \frac{1}{2}\frac{v_{off} - \bar{v}_d}{L} \cdot d_cT_s \cdot d_cT_s \cdot \frac{1}{T_s} = d_c^2 T_s \frac{v_{off} - \bar{v}_d}{2L}. \tag{13.14}$$

Recalling the definition for the equivalent duty ratio (Eq.(13.3)), one can write

$$\delta = d_c^2 T_s \frac{v_{off}}{2Li_{on}}(1 - \delta), \tag{13.15}$$

which in turn, upon solving for δ, leads to

$$\delta = \frac{d_c^2}{d_c^2 + \dfrac{i_{on}2L}{v_{off}T_s}}, \tag{13.16}$$

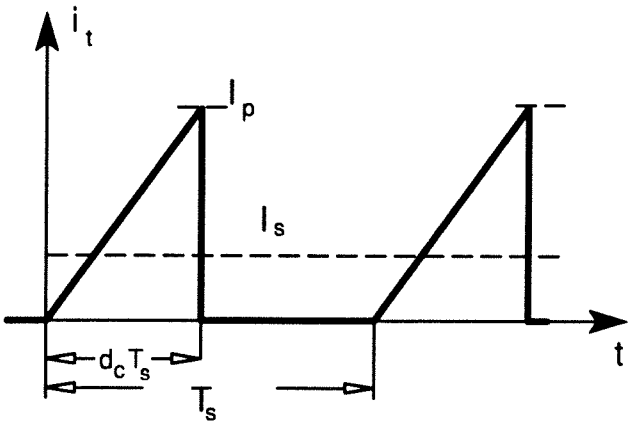

Figure 13.2: Typical waveform of transistor current i_t in discontinuous mode. Its average value is determined by the peak value I_p and the time duration d_cT_s and can be easily found from the geometry.

where d_c is the duty ratio of the transistor and is the independent control quantity.

Equation (13.16) shows that the dc value of i_t is no longer uniquely determined by duty ratio d_c. It is now a function of v_{off}, i_{on}, and d_c. Also, note that Eq. (13.16) is the same as the result presented in [14] which, however, was derived by working with current i_{on}, instead of i_t.

Replacement of d in the large-signal model in Fig. 11.2 (a) with the right-hand-side of Eq. (13.16) yields the extended generic large-signal model for converters operating in discontinuous conduction mode. Figure 13.3 (a) shows the model, which can be used to predict averaged large-signal dynamics for a converter in discontinuous inductor current mode.

The small-signal duty-ratio control law can be obtain by perturbation of Eq. (13.16). Straightforward algebra yields

$$\hat{\delta} = \frac{2\Delta(1-\Delta)}{D_c}\hat{d} - \frac{2L\Delta^2}{V_{off}T_sD_c^2}\hat{i}_{on} + \frac{2L\Delta^2 M(\Delta)}{V_{off}T_sD_c^2R}\hat{v}_{off}, \tag{13.17}$$

where $M(\Delta)$ is the equivalent voltage conversion ratio, and it has the value Δ, $\frac{1}{1-\Delta}$, and $\frac{\Delta}{1-\Delta}$ for the buck, the boost, and the buck/boost converters, respectively.

Substituting the equivalent duty ratio law into the generic model, one obtains the

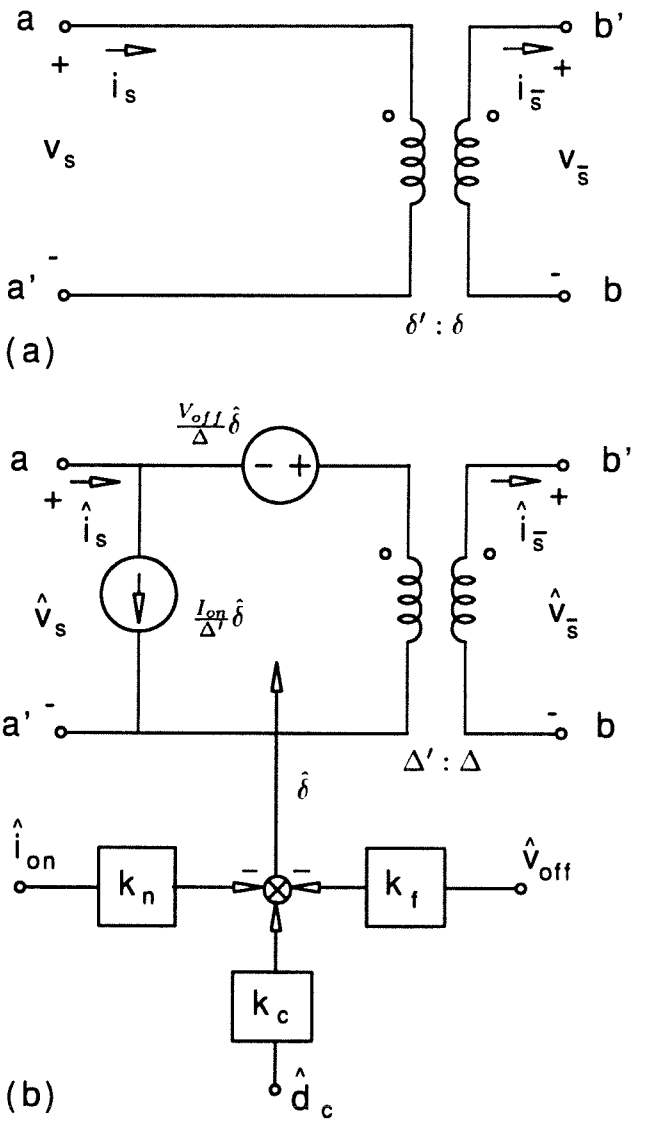

Figure 13.3: The extended generic large-signal model (a) and small-signal model (b) for converters in discontinuous inductor current mode. The effect of discontinuous inductor current is seen to be introduction of feedbacks into the model.

extended generic model for converters in discontinuous inductor current mode as shown in Fig. 13.3 (b), where the equivalent duty ratio $\hat{\delta}$ is expressed as

$$\hat{\delta} = k_c \hat{d}_c - k_n \hat{i}_{on} - k_f \hat{v}_{off}, \tag{13.18}$$

with

$$k_c = \frac{2\Delta(1-\Delta)}{D_c}, \tag{13.19}$$

$$k_n = \frac{2L\Delta^2}{V_{off} T_s D_c^2}, \tag{13.20}$$

$$k_f = \frac{2L\Delta^2 M(\Delta)}{V_{off} T_s D_c^2 R}. \tag{13.21}$$

Figure 13.3 (b) indicates discontinuous inductor current introduces feedbacks into the model, which can change the poles of the converter frequency response, but has no effect on the zeros. Note that the feedback due to $\hat{i}_{on}$ is always negative. Hence, the feedback is expected to introduce positive damping to the frequency response.

To expose the underlying damping explicitly, one can transfer the extended generic model into an equivalent y-parameter form as shown in Fig. 13.4 (a). From the form of the y-parameter model for switches, one can see that a resistance $r_{22} = 1/y_{22}$ is introduced into the model which brings damping. If r_{22} is positive, then the damping is positive. The positiveness of r_{22} indicates that the existence of feedbacks due to operation in discontinuous mode tends to split the double pole of the low-pass filter into two real poles, giving improved small-signal dynamics.

Fig. (13.4) (b) shows the equivalent circuit for the evaluation of y_{22}. Simple algebra gives

$$r_{22} = \frac{2L\Delta^2}{T_s D_c^2}, \tag{13.22}$$

which is a positive quantity since T_s, D_c, Δ, and L are all positive real numbers for any converter.

Therefore, one concludes that the feedback introduced by discontinuous inductor current brings positive damping into the model for switches, which tends to split the double pole of the equivalent low-pass filter into two real poles. That is, converters in

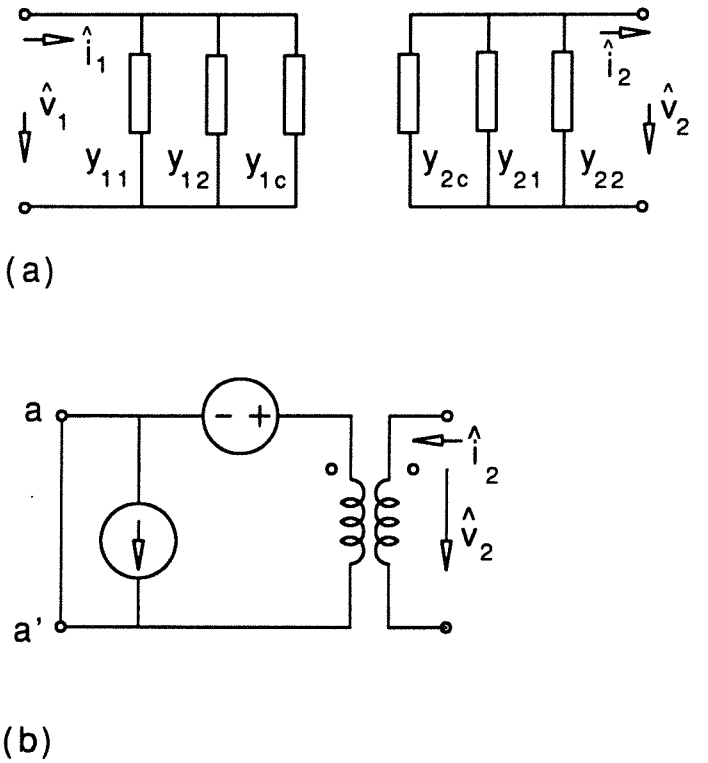

Figure 13.4: A y-parameter model can be derived from the extended model. The positiveness of y_{22} reveals that the feedback introduced by the operation of discontinuous conduction mode brings positive damping into the model, and hence tend to spilt the double pole into two real poles.

discontinuous conduction mode generally have better small-signal dynamics than converters with small ripples because of the negative feedback introduced by discontinuous inductor current.

It is important to realize that r_{22} does not consume any real power since its existence is due to the feedback introduced.

In the time domain, lossless damping describes the physical phenomenon that any perturbation of inductor current dies down to zero within one switching cycle as long as the inductor current is discontinuous.

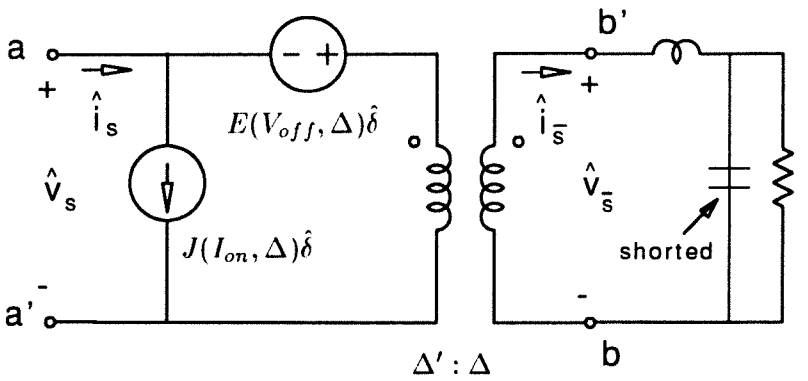

Figure 13.5: A high-frequency equivalent circuit for converters in discontinuous inductor current mode. The load resistance is shorted out of the circuit by a very low impedance presented by the capacitance which is constrained to be large for small ripple.

In other words, the boundary between continuous and discontinuous conduction modes of the inductor current represents a discontinuity of the frequency response of the converter. Across the boundary, the frequency response changes abruptly from that of a typical high-Q second-order low-pass filter to that of a typical low-Q second-order low-pass filter, or a dominate pole system with the other pole located at a much higher frequency.

The location of the high-frequency pole can be found conveniently from the generic model. Fig. 13.5 shows an equivalent circuit for a converter in discontinuous inductor current mode at high frequencies. At high frequencies, the perturbation $\hat{v}_{off}$ is virtually shorted out of the circuit by the filter capacitance.

The current-loop gain can thus be found from the equivalent circuit for high frequencies in Fig. 13.5. Straightforward algebra yields

$$T_c(s) = \frac{2L\Delta^2}{V_{off} T_s D_c^2} \frac{V_{off}}{sL} = \frac{2\Delta^2}{sD_c^2 T_s}, \tag{13.23}$$

from which the crossover frequency can be found as

$$f_c = \frac{\Delta^2}{2\pi D_c^2}\frac{2}{T_s} = \frac{\Delta^2}{D_c^2}\frac{f_s}{\pi}. \tag{13.24}$$

As established in [14], the relation $D_c < \Delta$ is true as long as the converter is in discontinuous inductor current mode. Hence, one can obtain the following lower bound for the value of f_c,

$$f_c \geq \frac{f_s}{\pi}. \tag{13.25}$$

Consider that the other closed-loop pole is primarily determined by the load resistance and the filter capacitance and is normally in the order of one tenth of the switching frequency. One can see that the two closed-loop poles are normally well separated, which is exactly the effect that operation in discontinuous conduction mode has on the small-signal dynamics.

Note that the improved dynamics for converters in discontinuous modes is well known and discussion here is meant to show the usefulness of the extended generic model for analysis as well as for simulation.

It is worth mentioning that the extended generic model is the same as the generic model in form. This is a convenient feature of the modeling approach, especially for computer simulations. In a computer simulation application of the model, all one has to do is to replace duty ratio d in the generic model by the equivalent duty ratio δ, and then make δ the function of v_{off}, i_{on}, and d_c ($\tau_c = d_c$ for this case) according to Eq. (13.16). Then, the averaged large- and small-signal behaviors of the converter can be handled in exactly the same way as for the case of converters with small ripples. In other words, for converters with large ripples, the switches can be modeled as controlled sources, which reflects the fact that with large ripples, the dc value of transistor current (or diode voltage) is a function of converter states.

It is important to point out that although it introduces feedbacks into the model, the large ripple in inductor current (capacitor voltage) does not necessarily change the small-signal dynamics qualitatively. Conclusion in this regard needs to be drawn for each particular mode of operation individually.

13.2.1 Other Extensions

The extension to converters in discontinuous capacitor voltage mode can be pursued in the same manner. It can also be obtained by invoking the principle of duality [14]. Since all steps are straightforward, details are not discussed here.

Extension can also be made easily to cover quasi-resonant converters. Results will be similar to those established in [15, 29], except that the extended generic model is for switches, instead of for converters.

It is emphasized that, in general, extensions can be made to cover any modes of operation, as long as the conditions for the equivalent duty ratio to hold is satisfied. That is, the dc value for switch voltage (or current) is not vanishingly small when the converter operates in that particular mode.

Converters which meet the condition for use of equivalent duty ratio include quasi-resonant converters, phase-shifted PWM converters, and any other soft-switching converters derived from parent PWM converters.

Also, the extended models will be the same in form as the generic model. Besides being a model for switches, this property is another major advantage over existing models for converters or for switches. The extended model is particularly convenient for applications in computer simulations, since the linear-controlled-sources feature, commonly available for circuit simulation packages, can be used with ease to build the extended generic model.

Chapter 14

Extension to Switches in Current-Programmed Converters

Current programming is intensively discussed in the first part of the thesis. The purpose of this chapter is simply to utilize those results to extend the generic model for switches to facilitate potential applications, especially for applications in computer simulation.

The extended generic model for switches in current-programmed converters is obtained by expressing duty ratio in terms of v_{off}, i_{on}, and independent control current i_c. To this end, the modulator model derived in the first part of this thesis can be directly employed.

It is shown that the extended generic model is equivalent to the model for current-controlled PWM switches proposed in [9]. The extended generic model is more convenient to use, since it is a four-terminal model for two switches.

14.1 The Extended Generic Model

Current programming is a control technique which produces, among other things, improved small-signal dynamics for switching converters. A current-programmed converter is frequently implemented with continuous conduction mode, and hence the small-ripple constraint is still met. Therefore, the equivalent duty ratio δ need not be used.

However, for a current-programmed converter, like converters in certain modes of operation where the equivalent duty ratio needs to be used, the value of duty ratio is no longer uniquely determined by independent control. Duty ratio is a function of voltage v_{off}, i_{on}, and independent control current i_c.

Extension of the generic model to switches in current-programmed converters pro-

ceeds in the same way as that to converters in discontinuous modes. A modulator model needs to be established, and then the modulator model can be substituted into the generic model to yield the extended generic model. Both the averaged large-signal model and the averaged small-signal models can be extended.

In a current-programmed converter, the duty ratio is determined by slopes of inductor current, slope of a possible compensating ramp, and the value of control current. Since the up- and down-slopes of the ramp are functions of voltage v_{off} and inductance L, the duty ratio is indirectly related to voltage v_{off}. As shown before, the average inductor current can be expressed as

$$i_l = i_c - m_c T_s d - \frac{dd'T_s}{2L} v_{off}. \tag{14.1}$$

Straightforward algebra leads to an approximate expression for d as

$$d = \frac{(i_c - i_l)}{(m_c + v_{off}/2L)T_s}. \tag{14.2}$$

If D in the generic large-signal model is replaced by the right-hand-side of Eq. (14.2), one obtains the extended large-signal model for switches in a current-programmed converter. Figure 14.1 (a) shows explicitly the extended large-signal model. This large-signal model can be used to investigate averaged large-signal dynamics. It can also be used to simulate small-signal dynamics if an analog-signal injection is performed on an appropriate place in the simulated converter.

A unified modulator model for the duty-ratio modulator in a current-programmed converter is obtained by perturbation of Eq. (14.2) and was derived previously. The end result is reprinted below,

$$\hat{d} = \frac{2L}{T_s V_{off}} \frac{1}{(D'/D'_{min} - 1)} \left[\left(\hat{i}_c - \hat{i}_l \right) - \frac{DD'T_s}{2L} \hat{v}_{off} \right]. \tag{14.3}$$

Replacement of the $\hat{d}$ in the generic model by Eq. (14.3) yields the extended generic small-signal model for switches in current-programmed converters. Figure 14.1 (b) shows the extended generic small-signal model, where

$$k_c = k_n = \frac{2L}{T_s V_{off}} \frac{1}{(D'/D'_{min} - 1)} \tag{14.4}$$

$$k_f = \frac{DD'}{V_{off}} \frac{1}{(D'/D'_{min} - 1)}. \tag{14.5}$$

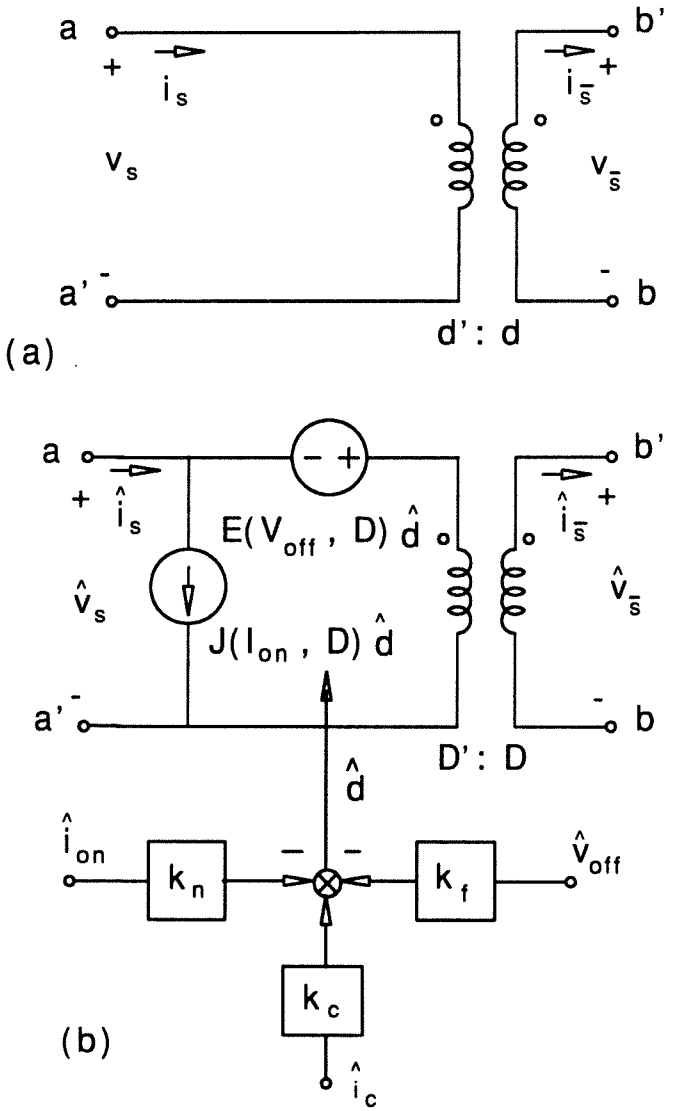

Figure 14.1: The extended generic large- and small-signal models, (a) and (b), for switches in current-programmed converters.

The effect of current programming is seen to introduce feedbacks into the model, which are expected to change poles but not zeros of the various closed-loop transfer functions of the converter.

As shown in detail in Chapter 4, when the sampling effect is considered, one additional pole needs to be added onto the current loop gain. This effect can be represented by a single-pole factor in series with the modulator gain factor F_m. Hence, the extended high-frequency generic model for switches in a current-programmed converter is given by

$$\hat{d} = \frac{2L}{T_s V_{off}} \frac{1}{(D'/D'_{min} - 1)} \frac{1}{(1 + s/\omega_p)} \left[\left(\hat{i}_c - \hat{i}_l \right) - \frac{DD'T_s}{2L} \hat{v}_{off} \right]. \tag{14.6}$$

Complications due to the presence of the additional pole ω_p are fully addressed in Chapter 4, and are therefore not repeated here.

14.2 Relationship to the Model of Current-Controlled PWM Switches

A model for switches in current-programmed converters was proposed in [9]. The model for current-controlled PWM Switches is a three-terminal model for two individual two-terminal switching devices. It is derived by utilization of the fact that the two switching devices are frequently, but not necessarily, connected together to form a three-terminal device (PWM switching structure) to realize PWM switching. Expressions for averaged terminal voltages and currents are derived in terms of v_{off}, i_{on}, and i_c, which are then perturbed to obtain corresponding small-signal expressions. The y-parameter model is then drawn according to these small-signal expressions for perturbations of averaged terminal voltages and currents.

Since both the extended generic and the model for current-controlled PWM switches are all based on the method of averaging, one may expect that they have the same performances in predicting the dynamics. Indeed, it can be shown that both models are equivalent as far as accuracy of modeling low-frequency dynamics is concerned.

To show the relationship, a y-parameter model is derived from the extended generic model. Figure 14.2 shows equivalent circuits used for evaluations of 6 y-parameters, respectively. These equivalent circuits are obtained by using the extended generic model and conditions for evaluation of the parameters. Straightforward circuit analysis leads to

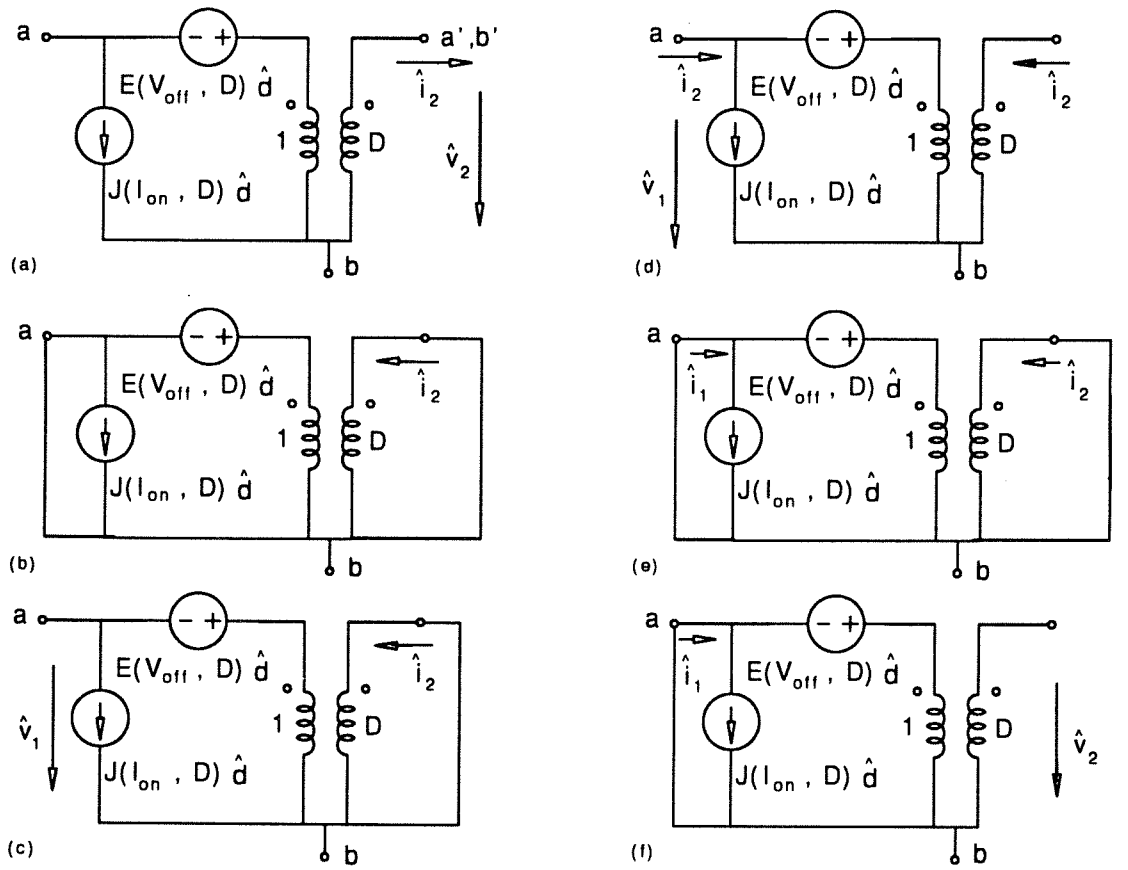

Figure 14.2: Equivalent circuits for the derivation of the y-parameter model for switches based on the extended generic model: the equivalent circuit for evaluation of y_{22} (a); the equivalent circuit for evaluation of y_{2c} (b); the equivalent circuit for evaluation of y_{21} (c); the equivalent circuit for evaluation of y_{11} (d); the equivalent circuit for evaluation of y_{1c} (e); and the equivalent circuit for evaluation of y_{12} (f).

y_{2c}	-1
y_{22}	$\frac{T_s(D'/D'_{min}-1)}{2L}$
y_{21}	$-\frac{DT_s(D'/D'_{min}-1-D')}{2L}$
y_{1c}	D
y_{11}	$D\left(y_{21}-\frac{I_{on}}{V_{off}}\right)$
y_{12}	$\frac{I_{on}}{V_{off}}-Dy_{22}$

Table 14.1: Expressions for values of y-parameters derived from the extended generic model for switches in current-programmed converters.

respective expressions for values of y-parameters, which are summarized in Table 14.1. (The notation used here for y-parameters is the same as the one used in [5]. But note that the extended model is for switches, while the model in [5] is for converters).

Useful insight can be extracted from the derived low-frequency expressions for y-parameters. Comparison of these expressions with those shown in Fig. 5 of [9] (not shown here) shows that the two sets of expressions are identical (note that notations and positive directions are different in the two models). In other words, the two models are equivalent as far as prediction for low-frequency dynamics is concerned.

The expression for y_{22} reveals that current-programming introduces a resistance $r_{22} \equiv 1/y_{22}$ into the switch model. This resistance can be rewritten as $r_{22} = \omega_c L$, where ω_c is the extrapolated crossover frequency for the current loop as discussed previously and L is the inductance. Since ω_c is a positive quantity as long as the current loop is stable, r_{22} is a positive quantity, too. The positiveness of r_{22} indicates that current-programming introduces positive damping into the switch model, tending to split the low-frequency double pole of the equivalent low-pass filter into two real poles. In other words, current programming tends to improve the frequency response of a switching converter from that of a double pole to a single pole. Identification of the positiveness of r_{22} shows explicitly

the mechanism for a current-programmed converter to improve dynamics.

One nice feature with current programming is that r_{22} does not dissipate any real power. This is true since the presence of r_{22} is due to the feedbacks introduced by current programming. This phenomenon was discussed in [5], where it was rightfully termed as "lossless damping."

A complication, not observed in [5], is that ω_c, together with ω_p, will form a closed-loop peaking if zero or a small value for the compensating ramp m_c is used. For any practical design, a certain value of m_c is always needed.

Differences do exist between the two models. The first one lies in the way that the sampling effect is handled. The model for current-controlled PWM Switches uses a capacitance to capture possible onset of subharmonic oscillation. Since this capacitance is not present physically in a current-programmed converter, insertion of the capacitance appears to be artificial.

In the extended generic model, the sampling effect is accounted for by introduction of an additional pole ω_p into the current loop. The existence of the additional pole is firmly established theoretically and experimentally in the first part of the thesis.

The second difference has to do with generality and ease of applications of the models. While it enjoys being a model for switches, the model for current-controlled PWM Switches has a fixed three-terminal structure, which is sometimes inconvenient, if not impossible, to use. Since the three-terminal PWM tree structure is only a sufficient condition to realize PWM switching, the three-terminal structure may not even exist in a valid PWM converter (see, [15, 16], for more detailed discussions). Under this circumstance, the model for current-controlled PWM Switches cannot be applied directly.

The extended generic model is a four-terminal model, and it represents each switch by its own two-terminal model. The extended generic model can be used by a simple point-to-point substitution of the model into any converter. It is applicable to converters where a three-terminal PWM switching structure is not explicitly in existence.

Therefore, one may conclude that the extended generic model is more general and more convenient to use than the model for current-controlled PWM Switches. In other words, one may say that the extended generic model for switches in current-programmed

converters extends the model for current-controlled PWM switches and covers it as a special case..

Chapter 15

Extension to Multiple Switches

Discussion has so far been limited to issues regarding modeling two switches in the environment of switching converters. This is done simply for convenience of discussion since two-switch converters are easy to understand, and are most frequently encountered in practical applications by virtue of simplicity.

In this chapter, the modeling effort is extended to multiple switches in dc-to-dc converters. For easy understanding of the theoretical aspect of the approach, and without loss of generality, key steps of the extension are illustrated through the process of modeling a novel three-switch converter. The principle of operation of the three-switch converter is described. Balance equations are then established by identifications of dc and ac equivalent circuits. Perturbation is performed to yield the generic equivalent-circuit model for three switches in their environment.

Experimental results for a prototype three-switch converter are presented to support predictions from the generic model for salient features of small-signal dynamics.

It needs to be pointed out that some of the results from analysis of as well as experimental measurement on the three-switch converter were first reported in [38, 39, 40], of which this chapter is a refined presentation with additional results.

15.1 Description of Circuit Operation of a Three-Switch Converter

Figure 15.1 (a) shows the circuit schematic for a three-switch converter disclosed in [43]. The converter is derived by a systematic approach. Its appearance is much like the Ćuk converter. The only difference is that the output inductance of the Ćuk converter is replaced by a switch (a diode). This replacement may bring large savings in terms of size and weight. The penalty for doing so is the loss of continuous output current. One ideal

application for the converter is when the output voltage is high and the output current is small, where the savings in size and weight may be substantial.

This converter has one active switch s_1, and two passive switches s_2 and $\bar{s}_3$. Switches s_1 and s_2 are turned on and off synchronously, and s_3 is switched in a fashion complementary to that of s_1 and s_2. Values for capacitances, C_1 and C_2, and inductance L are chosen to be large to maintain small ripples in their respective waveforms.

At the beginning of one switching cycle, s_1 is turned on. The converter circuit is equivalent to that of Fig. 15.1 (b). Capacitance C_1 provides energy to the parallel connection of the output capacitance C_2 and the load resistance R_L. The voltage across $\bar{s}_3$ is negative, and forces it to turn off. Since the voltage on C_1 is always larger than that of C_2, the net voltage across s_2 is always positive. Hence s_2 is turned on. This state is maintained until s_1 is turned off by the control (driving signal of the switch) at the desired value of duty ratio.

When s_1 is turned off, the circuit is equivalent to that of Fig. 15.1 (c). Input voltage forces $\bar{s}_3$ to turn off. Then, s_2 is turned off by a negative voltage presented by C_2. In the meantime, capacitance C_1 is being charged up by input voltage source V_g. Output current is maintained by energy stored in the output capacitance C_2 until the start of next cycle.

Note that the energy transfer mechanism is the same as that of the Ćuk converter, using a capacitance as the energy transfer component.

Two useful extensions of the basic topology can readily be made. An isolation transformer can be inserted into the converter by splitting capacitance C_1 into two and then introducing a transformer in between, as shown in Fig. 15.2 (a).

Another extension is to introduce additional capacitances and diodes to multiply output at the secondary, forming hence a high voltage converter as shown in Fig. 15.2 (b). For this reason, this converter is also called a three-switch high-voltage converter.

15.2 The Balance Equation and the Generic Small-Signal Model

To show clearly the key steps in derivation of a generic model for the three-switch converter, the basic version will be used as a working example in the following discussion.

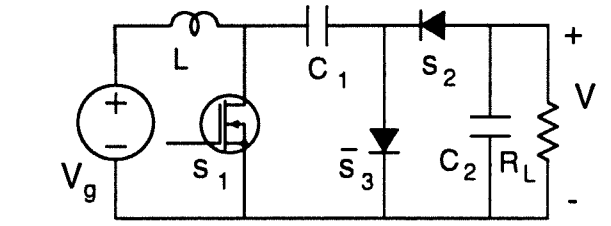

(a) Basic version

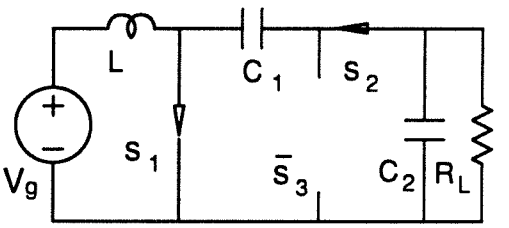

(b)

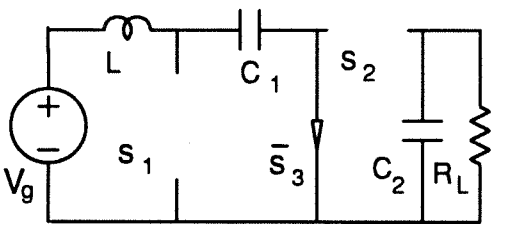

(c)

Figure 15.1: A three-switch converter: the basic version (a); the equivalent circuit when s_1 and s_2 are on and $\bar{s}_3$ is off (b); and the equivalent circuit when s_1 and s_2 are off and $\bar{s}_3$ is on (c).

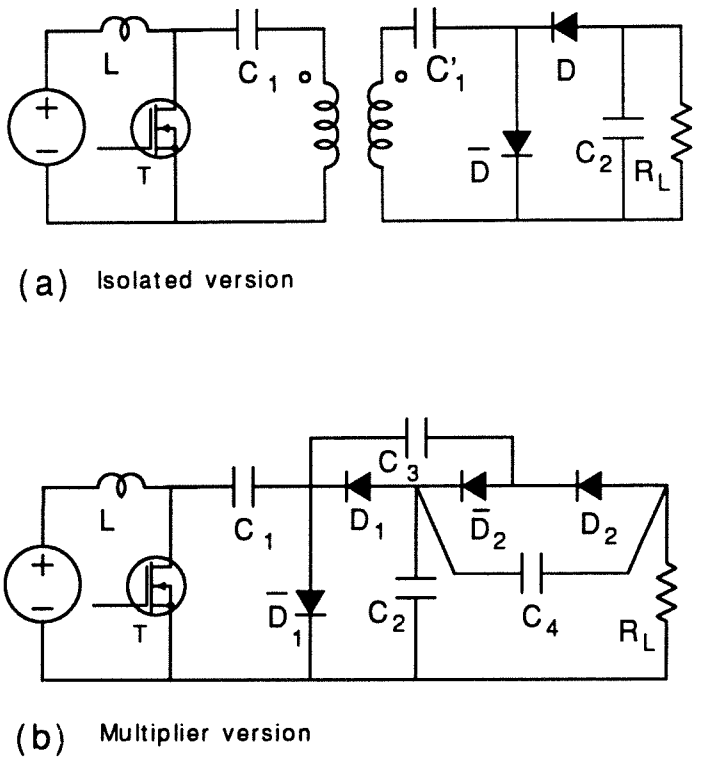

Figure 15.2: Variations of the three-switch converter: an isolated version (a); and a voltage-multiplier version (b).

Based on the circuit schematic of Fig. 15.1 (a), one can obtain its ac and dc equivalent circuits. Under the small-ripple constraint, capacitances can be opened at dc and shorted at ac (switching frequency), and inductances can be shorted at dc and opened at ac (switching frequency).

Figure 15.3 (a) shows the dc and ac equivalent circuits for the three-switch converter, obtained according to the rules of handling capacitances and inductances.

Equipped with the ac circuit, one can now proceed to derive the balance equation. Figure 15.3 (b) shows equivalent ac circuits at two different converter switching states, "on-off" and "off-on." The equivalent ac circuit for each interval is obtained by modeling a switch as a time-varying source and described by duty ratio and the dc values of switch

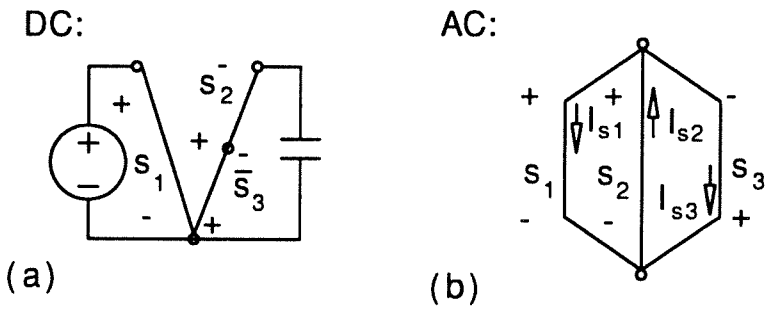

Figure 15.3: The dc and ac equivalent circuits, (a) and (b), for the three-switch converter.

voltage and current (see Chapter 10). It needs to be reiterated that time-varying models for switches in the ac circuit is totally determined if dc values of switch voltage and current are known.

From the ac circuits for two intervals and the time-varying models for switches, one can write the following balance equations by inspection,

$$\begin{cases} V_{s1}T_1 = V_{\bar{s}3}T_2 \\ V_{s2}T_1 = V_{\bar{s}3}T_2 \\ I_{\bar{s}3}T_1 = (I_{s1} - I_{s2})T_2, \end{cases}$$

which are equations governing the large-signal averaged behaviors of the converter.

Indeed, with the balance equation, the voltage conversion ratio can be easily established for the converter. The dc equivalent circuit and the balance equation show that

$$\begin{cases} V_{s1} = V_g \\ V_{s1}T_1 = V_{\bar{s}3}T_2. \end{cases} \tag{15.1}$$

In the meantime, the ac circuit shows that

$$V_{s1} = V_{s2}. \tag{15.2}$$

Equipped with these relationships, one can derive the voltage conversion ratio M as

$$M = \frac{V}{V_g} = \frac{-(V_{s2} + V_{\bar{s}3})}{V_{s1}} = -\frac{T_2 + T_1}{T_2} = -\frac{1}{D'}. \tag{15.3}$$

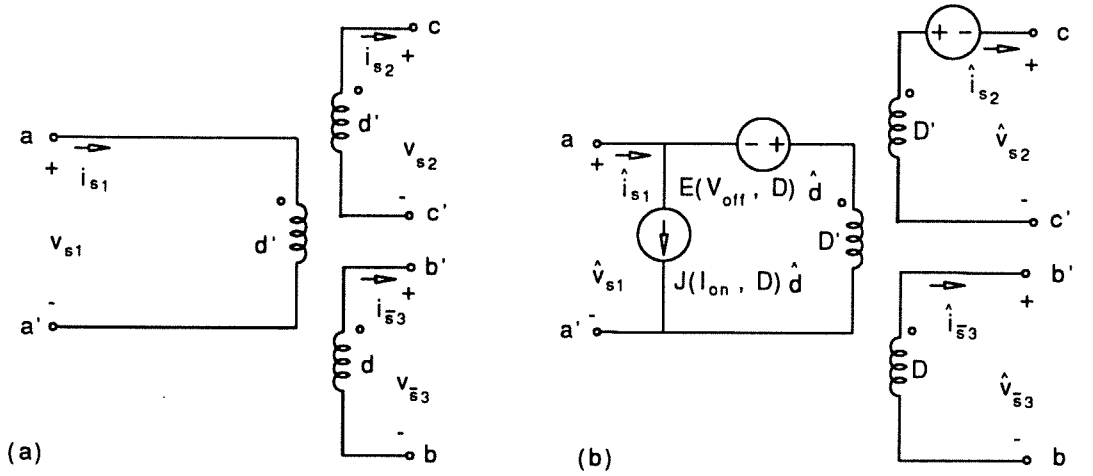

Figure 15.4: The generic small-signal model for the three switches in the three-switch converter.

It is emphasized that if the voltage conversion ratio were to be derived by conventional technique such as volt-second balance for the inductor, the derivation would have been much more involved.

Another less apparent benefit gained by use of the balance equation is that the converter which satisfies the balance equation will automatically have a steady state. In other words, the above voltage conversion ratio is physically obtainable by the steady state operation of the converter.

Having established the balance equation, one can now proceed to derive the small-signal model in a way similar to the case of two switches. Small-signal perturbation of the balance equation leads to the following set of equations governing small-signal dynamics of the three switches in the converter,

$$\begin{cases} \hat{v}_{s1}T_1 = \hat{v}_{\bar{s}3}T_2 + (V_{\bar{s}3}\hat{\tau}_2 - V_{s1}\hat{\tau}_1) \\ \hat{v}_{s2}T_1 = \hat{v}_{\bar{s}3}T_2 + (V_{\bar{s}3}\hat{\tau}_2 - V_{s2}\hat{\tau}_1) \\ \hat{i}_{\bar{s}3}T_1 = \hat{i}_{s1}T_2 - \hat{i}_{s2}T_2 - I_{\bar{s}3}\hat{\tau}_1 + (I_{s1} - I_{s2})\hat{\tau}_2. \end{cases}$$

Without loss of generality, assume the converter is controlled by pulse width modulation (PWM). Then, one additional constraint placed on small-signal dynamics is that

$$\hat{\tau}_2 = -\hat{\tau}_1 = -\hat{d}, \tag{15.4}$$

which reduces the above set of equations to

$$\begin{cases} \hat{v}_{s1}T_1 = \hat{v}_{\bar{s}3}T_2 - (V_{\bar{s}3} + V_{s1})\hat{d} \\ \hat{v}_{s2}T_1 = \hat{v}_{\bar{s}3}T_2 - (V_{\bar{s}3} + V_{s2})\hat{d} \\ \hat{i}_{\bar{s}3}T_1 = \hat{i}_{s1}T_2 - \hat{i}_{s2}T_2 - (I_{\bar{s}3} + I_{s1} - I_{s2})\hat{d}. \end{cases}$$

Based on this set of equations, one can draw an equivalent circuit model. Three independent equations determine a three-port equivalent circuit. Fig. 15.4 (a) is the averaged large-signal model for the switches, which can be used to predict averaged large-signal behaviors of switches in the three-switch converter.

Figure 15.4 (b) is the averaged small-signal model for the switches, which can be utilized to analyze averaged small-signal dynamics of switches in the three-switch converter.

Since the form of the model is invariant under different methods of control, this model is called the generic small-signal model for three switches in the three-switch converter.

Note that in the equivalent circuit, the current source representing independent control is shifted equivalently from the $\bar{s}_3$ branch to the s_1 branch to facilitate comparisons with the generic model for two switches.

The generic model for three switches indicates that the dynamic relationship between s_1 and $\bar{s}_3$ is the same as that of the generic model for two switches, which is consistent with the ac circuit for three switches. The relationship between s_1 and s_2 is different, as expected. The equivalent transformer has a unity turns ratio ($D' : D'$), and an additional voltage source exists.

Extensions of the generic small-signal model to other modes of operations such as, for example, discontinuous conduction, current programming, and soft-switching can be reached in the same manner as for the case of two switches in two-switch converters discussed previously. Hence, they are not pursued here.

15.3 Experimental Verifications

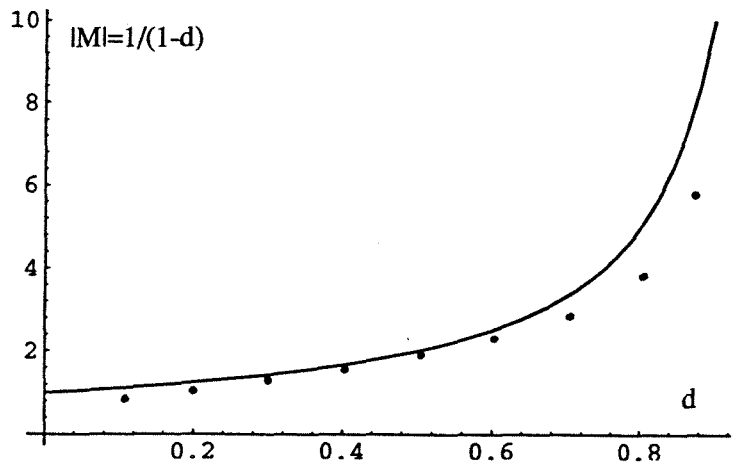

Figure 15.5: The measured and the predicted values for dc voltage conversion ratio. Good agreement between two sets of data are seen. Values of the output voltage V is normalized with respect to the input voltage V_g.

Large-signal Behavior

To verify analytical results, a prototype three-switch converter was built. The values for circuit components are: $C_1 = 5\mu F$, $C_2 = 47\mu F$, $R = 40\Omega$, $L = 480\mu H$, $D = 0.52$, $r_{c1} = 0.3\Omega$, $r_{c2} = 0.4\Omega$, and $V_g = 10V$. The switching frequency is $100kHz$.

Figure 15.5 shows the measured and the predicted dc voltage conversion ratio. Good agreement between two sets of data are seen, confirming that the derived expression for dc voltage conversion ratio $M = -1/D'$ is correct. Deviations at the low end and high end of duty-ratio values can be attributed to parasitic resistances associated with capacitors, inductors, and switching devices, which have been ignored in the expression for the voltage conversion ratio,

Table 15.1 presents measured data for the conversion ratio when one additional stage of voltage multiplier is added to the converter. A factor of two between values for V_1 and V_2 is consistently observed, validating potential applications of the three-switch converter as a high-voltage converter.

D	0.1	0.2	0.3	0.4	0.5	0.6
V_1	−7.7	−10.1	−12.1	−14.3	−17.1	−22.0
V_2	−15.9	−21.2	−24.8	−28.7	−34.1	−40.8

Table 15.1: Measured data for dc voltage conversion ratios at different values of duty ratio. The effect of a voltage doubler is clearly seen.

Small-Signal Dynamics

Figure 15.6 shows the application of the generic model to the three-switch converter, obtained by point-by-point substitution of the model into the converter. The small-signal equivalent circuit is linear and time-invariant. Any analytical method can now be used to investigate the dynamics. In particular, the design-oriented analysis can produce low-entropy expressions for various transfer functions of interests.

For example, the line transfer function is found to be

$$\frac{\hat{v}}{\hat{v}_g} = \frac{1}{D'} \frac{\left(1 + \frac{s}{\omega_{rc}}\right)}{\left(1 + \frac{s}{\omega_h}\right)\left[1 + \frac{1}{Q_o}\left(\frac{s}{\omega_o}\right) + \left(\frac{s}{\omega_o}\right)^2\right]}, \tag{15.5}$$

where

$$\omega_o = \frac{1}{\sqrt{L_e(C_1 + C_2)}}, \tag{15.6}$$

$$Q_o = \frac{R}{\sqrt{L_e/(C_1 + C_2)}} \frac{1}{\left[1 + \frac{R}{L_e/C_2}\left(r_{c2} + \frac{r_{c1}}{DD'} + \frac{r_{c1}C_1}{D'C_2}\right)\right]}, \tag{15.7}$$

$$L_e = \frac{L}{D'^2}, \tag{15.8}$$

$$\omega_{rc} = \frac{1}{r_{c2}C_2}, \tag{15.9}$$

$$\omega_h = \frac{1}{(C_1 || C_2)(r_{c1} + r_{c2})}. \tag{15.10}$$

Also, the control (duty-ratio-to-output-voltage) transfer function is given by

$$\frac{\hat{v}}{\hat{v}_g} = \frac{V}{D'} \frac{\left(1 + \frac{s}{\omega_{rc}}\right)\left[1 - \frac{1}{Q}\left(\frac{s}{\omega_{zd}}\right) + \left(\frac{s}{\omega_{zd}}\right)^2\right]}{\left(1 + \frac{s}{\omega_h}\right)\left[1 + \frac{1}{Q_o}\left(\frac{s}{\omega_o}\right) + \left(\frac{s}{\omega_o}\right)^2\right]}, \tag{15.11}$$

where additional parameters are defined as

$$\omega_{zd} = \frac{1}{\sqrt{L_e C_1}} \sqrt{\frac{D^2 R}{D'(r_{c1} + r_{c2})}}, \tag{15.12}$$

$$Q = \frac{R}{\sqrt{L_e / C_1}} \sqrt{\frac{D'(r_{c1} + r_{c2})}{D^2 R}}. \tag{15.13}$$

A double right-half-plane (RHP) zero ω_{zd} exists in the control transfer function, which needs to be controlled in order to have good phase margin.

The expression for Q reveals that the typical value of Q is not large. Furthermore, a small value for Q can be secured by selecting a small value for C_1. With $Q \ll 1$, the double zero is split into two separate real zeros given respectively by

$$\omega_1 = \frac{R}{L_e}, \tag{15.14}$$

$$\omega_2 = \frac{D^2}{D'} \frac{1}{C_1(r_{c1} + r_{c2})}. \tag{15.15}$$

Note that the value for ω_1 is exactly the same as that for a boost converter, and ω_2 is typically at much higher frequency.

Another benefit of using a small value for C_1 is that the entropy for the double pole ω_o can be lowered. Indeed, if $C_1 \ll C_2$, one has

$$\omega_o \approx \frac{1}{\sqrt{L_e C_2}}, \tag{15.16}$$

$$Q_o \approx \frac{R}{\sqrt{L_e / C_2}} \frac{1}{\left[1 + \frac{R}{L_e / C_2}(r_{c2} + \frac{r_{c1}}{DD'})\right]}, \tag{15.17}$$

which reveals that the double pole behaves in a way similar to an equivalent low-pass filter formed by L_e and C_2.

In short, low-entropy expressions reveal that the dynamics of the three-switch converter can be effectively controlled by appropriate choice of values for C_1 and C_2. The effects that C_1 and C_2 may have on the dynamics can be separated by meeting the constraint that $C_1 << C_2$. Then, the value of C_1 determines the behavior of the RHP double zero, and the value of C_2 determines the behavior for the double pole ω_o.

Figure 15.7 shows, respectively, the measured and the predicted control and the line transfer functions. Good agreements are seen between measurements and predictions. Therefore, one can conclude that the generic model is experimentally verified.

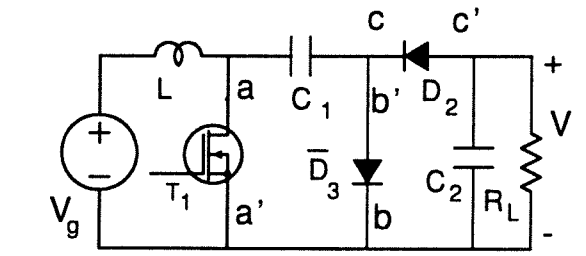

(a)

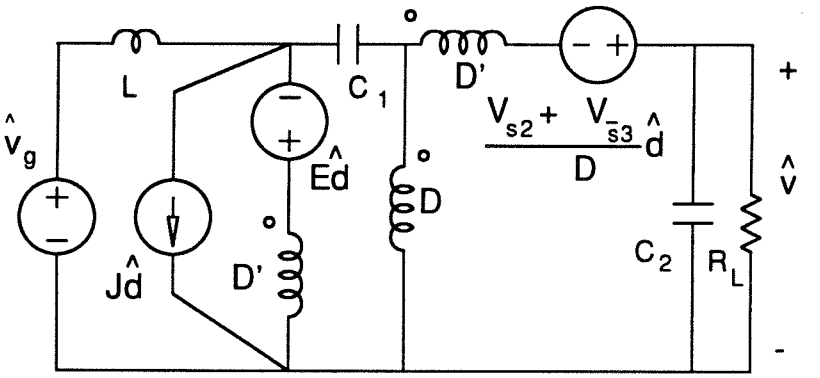

$$E = \frac{V_{s1} + V_{\bar{s}3}}{D}$$

$$J = \frac{I_{s1} + I_{\bar{s}3} - I_{s2}}{D'}$$

(b)

Figure 15.6: A small-signal linear circuit model (b) for the three-switch converter is obtained by simple point-by-point substitution of the generic model into the converter (a).

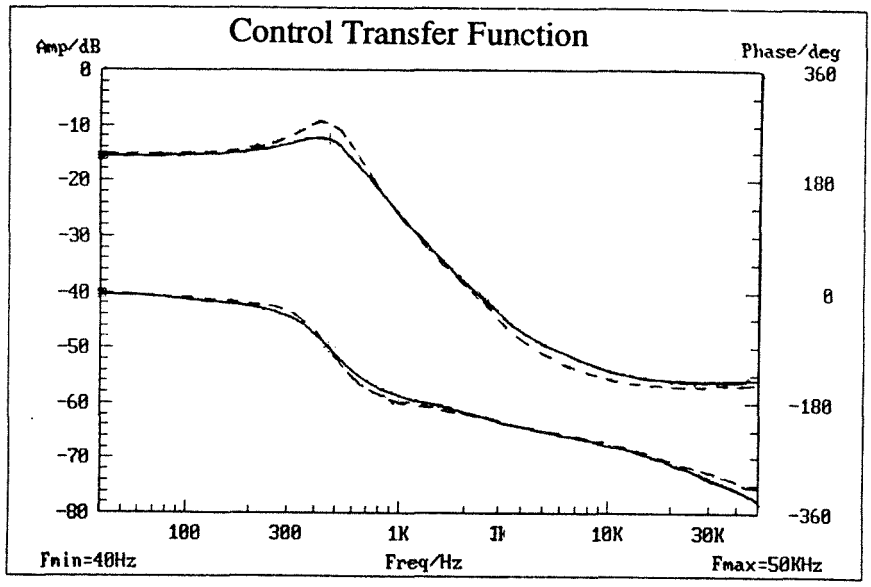

Figure 15.7: The measured and the predicted data for the control transfer function for the three-switch converter. Good agreement between two sets of data are seen.

15.3.1 Further Extensions

Further extensions of the approach to cover more than three switches can be pursued in a straightforward manner. As a matter of fact, this approach is not limited in principle by the number of switches.

The key step is to derive the balance equation for switches according to dc and ac equivalent circuits for switches in a given converter. One can follow the steps in the previous discussion, with minor modifications, to derive low-frequency large- and small-signal models for switches in a given converter with multiple switches.

Since each step was sufficiently illustrated in previous sections, details of those extensions are not presented here.

Chapter 16

Conclusions

A generic averaged model for two switches in the environment of dc-to-dc switching converters is established. It is applicable for switches in converters under constant-frequency (PWM), constant-on-time, or constant-off-time control. For constant-frequency control, it can be reduced to the PWM switch model in [34]. Also, when it is substituted into a PWM converter, it can be manipulated into a form which is identical to the canonical model [12] derived from state-space averaging.

A new powerful approach is used to derive the generic switch model. A time-varying model for switches is first introduced, which models switches as voltage or current sources in respective switching subintervals. The values of the time-varying sources are given in terms of dc values of corresponding switch voltage or current. In other words, it is an ac model in terms of dc quantities. Based on this model, dc and ac equivalent circuits for switches are derived, which in turn enables the establishment of volt-second and amp-second balance equations for the switches. Small-signal perturbation of the balance equations then leads to a set of equations governing the dynamics of the switches, from which the generic averaged model for switches is derived.

Extension of the generic model for switches to converters with isolation transformers is performed. The overall structure of the extended model is similar to its basic form, with some of the parameters of the model scaled by the transformer turns ratio n.

The generic model is also extended to switches in converters in discontinuous conduction mode. A key step in the process of extension is the introduction of the equivalent duty ratio δ, which is determined by the average value of the active switch current, or equivalently, the average value of the passive switch voltage. It is established that the averaged value of a switch voltage or current waveform can preserve the low-frequency information contained in the original waveform, as long as the original waveform has a

nonvanishing dc value. This is true regardless of the ripple contents of the waveform. Furthermore, it is observed that to preserve low-frequency information after averaging, the perturbation frequency cannot exceed half the switching frequency if the perturbation introduces amplitude perturbation only. If the perturbation introduces amplitude as well as frequency perturbations, the corresponding limit on the maximum perturbation frequency is a quarter of the switching frequency.

The extended generic model for switches in discontinuous inductor current mode predicts the same high frequency pole as that predicted in [14, 34], providing one explanation for improved small-signal dynamics. Note that the model in [14] is a model for converter. The model in the second part of [34] is a y-parameter model which is totally different from its form in constant-frequency (PWM) control. On the other hand, the extended generic switch model has the same form as its basic form, which is very useful for computer simulations.

The extended switch model for current programming also retains its form. The real difference between it and its basic form lies in that the duty ratio is no longer an independent control. It is a function of the control current i_c, voltage v_{off} and current i_{on}. A low-frequency y-parameter version of the extended generic switch model is also derived. This low-frequency version is identical to the model for current-controlled PWM switches in [9]. The value of y_{22} is seen to be positive, which in turn confirms explicitly that current programming introduces lossless damping to improve dynamics as first discussed in [5].

For easy reference, all the results can be summarized into a general form for the generic averaged model for switches, basic and extended. Figure 16.1 shows the large- and small-signal versions of the general form for the generic model. Corresponding expressions for $\delta(\cdot)$ and the feedback coefficients can be found in Table 16.1 and Table 16.2, respectively, for PWM, discontinuous conduction mode, and current programming.

It is emphasized that the table can easily be extended to cover other modes of operation such as quasi-resonant, soft-PWM switching, and any other modes of operation yet to be invented by use of the concept of equivalent duty ratio.

It is pointed out again that applications of the generic model, basic and extended,

are much more convenient than any existing models, switchwise or converterwise. It is convenient because of the facts that: 1) the generic switch model is a true switch model with two terminals for a single switch; 2) the generic averaged model for switches retains its form when extended to cover a much broader range of modes of operations where small ripples may not necessarily exist.

One important feature associated with the generic model is the unique approach used to derive large- and small-signal models. Application of the approach used in derivation of the generic switch model is not limited by the number of switches. The same principle can be applied to derive models for N switches (N denotes an positive integer) in switching converters. The key step is the establishment of the balance equation. An analysis of a novel three-switch converter is performed to demonstrate the application of the approach for multiple switches. Low-entropy expressions for the small-signal dynamics reveal design guidelines for the converter.

Finally, it is concluded that the establishment of the generic average model for switches in switching converters inherits and extends all previous modeling efforts to bring modeling of switches down to the switch level. Switches can now be handled as linear-time-invariant two-terminal circuit elements for their low-frequency characterizations.

	Constant Frequency (PWM)	Discontinuous Conduction Mode	Current Programming
$\delta(\cdot)$	d	$\dfrac{d_c^2}{d_c^2 + \dfrac{i_{on}2L}{v_{off}T_s}}$	$d(\cdot) = \dfrac{(i_c - i_l)}{(m_c + v_{off}/2L)T_s}$

Table 16.1: Expressions for $\delta(\cdot)$ in the large-signal version of the general form of the generic averaged model for switches in switching converters under PWM, discontinuous conduction mode, and current programming.

	Constant Frequency (PWM)	Discontinuous Conduction Mode	Current Programming
k_c	$\hat{\delta} = \hat{d}$, $\Delta = D$	$\dfrac{2\Delta(1-\Delta)}{D_c}$	$\dfrac{2L}{T_s V_{off}} \dfrac{1}{(D'/D'_{min} - 1)}$
k_n	0	$\dfrac{2L\Delta^2}{V_{off}T_s D_c^2}$	$\dfrac{2L}{T_s V_{off}} \dfrac{1}{(D'/D'_{min} - 1)}$
k_f	0	$-\dfrac{2L\Delta^2 M(\Delta)}{V_{off}T_s D_c^2 R}$	$\dfrac{DD'}{V_{off}} \dfrac{1}{(D'/D'_{min} - 1)}$

Table 16.2: Expressions for feedback coefficients k_c, k_n, and k_f in the small-signal version of the general form of the generic averaged model for switches in switching converters under PWM, discontinuous conduction mode, and current programming.

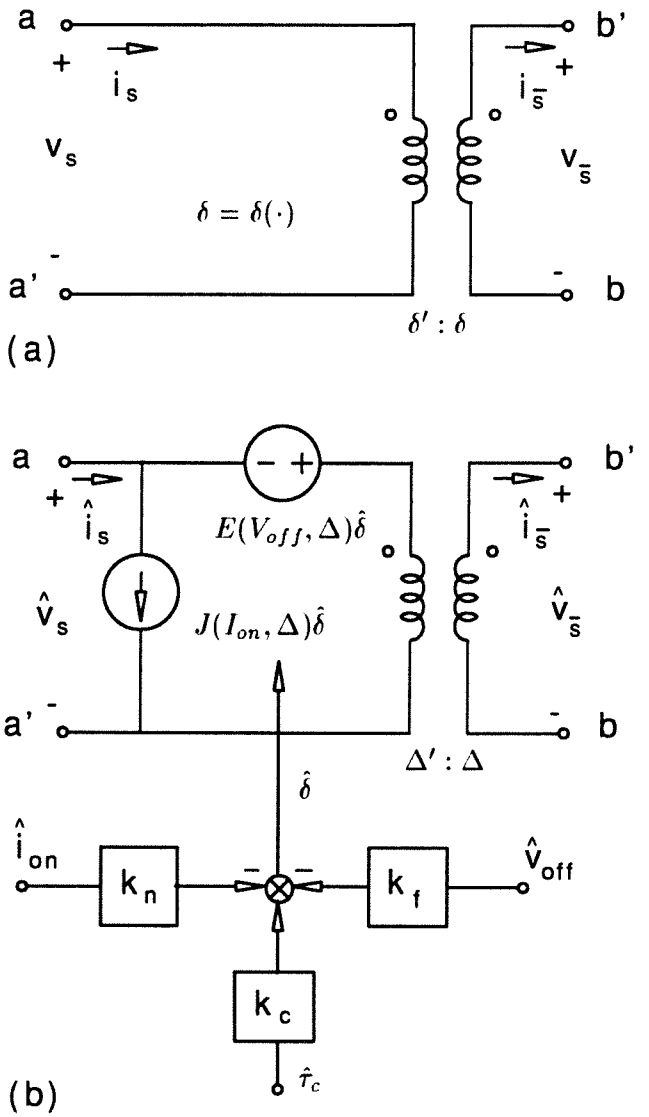

Figure 16.1: The large- and small-signal versions, (a) and (b), of the general form for the generic averaged model for switches in switching converters. The expressions for $\delta(\cdot)$ and the feedback coefficients can be found in Table 16.1 and Table 6.2, respectively, for PWM, discontinuous conduction mode, and current programming. Other modes of operations can readily be obtained by use of the equivalent duty ratio δ.

Appendix A

A Practical Sampler

In this appendix, mathematical details about a practical sampler are presented.

A mathematical model for sampling is the product of the signal to be sampled and the sampling series which is normally taken to a series of impulses.

A practical sampler performs sampling by a series of pulses instead of impulses. A small but finite pulse width introduces significant attenuation of the amplitudes for all sidebands.

Consider a series of rectangular pulses $p(t)$. Denote the small but finite pulse width by t_w. For simplicity and without loss of generality, take the magnitude of the rectangular pulses to be unity.

Then, straightforward algebra yields the Fourier expansion in the complex-variable form

$$p(t) = \sum_{-\infty}^{\infty} P_n e^{jn\omega_s t}, \tag{A.1}$$

where $\omega_s = 2\pi/T_s$ is the sampling frequency, and the Fourier coefficient P_n is given by

$$\begin{aligned} P_n &= \frac{1}{T_s}\int_{-\frac{t_w}{2}}^{\frac{t_w}{2}} 1 \cdot e^{-jn\omega_s t} dt \\ &= \frac{1}{n\pi}\sin\left(\frac{n\pi t_w}{T_s}\right). \end{aligned} \tag{A.2}$$

If a continuous-time signal $g(t)$ is sampled by the series of pulses $p(t)$, the sampled signal $g_s(t)$ can be expressed as

$$\begin{aligned} g_s(t) &= g(t)p(t) \\ &= \sum_{-\infty}^{\infty} g(t) P_n e^{jn\omega_s t}. \end{aligned} \tag{A.3}$$

According to the property of frequency shifting for the Fourier transform, one obtains the spectrum of the sampled signal as

$$G_s(\omega) = \sum_{-\infty}^{\infty} P_n G(j\omega - jn\omega_s), \tag{A.4}$$

where $G(\cdot)$ is the spectrum of $g(t)$.

Equation A.4 indicates that the spectrum of the sampled signal is replicas of $G(j\omega)$ centered at integral multiples of the sampling frequency. However, the amplitude of those replicas are scaled by the factor P_n. Since P_n is less than 1 in amplitude and decreases with n, it represents significant attenuation for sidebands.

For a better understanding, consider the baseband component of the sampled spectrum. If $t_w \ll T_s$, the baseband of the sampled spectrum, according to Eq. (A.4), is given by

$$G_s \approx \frac{1}{\pi} G(j\omega). \tag{A.5}$$

Therefore, one can see that the small but finite pulse width t_w introduces attenuation. The value is about one third, approximately $-10dB$.

In the context of measurement of loop gain, the attenuation inherently associated with the finite pulse width (practical sampling) will be observed in dc gain measurement. Equation A.4 provides an explanation for the puzzling question: Why is the dc gain measured by digital injection much lower than that measured by analog injection? The "unexpected" attenuation associated with digital injection is precisely due to the finite pulse width of the sampler, which in a switching converter is the duty ratio modulator. The sampling done by a modulator is practical since the perturbation of its output (duty ratio) is always finite, and hence the duty ratio perturbation should not be modeled as a series of impulses.

Appendix B

A Sufficient Condition

In this appendix, an attempt is made to establish a sufficient condition for the existence of a unique solution to an averaged linear time-varying system.

Two theorems are given without proofs. Mathematics-oriented people can refer to standard texts and the listed references on differential equation theory (see, for example, [44]) for a formal treatment of the topic.

Consider a time-varying system described by

$$\frac{d}{dt}x = A(t)x + B(t)u \tag{B.1}$$

where x and u are vector-valued variables, and A and B are matrices with proper dimensions. The time-varying nature of the system is indicated by the letter t in the parentheses.

The vector-valued function x is said to be a solution to Eq. (B.1) in the ordinary sense when Eq. (B.1) is satisfied for all finite $t \geq t_0$ with dx/dt being interpreted as a derivative from the right. The following theorem gives the existence of a unique solution in the ordinary sense.

Theorem B.1: *Given any $x(t_0)$, Eq. B.1 has a unique solution, in the ordinary sense, equal to $x(t_0)$ at t_0, if $A(t)$ and $B(t)$ are continuous functions of t for $t_0 \leq t \leq \infty$.*

The requirement of continuity of $A(t)$ and $B(t)$ is frequently violated in power electronics owing to inherent switching actions in switching converters. Hence, Theorem B.1 needs to be extended in order to be useful in modeling switching converters.

Before the next theorem is presented, a few terms are introduced.

Integration of both sides of Eq. (B.1) from t_0 to t yields

$$x(t) = x(t_0) + \int_{t_0}^{t} [A(\tau)x + B(\tau)u]\, d\tau. \tag{B.2}$$

A vector-valued function x is said to be locally integrable if each of its elements (1) is a continuous function except at a finite number of points on any finite interval, and (2) has a proper absolutely convergent improper Riemann integral [45] on every finite interval over the interior of which the function is continuous.

The vector-valued function x is said to be a solution to Eq. (B.1) in the extended sense, if it satisfies the integral equation (B.2) for all time $t \geq t_0$.

The following theorem gives a sufficient condition for the case where $A(t)$ and/or $B(t)$ have discontinuities.

Theorem B.2: *Given $x(t_0)$, Eq.(B.1) has a unique continuous solution, in the extended sense, equal to $x(t_0)$ at t_0, if $A(t)$ and $B(t)$ are locally integrable functions for $t \geq t_0$.*

Several comments are due here.

Note that Theorem B.2 is a sufficient condition only. A solution may well exist, even if the conditions of the theorem are not satisfied.

However, the theorem is useful because, in power electronics, $A(t)$ and $B(t)$ are frequently locally integrable, since the only discontinuities are step discontinuities associated with inherent switching actions of the converter.

More important, if more simplifying assumptions are made, Eq. (B.2) can be manipulated into averaged form.

If the operation of the integration and differentiation of x is interchangeable, which is frequently true for practical switching converters with finite turnon and turnoff times, Eq. (B.2) can be rewritten as

$$\frac{d}{dt}\int_{t_0}^{t} x\,d\tau = \int_{t_0}^{t} [A(\tau)x + B(\tau)u]\,d\tau. \tag{B.3}$$

If $A(t)$ and $B(t)$ are constrained to have small ripples, then both $A(t)$ and $B(t)$ can be approximated by their respective averaged values $\bar{A}$ and $\bar{B}$. Since they are now constant matrices, they can be moved out of the integral sign. Then, one has

$$\frac{d}{dt}\int_{t_0}^{t} x\,d\tau \;=\; \bar{A}\int_{t_0}^{t} x\,d\tau + \bar{B}\int_{t_0}^{t} u\,d\tau. \tag{B.4}$$

If the integration is performed over one switching period, one obtains that

$$\frac{d}{dt}\bar{x} = \bar{A}\bar{x} + \bar{B}\bar{u}. \tag{B.5}$$

Equation (B.5) is one form of the well-known state-space averaged description of switching converters, which says that the low-frequency small-signal dynamics of Eq (B.1) can be characterized by the characterization of its averaged system Eq. (B.5).

In short, a sufficient condition for the existence of a unique solution to a time-varying system is established. If the system matrices $A(t)$ and $B(t)$ are continuous, a unique solution exists in the ordinary sense. It the system matrices have discontinuities, a unique solution exists in the extended sense. One version of the extended solution can be manipulated into a form equivalent to the result from the well-known state-space averaging.

References

[1] C. W. Deisch, "Simple Switching Control Method Changes Power Converter into a Current Source," *IEEE PESC Record,* 1978, pp. 300-306.

[2] A. Capel, G. Ferrante, D. O'Sullivan, and A. Weinberg, "Application of the Injected Current Model for the Dynamics of Switching Regulators with the New Concept of LC3 Modulator," *IEEE PESC Record,* 1978, pp. 135-147.

[3] S.-P. Hsu, A. Brown, L. Rensink, and R. D. Middlebrook, "Modeling and Analysis of Switching DC-to-DC Converters in Constant-Frequency Current-Programmed Mode," *IEEE PESC Record,* 1979, pp. 284-301.

[4] A. B. Brown, "Topics in Modeling, Measurement, and Design of High Performance Switching Regulators," *Ph.D. Thesis,* Power Electronics Group, California Institute of Technology, 1981.

[5] R. D. Middlebrook, "Topics in Multiple-Loop Regulators and Current-Mode Programming," *IEEE PESC Record,* 1985, pp. 716-732 (also in *IEEE Trans. on Power Electronics*, Vol. 2, No. 2, 1987, pp.109-124).

[6] D. M. Mitchell, "An Analytic Investigation of Current-Injected Control for Constant-Frequency Switching Converters," *IEEE Trans. on Power Electronics,* Vol. 1, No. 3, July, 1986, pp. 167-174.

[7] G. C. Verghese, C. A. Bruzos, and K. N. Mahabir, "Averaged and Sampled-Data Models for Current Mode Control: a Reexamination," *IEEE PESC Record,* 1989, pp. 484-491.

[8] R. B. Ridley, "A New, Continuous-Time Model for Current-Mode Control," *IEEE Trans. on Power Electronics,* Vol. 6, No. 2, April, 1991, pp. 271-280.

[9] V. Vorpérian, "Analysis of Current-Mode Controlled PWM Converters Using the Model of the Current-Controlled PWM Switch," *PCIM Conference Record,* 1990.

[10] R. M. Tedder, "An Alternate Analysis of the Current-Programmed Model Leads to Simplified Input Filter Design Criteria," *IEEE APEC Record,* 1992, pp. 756-673.

[11] R. Redl, "High-Frequency Extension of the Small-Signal Model of the Constant-Frequency Current-Mode-Controlled Converters," *IEEE PESC Record,* 1991, pp. 466-472.

[12] R. D. Middlebrook and S. M. Ćuk, "A General Unified Approach to Modeling Switching Converter Power Stages," *IEEE PESC Record*, 1976, pp. 18-34.

[13] F. C. Lee, Y. Yu, and M. F. Mahmoud, "A Unified Analysis and Design Procedure for a Standardized Control Module for Dc-to-Dc Switching Regulators," *IEEE PESC Record*, 1980, pp. 284-301.

[14] D. Maksimović and S. M. Ćuk, "A Unified analysis of PWM Converters in Discontinuous Modes," *International PCIM Conference Record*, June, 1989.

[15] S. Freeland and R. D. Middlebrook, "A Unified Analysis of Converters with Resonant Switches," *IEEE PESC Record*, 1987, pp. 20-30.

[16] A. K. S. Bhat and F. D. Tan, "A Unified Approach to Characterization of PWM and Quasi-PWM Converters: Topological Constraints, Classification, and Synthesis," *IEEE PESC Record,* 1989, pp. 760-767 (also in *IEEE Trans. on Power Electronics*, Vol. 6, No. 4, 1991, pp. 719-726).

[17] R. D. Middlebrook, "Low-Entropy Expressions: the Key to Design-Oriented Analysis," *Proc. IEEE Frontiers in Education, Twenty-First Annual Conference*, Purdue University, 1991, pp. 399-403.

[18] B. Y. B. Lau and R. D. Middlebrook, "Small-Signal Frequency Response Theory for Piecewise-Constant Two-Switched-Network Dc-to-Dc Converters," *IEEE PESC Record,* 1986, pp. 186-200.

[19] B. H. Cho and F. C. Lee, "Measurement of Loop-Gain with the Digital Modulator," *IEEE PESC Record*, 1984, pp. 363-373.

[20] R. D. Middlebrook, "Predicting Modulator Phase Lag in PWM Converter Feedback Loops," *Powercon 8*, Paper H-4, 1981.

[21] C. E. Shannon, "A Mathematical Theory of Communication," *Bell System Technical Journal*, No. 3, Vol. 27, July, 1948, pp. 379-433.

[22] R. D. Middlebrook, "Measurement of Loop Gain in Feedback Systems," *Int. J. Electronics*, Vol. 38, No. 4, pp. 485-512.

[23] C.-T. Chen, *Linear System Theory and Design*, Holt, Rinehart, and Winston, New York, 1985.

[24] C. A. Desoer and E. S.Kuh, *Basic Circuit Theory*, McGraw-Hill, New York, 1969.

[25] N. Balabanian and T. A. Bickart, *Electrical Network Theory*, John Wiley, New York, 1969.

[26] H. D'Angelo, *Linear Time-Varying Systems: Analysis and Sythesis*, Allyn and Bacon, Inc., Boston, 1970.

[27] M. Vidyasagar, *Nonlinear System Analysis*, Prentice-Hall, Englewood Cliff, New Jersey, 1978.

[28] G. W. Wester and R. D. Middlebrook, "Low-Frequency Characterization of Switched Dc-Dc Converters," *IEEE Trans. on Aerospace and Electronic Systems*, Vol. AES-9, No. 3, May, 1973, pp. 376-385.

[29] V. Vorpérian, R. Tymerski, and F. C. Lee, "Equivalent Circuit Models for Resonant and PWM Switches," *IEEE Trans. on Power Electronics*, Vol. 4, No. 2, April, 1989, pp. 205-214.

[30] D. Maksimović and S. Ćuk, "A General Approach to Synthesis and Analysis of Quasi-Resonant Converters," *IEEE PESC Record*, 1989, pp. 713-727.

[31] T. Ninomiya, M. Nakahara, T. Higashi, and K. Harada,"A Unified Analysis of Resonant Converters," *IEEE Trans. on Power Electronics*, Vol. 6, No. 2, April, 1991, pp. 260-270.

[32] A. F. Witulski and R. W. Erickson, "Extension of State Space Averaging to Resonant Switches- and Beyond," *IEEE PESC Record*, 1989, pp. 476-483.

[33] V. Vlatković, Juan A. Sabaté, R. B. Ridley, F. C. Lee, and B. H. Cho, "Small-Signal Analysis of the Phase-Shift PWM Converter," *IEEE Trans. on Power Electronics*, Vol. 7, No. 1, January. 1992.

[34] V. Vorpérian, "Simplified Analysis of PWM Converters Using the Model of the PWM Switch, Part I: Continuous Conduction Mode, & Part II: Discontinuous Conduction Mode," *IEEE Trans. on Aerospace and Electronic Systems*, Vol. 26, No. 3 , May, 1990, pp. 490-505.

[35] H. A. Owen, A. Capel, and J. G. Ferrante, "Simulation and Analysis Methods for Sampled Power Electronic Systems," *IEEE PESC Record*, 1976, pp. 45-55.

[36] Harish N. Chandra and V. Joseph Thottuvellil, "Modeling and Analysis of Computer Power Systems," *IEEE PESC Record*, 1989, pp.144-151.

[37] F.-S. Tsai, "Small-Signal and Transients Analysis of a Zero-Voltage-Switched, Phase-Controlled PWM Converter Using Averaged Switch Model," *IEEE IAS Annual Meeting Record*, 1991, pp. 1010-1016.

[38] A. Pietkiewicz, "Ac Circuit Modeling Method," *Internal Presentation, Power Electronics Group*, California Institute of Technology, March, 1991.

[39] F. Dong Tan, "Experimental Verifications of New Converter Topologies," *Technical Notes, # 209*, Power Electronics Group, California Institute of Technology, April, 1991.

[40] Dongyan Zhou, "Analysis of Three-Switch High-Voltage Converter," *Technical Notes, # 225*, Power Electronics Group, California Institute of Technology, Feb., 1992.

[41] V. Joseph Thottuvellil, Fu-sheng Tsai, and D. Scott Moore, "Application of Switched-Circuit Simulators in Power Electronics Design," *IEEE APEC Proceedings,* 1993, pp. 484-490.

[42] A. Papoulis, *The Fourier Integrals and Its Application,* McGraw Hills, New York, 1962.

[43] A. Pietkiewicz and S. Ćuk, "A Three-Switch High-Voltage Converter," *U. S. Patent Application*, June, 1991.

[44] E. A. Coddington and N. Levinson, *Theory of Ordinary Differential Equations*, McGraw-Hill, New York, 1955.

[45] T. M. Apostol, *Mathematical Analysis*, second edition, Addison-Wesley, Reading, Massachusetts, 1973.